Evaluating Groundwater Inflow and Nutrient Transport to Texas Coastal Embayments

Final Report

GLO Contract No. 15-047-000-8392
August 2017

Prepared by:
Audrey Douglas, Graduate Research Assistant
Dorina Murgulet, Principal Investigator

and

Michael S. Wetz, Co-Principal Investigator
Nicholas Spalt, Research Specialist II

With assistance from:

Cody Lopez, Graduate Research Assistant
Henry Wang, Undergraduate Research Assistant

Texas A&M University-Corpus Christi
6300 Ocean Dr., Unit 5850
Corpus Christi, Texas 78412
Phone: 361-825-2309
Email: Dorina.murgulet@tamucc.edu

Submitted to:
Texas General Land Office
1700 Congress Ave.
Austin, TX 78701-1495

A report submitted to the Texas Land Commissioner pursuant to National Oceanic and Atmospheric Administration Award No. NA14NOS4190139

Contents

EXECUTIVE SUMMARY

The main purpose of this study is to advance understanding of groundwater inflows and nutrient transport to bay systems in South Texas for improved Environmental Flow recommendations and nutrient criteria by explicitly incorporating groundwater discharge into the freshwater inflow needs and nutrient budgets to the south Texas coastal embayments. A significant observation of this study, consistent across all three seasons in which sampling occurred (winter, summer, fall), is the year-round N-limitation seen in the Mission-Aransas Estuary system which aligns with previous work describing nitrogen to be the primary limiting nutrient in Texas estuaries. This is expected mainly due to the limited input of riverine inflow in South Texas. However, this study shows that the estuary is likely to be N-limited regardless of significant river discharges, those following massive precipitation and flooding events (i.e. late spring-summer 2015). Inorganic nutrient concentrations in porewater samples, particularly ammonium and orthophosphate, were often 1->100 fold higher than in water column samples, suggesting that porewater may be an intermittently important source for inorganic nutrients to the Mission-Aransas estuary. The potential importance of porewater as a source for organic nutrient inputs to the system cannot be ruled out either, although DON concentrations in porewater were highly variable in time-space.

Groundwater contribution for the Mission-Aransas Estuary estimated as part of this study is representative of excessively wet (July 2015) and moderately wet (November 2015) conditions. Groundwater discharge rates vary spatially by season; however, the average of all SGD rates exhibited very little change between July (40.4 cm/d) and November (39.1 cm/d). Furthermore, nutrient concentrations measured in the interstitial porewater also vary spatially and temporally. In the Mission-Aransas Estuary, SGD-derived nutrient fluxes for each station are

less dynamic as a function of changes in hydrologic conditions across seasons and more dependent on spatial inputs. The system-wide nutrient fluxes (i.e. season average) appear to be more dependent upon the nutrient concentrations in the interstitial fluids than on the hydrologic conditions. This study shows that SGD-derived nutrient (i.e. TDN) fluxes, from just along the mainland shoreline of the Copano Bay and Aransas Bay, are almost four orders of magnitude lower for both July (1.2×10^{-4} M N/yr) and November (1.3×10^{-4} M N/yr) than the Mission River discharge during a wet year (2.37×10^{7} M N/yr). During a dry year, assuming similar SGD rates, the shoreline SGD-derived input of TDN is only by two orders of magnitude lower for both July (1.2×10^{-2} M N/yr) and November (1.3×10^{-2} M N/yr) than the Mission River discharge during a dry year (2.29×10^{5} M N/yr). Fluxes of organic nutrients, although not compared to the river input, are much more significant than those of inorganic nutrients. A similar rate of SGD cannot be applied to the entire bay system as large heterogeneities in hydrologic conditions and porewater nutrient concentrations are likely, resulting in much larger estimates of SGD-derived nutrients. However, the nutrient input associated with sediment benthic fluxes, that could be significant in these shallow bays due to persistent winds, should not be ignored. This work is critically important for understanding nutrient dynamics in Texas estuaries and helps in setting nutrient criteria by Texas Commission on Environmental Quality (TCEQ) and the US Environmental Protection Agency (USEPA).

INTRODUCTION

Background Information

Submarine groundwater discharge (SGD) and coastal groundwater discharge (CGD) are important components of the hydrologic and biogeochemical systems that link terrestrial waters to marine environments (Burnett and Dulaiova 2003; Cardenas et al. 2010; Moore 1996). Submarine groundwater discharge enables the flow and transport of fluids and solutes from terrestrial groundwater sources into offshore coastal embayments (i.e. bays, estuaries, oceans, etc.) whereby coastal groundwater discharge occurs from offshore to inland environments (i.e. wetlands, marshes, etc.). Coastal groundwater discharge and saltwater intrusion are similar in their definition and mechanisms of fluid transport; however, CGD assumes that saline groundwater from seawater intrusion will eventually discharge into adjacent surface waters depending upon the hydrogeologic conditions. Bays and estuaries rely on a specific range of salinity and nutrient levels to maintain optimal productivity and ecosystem services (Palmer et al. 2011). Inflows from riverine and groundwater resources to estuaries are the dominant source of freshwater inflows that can affect coastal ecosystem structure indirectly by changing salinity regimes, hydrology, and transport of nutrients and contaminants. Groundwater, which can accumulate exceptionally high concentrations of nutrients and organic matter, has been shown to contribute to water quality degradation in many coastal systems worldwide (Church 1996). Organic matter-contaminated groundwater discharging to the bays may fuel bacterial respiration, leading to hypoxia formation. It has also been demonstrated that nutrient-contaminated groundwater can fuel growth of phytoplankton and algae in coastal systems. Given the arid nature of south Texas, it is conceivable that groundwater represents a significant source of freshwater, nutrients and organic matter and

plays a major role in ecosystem health. However, groundwater contribution is entirely unknown for this area as well as for most of the Texas coastal zone.

Commonly, analyses of groundwater discharge to surface water has been conducted using elemental and isotopic geochemistry (Burnett 2003; Burnett and Dulaiova 2003; Cable et al. 2004; Dimova et al. 2013; Grossman et al. 2002; Moore 1996; Su et al. 2012) as well as density-dependent flow and transport simulation codes (Guo and Langevin 2002; Murgulet and Tick 2016). Statistical methods such as analysis of variance (ANOVA), multivariate linear regression (MLR) and factor analysis on environmental data have also produced valuable models that aid in identifying variations in water quality and contamination sources in various hydrologic systems (Khan and Kumar 2012; Kim and Montagna 2012; Morehead et al. 2008; Morell et al. 1996; Palmer et al. 2011; Thareja et al. 2011; Voudouris et al. 2000). Recently, subsurface imaging techniques such as direct current electrical resistivity (ER) surveys have been increasingly used to delineate and quantify groundwater flow paths and discharge rates into surface water bodies (Dimova et al. 2012; Green et al. 2008; Greenwood et al. 2006; Nyquist et al. 2008; White 1988). Consecutive/continuous ER images acquired along the same survey lines over time periods of hours or during different environmental conditions are used to locate potential groundwater discharge seepage faces and estimate changes in discharge rates over time (Dimova et al. 2012; Johnson et al. 2012; Nyquist et al. 2008).

In south Texas, severe drought conditions caused depletion of freshwater inflows from riverine sources leading to increased salinity contents in surface waters (Schmidt and Garland 2012). Most studies in south Texas show that impaired waterways are the result of high levels of bacteria or other microbes, dissolved oxygen (DO) depletion, and increasing salinity levels (Montagna and Ritter 2006; Palmer et al. 2011). In Corpus Christi Bay, for instance, formations

of hypoxia have cyclically surfaced during the late spring through the fall months (Nelson and Montagna 2009). Various coastal systems around the world have experienced and recorded water quality degradation due to nutrient loading from groundwater that can fuel phytoplankton growth as well as bacterial respiration aiding in hypoxic episodes (Church 1996). Although monitoring efforts have been extensive, limited efforts were directed towards identifying the quality and quantity of freshwater inputs to Texas coastal embayments. Recent efforts to regulate freshwater inflows for optimal salinity ranges to promote ecosystem health of bays and estuaries along the Texas Gulf Coast do not include groundwater inputs (Alexander and Dunton 2006; Kim and Montagna 2012).

This study shows that groundwater could be a significant pathway for nutrient and other solute loading into the south Texas estuaries, particularly the secondary bays (i.e. Copano Bay), therefore requiring the incorporation of groundwater inflows for proper evaluation of freshwater and nutrient budgets. The Mission-Aransas Estuary water column and sediments have been extensively monitored and sampled but no efforts were directed in understanding groundwater contributions. The Mission-Aransas Estuary plays an important role, both environmentally and economically in south Texas, and despite the importance of groundwater discharge to the nutrient budget and overall vitality of the Mission-Aransas Estuary surrounding coastal waters, this hydrologic cycle component has been overlooked for decades.

The objectives are: 1) to map groundwater discharge and groundwater-surface water interaction zones, 2) to quantify the spatial-temporal distribution of groundwater and surface water contaminant (nutrients, organic matter) transport and discharge, 3) to evaluate nitrogen sources (i.e. anthropogenic vs. natural; agricultural vs. alternative), and 4) to evaluate the role of groundwater nutrients in system-wide nutrient budgets (i.e., inputs-outputs). To fulfill these

objectives, we quantified groundwater discharge on a seasonal basis to the Mission-Aransas Estuary and the contaminants within the groundwater that may contribute to water quality degradation. The resulting decision support products are expected to yield new information on freshwater and nutrient inflows to coastal embayments from both groundwater and surface water, characterize the interchange zone between groundwater and surface water and limitations on freshwater inflows to coastal waters, freshwater resource availability, and habitat health in representative coastal Texas embayments due to natural and anthropogenic sources. The resulting data products will be used for the development of decision support products and educational materials that will better equip resource managers and other end users to analyze, detect, and identify potential threats to freshwater resources (e.g., groundwater) and the health of environmentally sensitive ecosystems such as those of Mission-Aransas Estuary.

Study area

The Mission-Aransas Estuary is located in the coastal bend of Texas and consists of Aransas Bay, Copano Bay and several smaller bays, including Saint Charles Bay, Mission Bay, and Redfish Bay (**Figure 1**). The estuary provides essential nursery habitat for numerous commercially and recreationally important marine species. The predominantly low developed land use surrounding these bays result in more pristine conditions in the Aransas Estuary compared to the Nueces and Laguna Madre systems. However, there are emerging concerns that the ecological health of these vital habitats could be threatened by water quality degradation, specifically pertaining to harmful algae bloom (HAB) (Harred and Campbell 2014). Furthermore, agricultural and other rural practices may contribute nutrients to rivers and groundwater draining into the estuary. The estuary, formed from the drowned Mission and Aransas Rivers, has a direct connection to the Gulf of Mexico at Aransas Pass, but is largely

protected by a barrier island, San Jose Island. The estuary receives in average approximately 490,000 acre-feet of freshwater inflow from its major rivers: the Aransas and Mission Rivers, and surrounding drainage basins (TWDB 2017).

The Texas Coastal Plain has a monoclinal belt structure, gently dipping (1.8-7.5 meters (m) per km) toward the Gulf of Mexico (Baker 1979). Bed thicknesses increase down-dip, with sands accumulating approximately 215-400m in the Coastal Bend region (Ashworth and Hopkins 1995). These sediments are ambiguously grouped into the Gulf Coast Aquifer system, a major hydrostratigraphic unit composed of minor sub-units which are difficult to accurately delineate using modern methods (Mace et al. 2006). Sub-units within the system are enriched in uranium deposits, and Texas counties down the hydraulic gradient have increased mortality from malignant neoplasms of respiratory organs, which researchers attribute to increased levels of radon (Rn) and radium (Ra) (Cech et al. 1988). A sole bright side from this occurrence is that it corroborates the use of the uranium-thorium decay series as a groundwater tracer in this area.

The estuary covers 452.4 km^2, has an average depth of 2m, and seafloor composed of terrigenous and biogenic valley-fill sediments (Mooney and McClelland 2012). Spatial variability of these sediments is related to water depth, proximity to shore, and the underlying geology (Morton and McGowen 1980). Coarser grained sediments are concentrated around high-energy bay margins that erode high-standing Pleistocene sediments while deeper portions of the bay are predominantly mud.

Paleoclimate researchers denote decreasing sediment supply around 4.8 ka (kilo-annums) that likely led to the expanse of oyster reefs in Copano Bay. At approximately 2.5 ka, sediment delivery resumed as a result of increased precipitation and subsequent erosion of the Edwards Plateau (Cooke et al. 2003; Toomey III 1993; Troiani et al. 2011). Currently, the bay's

sedimentation rate is estimated to be approximately 2 millimeters per year (Troiani et al. 2011). This study area also includes the infilled Mission River Paleovalley and Copano Reef. It also considers the Mission Bay Mouth and adjacent shoreline as reference sampling sites.

The bay system is generally well mixed, in the shallow portions such as Copano Bay, due to elevated local winds, resulting in little stratification under normal conditions. Freshwater inflow to the area is sporadic, and has been connected to highly variable salinities (i.e. fresh to hypersaline) and residence times (i.e. hours for lower river reaches during storms to multiple years for the bay system) (Lebreton et al. 2016). The Mission and Aransas undammed rivers are the two main contributors of freshwater to the estuary (**Figure 1**). Furthermore, given the microtidal (small tidal range) characteristic, this bay is sensitive to meteorological forcing such as temperature, precipitation and wind. Prevailing southeastern winds from the Gulf of Mexico help regulate water temperature decreasing the occurrence of severe events (Guckian et al. 1988) and drive the shallow waters, resulting in a generally well-mixed water column (Copano Bay) during the fall and winter and a more stratified water column during the late-spring and summer, especially in the Aransas Bay.

Previous studies in the South Texas area (Breier et al. 2010; Nyquist et al. 2008; USDA 2012; Waterstone and Parsons 2003) as well as the hydraulic conditions indicate that groundwater flows toward the coast, eventually discharging into the bays and estuaries. Annual mean precipitation and evaporation rates for the Mission-Aransas Estuary are 0.35 and 0.46 km^3, respectively (Schoenbaechler et al. 2011). Tropical storms and hurricanes from the Gulf of Mexico may deliver larger quantities of rainfall during late summer and early fall on an irregular basis (Armstrong et al. 1987). The dry sub-humid climate on the shallow waters of secondary bays (i.e. Copano Bay) manifests not only through reduced freshwater inflows but also increased

salinity levels within the bay and estuary system caused by high evaporation rates and salt evapo-concentration (Bighash and Murgulet 2015).

Sediments deposited by the Mission and Aransas Rivers, the clayey Barrada and Aransas soils, are influenced by tidal effects in the bays. These sediments are gradually replaced by the Sinton and Odem soils of a loamier and sandier texture, likely a result of aeolian action (Guckian et al. 1988). The Gulf Coast Aquifer is a leaky artesian aquifer comprised of a complex of clays, silts, sands, and gravels (Ashworth and Hopkins 1995) that form the Chicot, Evangeline, and Jasper aquifers (Waterstone and Parsons 2003). The Mission-Aransas Estuary and the surrounding systems are generally in direct contact with the Chicot aquifer, which is the shallowest of the mentioned aquifers. The stratigraphic units of the Chicot aquifer consist of an overlying alluvial formation preceded by Beaumont and Lissie formations (Ashworth and Hopkins 1995), which are generally composed of clays and clayey silts with intermittent sand and gravel lenses that continue out into the Gulf of Mexico (Waterstone and Parsons 2003).

METHODS

Continuous Resistivity Profiling (CRP)

The project started with a reconnaissance survey of the study area. Land and water-based resistivity profiling were collected to locate possible groundwater upwelling zones (or SGD) in the study area. We used the Advanced Geosciences, Inc. SuperStingR8 Marine system with patented graphite electrodes and EarthImager software with induced polarization imaging system and geophysical interpretive tools to differentiate between types of lithology and water with differing resistivity/electrical conductivity to map out groundwater seepage faces and to differentiate between shallow/recirculated and deeper SGD pathways. The system is equipped with a 112 meter cable consisting of 56 graphite electrodes spaced 2 meters apart with the ability to

accurately image to a depth of approximately 20% the length of the cable. Resistivity readings of the area surveyed are collected through a dipole-dipole system that injects direct current through two current producing electrodes and measures the difference in voltage received by potential electrode pairs (AGI 2016). The SuperSting R8/IP is an 8-channel imaging system that can take up to eight readings for each current electrode allowing for a substantial decrease in survey time and increase in error correction and accuracy. This system offers the advantage of imaging both the water column (cable is deployed on the water surface) and the underlying sediments in a single run.

Continuous resistivity profiles (USGS 2013) were collected starting in Copano Bay from the Aransas River mouth and extending into Aransas Bay. These images help determine the location and possible extents of discharge zones and aid in selecting sampling and SGD monitoring sites. For these marine surveys the electrode cable is towed behind a boat along the desired transect (**Figure 2**). The beginning and end coordinates of each surveyed transect are entered into a Lowrance GPS to ensure an accurate path along the desired transect. Based on these initial assessments four locations were selected to conduct time-lapse resistivity imaging and continuous radon measurements in July and November/December, 2015 as described below.

Current is injected every 800 milli-seconds and 8 apparent resistivity values representing 8 depth levels are read for each current injection. Depth of penetration depends on length of the cable and array type (typically approximately 20% of the electrode spread length) (AGI 2016). The July and November/December time-lapse stationary resistivity images were acquired along the same survey line. Time-lapse images are conducted with the resistivity cable deployed along the bottom of the bay during which measurements are taken in sequence to fully capture the groundwater discharge during tidal cycles. Each individual ER reading was gathered into a

continuous dataset or tomograph and then inverted to earth model resistivity values using the 2D AGI EarthImager with a maximally smooth least squares algorithm (Samouelian et al. 2005). Using an initial estimate, the element resistivities are iteratively adjusted until calculated resistivities best match the measured values within a specified tolerance or until the best fit model is obtained using the root mean square error (Armstrong et al. 1987) and L-2 norm values as indicators of best fit. The prominent reason for high RMS and L-2 norm values is usually noisy raw data originating from any factors that would inhibit proper signal communication between current and potential electrodes (i.e. bent survey lines or insufficient contact with the electrodes and the medium).

Porewater conductivities were measured in the field, whenever possible, and were converted to electrical resistivity values and used to constrain the inversion results. Given the conductive nature of the imaged sediments and porewaters, and the small percent changes on subsurface sediment types (i.e. unconsolidated clays to silty-sands), any local resistivity contrasts and resulting noise levels are considered negligible, thus not affecting the resolution of the resulting ER tomography (Friedel 2003).

Water Sample Collection for Major Ions and Nutrient Analysis

Water samples from porewater and water column were collected from twenty stations in January (**Figure 3**), and eighteen in July and November (**Figure 4, Figure 5**). Samples and resistivity data were collected during three events (i.e. winter - January, summer - July and fall – November to early December) to capture groundwater discharge rates, nutrient, and biomass distribution and levels under different environmental conditions (**Figure 6, Figure 7**). Water samples were collected in compliance with standard sampling techniques (Brown et al. 1970; RCRA 2009; Wood 1976). At each location, the water depth was measured using a pre-labeled

line attached to a weight. Station depth is used to determine the necessary number of samples to be collected at each location. Samples from the water column were collected from the surface (0.2m from air-sea interface) and bottom (0.2m from sediment-water interface). Field parameters were measured before sample collection using an YSI multiparameter water quality meter. The YSI meter was placed at each sampling depth within the water column for several minutes to allow proper circulation of sample and instrument stability before parameters were recorded.

Samples from the water column were collected using a Van Dorn water sampler deployed to the desired depth and given a few minutes to allow water to circulate throughout the cartridge. Sampling bottles are rinsed three times and then overfilled, capped, and placed on ice depending on the required procedure for each analyte. A porewater sampler (AMS Retract-a-Tip) was used to collect porewater samples. The porewater sampler consists of 1 m sections of hollow steel pipe attached to a retract-a-tip point that is inserted about 0.2 to 1 m below the sediment-water interface. The depth of sample extraction is critical to sampling to prevent bottom waters from contaminating porewater samples (RCRA 2009). The sample is extracted using a peristaltic pump attached to silicone tubing which is connected to the retract-a-tip at the other end. Before sample collection the silicone tubing is purged until the sample is clear (or a minimum amount of sediment is present in the sample) and field parameters (i.e. salinity, temperature, pH) stabilize.

Major Ions and Stable Isotope Sampling

Samples for measurements of stable isotope ratios of oxygen ($\delta^{18}O$), hydrogen (δD), dissolved inorganic carbon (Dickson et al.), and carbon stable isotope ratio ($\delta^{13}C$) were also collected using the above procedure. Abundances of oxygen, hydrogen and carbon isotopes were measured (with an uncertainty of ±1per mil (‰) for δD, ± 0.1 for $\delta^{18}O$, and ± 0.2 for $\delta^{13}C$) relative

to accepted international standards, which are the Vienna Standard Mean Oceanic Water (VSMOW) (for oxygen and hydrogen) and the Vienna Pee Dee Belemnite (VPDB) (for carbon).

Major ion measurements were determined using a Dionex High Performance Ion Chromatograph (Model DX600) equipped with an autosampler, an anion-exchange column (7 mm; 4 x 250 mm; Dionex AS14A), and a conductivity detector (Dionex CD25). The detection limit of the method ranged between 0.05 and 0.1 mg/L, depending on the background signal of constituents in the samples. Iron (Fe) can also be a limiting nutrient in coastal systems and could have significant impact on GPP as it has a strong affinity for scavenging dissolved phosphate (Testa et al. 2002). Samples for these major ions as well as sodium (Na^{+}), magnesium (Mg^{2+}), total manganese (Khan and Kumar), and calcium (Ca^{2+}) were acidified to 2% ultra-high purity nitric acid (end pH <2), filtered at 0.2µm nominal pore size and analyzed using Inductively Coupled Plasma - Mass Spectrometry (ICP-MS) (Method: EPA 200.8). Detection limits vary by element and are available at http://www.chemtest.co.uk/downloads/metalsmrls-jun10.pdf.

Alkalinity and dissolved inorganic carbon (Dickson et al.) samples were collected in 250 mL borosilicate bottles with no head space and preserved using 100 microliters (µL) of saturated mercuric chloride ($HgCl_2$) (Kattner 1999). Total alkalinity was processed by Gran titration utilizing an automatic titrator with an attached temperature control water bath maintained at 22 ^{o}C and a pH electrode. Hydrochloric acid (HCl) was used as the titrant with a concentration of approximately 0.1 moles per liter (mol/L). Alkalinity samples were run multiple times to reach a precision of 0.1% (Cyronak et al. 2013).

Nutrient and Chlorophyll-α Sampling

For simplicity, we computed the average and variance for each parameter of interest for all regions as explained in the 'Spatial-temporal Distribution of Phytoplankton and Nutrients' section. Water samples were collected in acid-washed amber polycarbonate bottles using the techniques mentioned above. Bottles were stored on ice until return to a shore-based facility where processing of samples occurred and analyses were conducted for chlorophyll-α (surface water) and nutrients and organic matter (surface water and porewater).

Sample analyses – Chlorophyll-*α* was determined from samples collected on, and extracted from Whatman GF/F filters (nominal pore size 0.7 μm). Chlorophyll was extracted using 90% acetone and analyzed fluorometrically. Inorganic nutrients (nitrate + nitrite (N+N), nitrite, silicate, orthophosphate, ammonium) were determined in the filtrate of water that passed through GF/F filters using a Seal QuAAtro autoanalyzer. Dissolved organic carbon (Boyd et al.) and total dissolved nitrogen (TDN) were determined in the filtrate of water that passed through GF/F filters using a Shimadzu TOC-V analyzer with nitrogen module. Dissolved organic nitrogen (DON) was estimated as the difference between TDN and inorganic nitrogen.

Radiogenic Isotopes

Sampling and lab measurements

Samples for radium isotope measurements were collected in three-20L jugs at each of the eight June stations and ten July and November stations (Figs. 1-3). Suspended sediments that could produce additional Ra were removed in the field using a 1μm and a 0.5μm sequence of filters. Next, filtered samples were processed through ~15g fluffed manganese dioxide, MnO_2, impregnated acrylic fibers twice at a rate of <1L/min (Dimova et al. 2007; Kim et al. 2001). Following, the Mn-fibers were rinsed with Ra-free water, to eliminate any salts or particulates, and

then pressed to a water to fiber ratio of 0.3-1g (i.e., 20-30g wet weight) (Sun and Torgersen 1998). The processed fibers were placed in a gas tight cartridge and run for ^{224}Ra within 3.6 days of collection. After the ^{224}Ra measurements, fibers were flushed with nitrogen gas and sealed for >21days to reach secular equilibrium before measuring ^{226}Ra. The Ra samples were run on a RAD-7 with measurements corrected to a calibration curve determined from 5 standards. Measurements of ^{222}Rn from the 2L grab samples were conducted using a *Durridge RAD7* radon-in-air monitor and the RAD AQUA accessory. The RAD AQUA is used to bring the radon concentration in a closed air loop into equilibrium with the radon concentration in a flow-through water supply. This method was used for continuous measurements of radon in water that are used to calculate groundwater discharge rates as descried in the next section.

Submarine groundwater discharge flux calculations

Radon is much more enriched in groundwater when compared to surface waters (typically 1000-fold or greater) (Dimova et al. 2011). Because of its unreactive nature and short half-life ($T_{1/2}$ = 3.83 d) ^{222}Rn is an excellent tracer to identify areas of significant groundwater discharge (Burnett and Dulaiova 2003). Recent studies demonstrate that continuous radon measurements could provide reasonably high-resolution data to evaluate changes of radon concentration of surface water at one location over time (Burnett and Dulaiova 2003; Burnett et al. 2001). Continuous measurements of ^{222}Rn were conducted at 3 selected locations where time-lapse ER profiles were also acquired. The automated radon system (RAD 7 and the RAD AQUA accessories) was placed at the end of each resistivity transect on the deck of the research vessel. The monitoring system measures ^{222}Rn from a constant stream of water (driven by a peristaltic pump) passing through an air-water exchanger. The exchanger distributes radon from a running flow of water to a closed air loop that fees to the RAD 7 radon-in-air monitor. A detailed description of RAD 7 capabilities and

measurement principles can be found in (Burnett and Dulaiova 2003). Radon measurements were integrated over 30 minute intervals.

The main principle behind using continuous radon measurements to quantify groundwater discharge rates to surface waters is based on the inventory of ^{222}Rn over time accounting for losses/gains due to mixing with waters of different radon concentrations (i.e. low concentrations offshore waters), atmospheric evasion, and sediment inputs (**Figure 8**). Thus, changes over time, if any, can be converted to radon fluxes. Using the advective fluid radon concentrations ^{222}Rn fluxes are converted to water fluxes (Burnett and Dulaiova 2003).

Monitoring of radon extended over 4 to 8 hours depending on weather conditions (e.g., at winds of more than 12 miles per hour bay conditions become very difficult for sampling and data collection). Consequently, tidal effects could not be fully addressed using the presented methods. Nevertheless, changes in water levels of no more than 0.3 meters are recorded in this area due to tidal fluctuations (NOAA 2014). It is assumed that the lower radon fluxes observed during the monitoring time are due to mixing with offshore waters of lower concentration. The maximum absolute values of the observed negative fluxes during each time-series event at each location are used to correct radon fluxes for losses via mixing (Burnett and Dulaiova 2003; Dulaiova et al. 2006). Sediment-supported radon concentrations were measured using laboratory equilibration experiments from sediment cores collected at each time-series station following the methods outlined by Corbett et al. (1998). Sediment samples (i.e. 2cm) collected from every 10cm of the cores were placed into a 500ml Erlenmeyer flask, equilibrated with 400mL of Ra-free bay water, sealed, and after agitation on a shaker table for >21days, were analyzed for the amount of ^{222}Rn that escaped into the fluid phase. This provides the sediment equilibrated ^{222}Rn concentration (or sediment-supported 222Rn) for each SGD site. Finally, we calculate water fluxes (q, cm/d) by

dividing the total estimated ^{222}Rn fluxes (T_{total}l, Bq/m^2*s) by the concentration of ^{222}Rn (^{222}Rngw, Bq/m3) in the fluids entering the system (Burnett and Dulaiova 2003).

Relative water mass ages

The laboratory experiments conducted using sediment cores show that fluxes from bottom sediment alone are negligible for this study (see section 'Radon-derived SGD rates'). Therefore, we can assume that the major input of radium comes from groundwater rather than from sediment diffusion or resuspension. Relative radium age (Wetz et al.) of the surface water, or the relative time that has passed since the radium first entered the system in a well-mixed estuary, was calculated using the ratio of the short-lived (^{224}Ra) to the long-lived (^{226}Ra) isotopes using equation 1 from (Knee et al. 2011).

$$T_W = (AR_{GW} - AR_{Sta})/(AR_{Sta}*\lambda_{224}) \quad (1)$$

where AR_{GW} is the initial activity ratio of discharging groundwater, AR_{Sta} is the measured activity ratio at the station, and λ_{224} is the decay constant (d^{-1}) for the short-lived radium-224 isotope (Knee et al. 2011).

This equation assumes radium activities and activity radios are greatest in the Ra source (i.e. groundwater and sediment containing Ra) and also elevated in receiving nearshore water relative to waters further offshore due to SGD and desorption from sediments. Consequently, radium activities and ARs should be decreasing as the water mass is moving away from the discharge point. This could occur due to two factors: radioactive decay and mixing with more diluted offshore waters. This equation also assumes Ra additions are occurring continuously over a wide area, in this case the Mission-Aransas estuary with multiple groundwater discharge locations. The short-lived isotope is normalized to the long-lived isotope (i.e. ^{226}Ra) with activities

that are expected to only decrease due to dilution. Because the half-life of ^{226}Ra is much longer ($T_{1/2}$ = 1600 y) with respect to mixing time, its decay rate may be neglected. Using the groundwater activity ratios as the source of radium (i.e. water source), an estimate of the time since SGD occurred was provided. It should be noted that water mass ages and residence times are different ways to quantify mixing within a water body and they may not yield the same results as residence times calculate the amount of time it takes a parcel of water to leave the water body whereas water mass ages calculate the length of time since a parcel of water entered the water body.

Salinity Mass Balance and Submarine Groundwater Discharge Flux Calculations

Time-difference inversion algorithms were used to calculate the percent difference in subsurface resistivity between the consecutive ER images collected over five to nine-hour period for the July and November/December events. These differences in resistivities between time steps are used to constrain radon-derived SGD measurements and distinguish between deeper or shallow/recirculation inputs of fluids and solutes. Through this process the image collected at time=1 is used as the base image from which the image collected at time=2 is subtracted and normalized. Furthermore, the image collected at time=2 is used as the base image from which the image collected at time=3 is subtracted and normalized and so on. Changes in the subsurface bulk resistivity can be monitored between each time step. However, an overall resulting difference-image reveals changes in bulk resistivity over the entire monitoring period which is assumed to be caused by variations in pore fluid chemistry while the matrix properties remain constant (Nyquist et al. 2008). Groundwater plumes were identified and separated into zones for each time-difference inversion image using the ArcMap raster tool and the volume (V) of each zone was estimated using a 2-meter horizontal distance (Bighash and Murgulet 2015; Dimova et al. 2012). The defined zones for each difference image were superimposed onto the original ER images of their corresponding

collection time and location. Porewater salinities were corrected using the relationship between formation factor (F) and sediment porosity (ϕ) following equation 2 given by Archie's law (Archie 1942). Based on sediment core description and well logs developed in the formation extending under the Mission-Aransas Estuary, we assume a clay content of approximately 25%. Clay corrected Archie's constants have been derived using a least-squares fitting of log-porosity and log-resistivity values (Lee and Collett 2006). The clay corrected constants that assume a 25% clay content yield "*m"* and "*a*" values of 1.89 and 1.03, respectively. The porewater resistivity (Rp, Ωm) is then calculated using Archie's law for fully saturated media as expressed in equation 3. Salinity values for each superimposed zone were then estimated using equation 4 which converts the ER-derived resistivity (Rp, Ωm) to salinity (S, parts per thousand (ppt)) (Manheim et al. 2004):

$$F = a * \phi^{-m} \quad (2)$$

$$F = R_f/R_p \quad (3)$$

$$S = 7.042 \times Rp^{-1.0233} \quad (4)$$

Once the salinity for each zone was calculated, average porewater salinity was derived for the beginning (Palmer et al. 2011) and end (S2) of each time-lapse survey. With this information, the volume of groundwater discharge was calculated using a salinity mass balance approach calculated using the percent change in salinity between the initial and final time of resistivity data collection using equation 5.

$$Vgwd = Vsal[(S1-S2)/S2] \quad (5)$$

In the above mass balance approach the principle of conservation of both mass and salt is applied. Assuming a steady-state condition over a specified time, the SGD rate is calculated as the difference between the salinity inputs and outputs, not accounting for saltwater dispersion (or

diffusion) (Bighash and Murgulet 2015). Mass balances for each box are determined using the following criteria: fluxes into (out of) a box are positive (Montagna and Ritter 2006). The mass balance is based on changes in salinity concentrations over time within the surveyed area. For a detailed description of this method please refer to (Dimova et al. 2012). Equation (5) is based on the assumption that the entire volume of groundwater plumes, fresh or saline, will eventually discharge into surface waters under hydrologic conditions favoring groundwater discharge to surface water (i.e. upward hydraulic gradients).

RESULTS AND DISCUSSIONS

Selection of Groundwater End-member

The groundwater endmember used for this study was selected using methods described in more detail by Spalt (2017) as part of a Master's of Science thesis research. The selection was done by analyzing geochemical data collected from twelve wells located within the watershed. This analysis revealed trends between the average depth of the screened formation and the geochemical constituents. In general, there was a positive linear relationship between radon activity and depth ($R^2 = 0.6$), and a negative logarithmic correlation between depth and ^{224}Ra activity ($R^2 = 0.8$) as well as $^{224/226}Ra$ activity ratios ($R^2 = 0.6$). Sodium content was also significantly greater at depth ($R^2 = 0.5$). This increase in sodium content (as well as a decrease in Ca^{2+} and Mg^{2+}) suggests a change in depositional environments, thus, in the hydrogeochemical characteristics of the sampled aquifers. Piper diagram analyses were also conducted and confirm the unique characteristics. Based on these distinct geochemical relationships, only the shallowest wells (i.e. a total of four) were selected to represent the ^{222}Rn endmember (Spalt 2017).

Continuous Resistivity Profiles

Three continuous resistivity profiles (USGS 2013) were collected in December 2014 and January 2015 throughout Copano and Aransas Bays (**Figure 9)**. These CRPs were used to identify possible areas of SGD for location of monitoring stations of both water quality and stationary (i.e. resistivity) and time-series (i.e. continuous radon measurements) surveys (**Figure 10**). The following winter more CRP surveys were conducted in Copano Bay to examine the effect of geology on SGD (**Figure 9**).

Transect A-A' and B-B' show the stations selected in Copano Bay based on the resistivity data (**Figure 10**). These transects, taken along the general Aransas River paleovalley show lower resistivity values to approximately 10m depth where they sharply contrast to higher resistivity values. This is consistent with previous sub-bottom surveys conducted in the area (Troiani et al. 2011). Approaching the Copano Bay mouth the low resistivity sections are deeper but also intersect relict interfluves and anomalies that are likely associated with well/pipeline networks in that portion of the bay. Sampling locations were selected at the location of these anomalies (i.e. 4, 5, and 6), and less anomalous locations (2 and 3) (**Figure 10**).

The western transect in Aransas Bay (C-C') shows a larger degree of salinity variation in the water column that also projects into the subsurface (**Figure 10**). This portion shows more bathymetric relief (white line on the tomograph) and suggests connection to the water column from the deeper subsurface (higher resistivity sections near the sediment-water interface). For example, station 10 and 12 have the highest resistivity values of the surveys and extend to the shallow subsurface. The survey also crossed the inter-coastal waterway which has a high resistivity area beneath it.

The Northern and Eastern Aransas Bay transect (D-D') crossed the Saint Charles Bay mouth and had a higher than average subsurface resistivity (**Figure 10**). This area was selected for time-series sampling and confirmed to be sandier and therefore more resistive. Most of this transect was completed in the open bay and had a general homogenous mean resistivity to the maximum depth of the imaging. At the end of cross section and closer to shore the higher resistivity portions re-appear at approximately 10m depth. A reef was also selected for sampling (station 16) and has a higher resistivity throughout the entire vertical profile when compared to the adjacent areas.

Time-Lapse Resistivity Profiling and Resistivity-Derived SGD rates

Time-lapse resistivity images of the underlying sedimentary formations and porewaters were acquired to a depth of approximately 24 meters below the sediment-water interface. The range of apparent resistivity values was very narrow (0.17-3.6 Ωm) for all surveys indicating the highly saline nature of porewater/groundwater salinities in this area. The first time-lapse resistivity surveys were conducted in July, 2015, after a large number of precipitation events in the preceding months (**Figure 6, Figure 7**). The same survey lines were imaged in fall 2015 (end of November to beginning of December 2015), when precipitation rates and streamflow were lower than those during the summer event (**Figure 6, Figure 7**). For the time-difference resistivity tomographs, the minimum and maximum plot boundaries were set equal so that zero represented no change in resistivity and is shown as green in color.

Time-lapse ER images show potential for groundwater-surface water interaction at multiple locations within the 112-m of the survey lines for both summer and fall. Although the estimated SGD rates are very similar, the location and extent of groundwater plumes generally change from one season to another (**Figures TL 1 – TL 6; Appendix 1**). For instance, at the Saint Charles Bay Mouth (station 13) location input of fresher water is observed for the fall event

(**Figure TL 3, Figure TL 4; Appendix 1**). Furthermore, while most change in porewater chemistry in summer occurs in the top half of the imaged depth, percent resistivity/conductivity changes in fall, although smaller, were observed throughout the entire profile depth and more prominent in the deeper portion. The SGD rates derived from the salinity mass balance show more discharge during fall (105 cm/d) when compared to summer (68.7 cm/d) and follow the inverse trend of the radon-derived SGD rates (71.3 cm/d in summer and 25.8 cm/d in fall).

Time-lapse resistivity data for the Mission Bay Mouth (station 7) show less than 10% change in resistivity in both summer and fall, which is less than all time-series locations (**Figure TL 1, Figure TL 2; Appendix 1**). The change in shallow subsurface resistivity is largely related to salinity changes in the surface water. The surveys also did not differ substantially in resistivity by season. The SGD rates derived from the salinity mass balance show very low discharge in fall (2.8 cm/d) which does not correlate with the much higher radon-derived SGD rate (88 cm/d). The discrepancy between the two methods is likely due to the low variation in salinity of the interstitial fluids on which the salinity mass balance depends. Actual flow and discharge rates through the sediment may be substantially greater, but the salinity is not changing with the flow.

The Saint Charles Bay Mouth events did experience more substantial change in resistivity (**Figure TL 3, Figure TL 4; Appendix 1**). During July, there was a gradual progression of salinization in the shallow subsurface from the open bay to the bay mouth that correlated with the surface water salinization over the survey period. This change in resistivity may be attributed to the effects of density-driven flow, and may alter the location of SGD faces. Bighash and Murgulet (2015) found that the location and magnitude of groundwater discharge faces change dependent of the migration of highly saline, high density groundwater plumes.

At the Redfish Bay location (station 19), resistivity increases horizontally toward shore (right to left in figure) in the shallow subsurface (**Figure TL 5, Figure TL 6; Appendix 1**). A lower resistivity section lies beneath it and is likely saltwater-rich clay. Changes in resistivity, like the other surveys, mainly occur in the shallow subsurface across the entire 112m section. The difference of resistivity values between seasons is large at station 19. A maximum of 3.0 Ω•m in summer compared to 1.8 Ω•m in fall. Total percent changes in porewater chemistry within the underlying sedimentary formations are slightly larger in summer (15%) compared to fall (5%). Mass-balance calculations based on changes in salinity within the monitoring time period yielded SGD rates of 42.8 cm/day during the summer and 97 cm/day during the fall event which are greater than those calculated from continuous radon monitoring but follow that same increasing trend (39.9 cm/d in summer and 42.8 cm/d in fall).

Overall, time-lapse stationary ER results generally showed the exchange of porewater salinity in the shallow subsurface to be greatest, with a smaller degree and inverse change directly beneath it. This may be the result of the surveys being offshore and not being influenced by processes like tidal forcing. Rather it is likely that this discharge is related to turbulent exchange and/or density convection.

Radiogenic Isotope Concentrations

Radon-222

Radium (^{224}Ra and ^{226}Ra) and radon (^{222}Rn) isotope concentrations have fluctuated by sampling event and transect (**Table 1, Figure 11-16**). Radon concentrations were the highest in porewater with the highest concentrations in summer followed by fall while surface water concentrations are higher in fall. Porewater concentrations in general exceed concentrations supported by sediment equilibration, thus, any fluctuations in concentrations are indications of

changes in groundwater fluxes that bring in higher radon concentrations. Shallow groundwater ^{222}Rn concentrations for the shallower aquifers surrounding the Mission-Aransas Estuary system range between 5661 to 14,509 Bq/m^3. Porewater ^{222}Rn concentrations varied by location and sampling event. January and November porewater concentrations ranged from 18.9 Bq/m^3 to 994.3 Bq/m^3 (average 242.8 Bq/m^3, n=7) and 24.5 Bq/m^3 to 535.0 Bq/m^3 (average 181.92 Bq/m^3, n=7), respectively. Porewater radon concentrations in July were generally much greater, ranging from 28.1 Bq/m^3 to 2364.9 Bq/m^3 (average 922.4 Bq/m^3, n=6). This increase in porewater ^{222}Rn concentrations in July is likely due to the increased shallow groundwater flow following the heavy precipitation in April and May.

Overall the highest concentrations of ^{222}Rn in surface waters were consistently measured at Aransas River mouth (station 1), Mission Bay mouth (station 7), Aransas Bay's connection to Mesquite Bay (station 15), and the island side of lower Aransas bay (station 21) (**Figure 11**). Additionally, in November, Copano Creek mouth had a peak in concentration in the surface of the water column (354.3 Bq/m^3) more consistent with concentrations observed in porewaters than in surface waters. For Aransas River mouth, Mission Bay mouth, and Copano Creek mouth the high radon concentration could result from discharge from Aransas River, Mission River, and Copano Creek, respectively. Elevated radon concentrations were previously found to be correlated with terrestrial groundwater discharge to Oso Bay (Bighash and Murgulet 2015) and were also observed to be greater in Nueces River than in Nueces or Corpus Christi Bays (Douglas and Murgulet unpublished). On the other hand, sources of radon to sampling stations further from surface water inflows in Copano and Aransas Bays are likely the result of benthic fluxes from both groundwater discharge and bottom sediment.

Radium

Radium measurements were available for all three sampling events; however, the radium station in Aransas East (station 17) was discontinued after January and others were added for the remainder of the project (stations 8, 21, and 22 in July and station 20 in November) (**Figure 3, Figure 4, Figure 5**). For the purpose of discussion, station 21's radium data will be assigned to Aransas East as it is in relatively close proximity to station 17. The long-lived ^{226}Ra was found in highest activities during all three seasons in samples from Aransas River mouth (station 1, Copano West), during January and November in samples from Mission Bay mouth (station 7, Copano East), and during July and November in samples from St. Charles Bay mouth (station 13, Aransas North) (**Figure 12**). Aransas South was observed to have consistently low ^{226}Ra activities in all three sampling events (**Figure 12**) Given these elevated ^{226}Ra activities are located near surface water inflows and on the terrestrial side of the bays, this hints at a close terrestrial groundwater discharge source because concentrations are not altered significantly by dilution with radium depleted waters. The ^{226}Ra activities are lowest in July when salinities are lowest. On the other hand, the short-lived ^{224}Ra isotope activities in Copano Bay sampling regions experienced less variation between sampling events whereas greater seasonal heterogeneity was observed in Aransas Bay indicating more consistent benthic fluxes in Copano Bay than in Aransas Bay which appears to experience more climatic influences on groundwater discharge (**Figure 13**). Copano West had persistent high activities of short-lived ^{224}Ra indicating steady benthic fluxes which in turn facilitates the transport of dissolved chemical species between the water column and the underlying sediment.

Endmember ^{224}Ra/^{226}Ra activity ratios (Waterstone and Parsons) representing the characteristics of the groundwater radium source (i.e. shallow groundwater) were selected from

locations that were geochemically identified through grouping of regional well samples of similar geochemical characteristics collected from aquifer depths that are likely to interact with surface waters (Spalt 2017). Using these endmember ARs and the measured ARs at stations selected for radium sampling (Knee et al. 2011), water radium ages ranged from 5.9 to 18.4 days in January, from 3.4 to 13.9 days in July, and from 2.8 to 27.4 days in November (**Table 1, Figure 14-16**). A negative age may be an indication of a recent addition of radium to the system in concentrations high enough that overcome the mixing and dilution effect during transport from the initial source or that the endmember applied to the calculation is not the source of the radium for that location. We do not want to speculate on the negative age at Copano Creek Mouth during the July sampling event until the ^{226}Ra activity can be re-run and verified as very low. Average radium ages in January were the same in Copano and Aransas bays (12.3 days) and similar in November (13.1 days in Copano Bay and 12.1 days in Aransas Bay, event average 12.5 days) (**Table 1**). The youngest average radium ages were observed in July (4.4 days in Copano Bay and 10.6 days in Aransas Bay, event average 8.1 days) (**Table 1**).

Radon-derived SGD rates

Every time-lapse resistivity survey was accompanied by radon monitoring on the station. The radon monitor and field parameter YSI sonde were installed on the boat platform and deployed during the same time period. Monitoring efforts were done over a 4 to 8-hour period and for as long as the ER time-lapse data collection was conducted. It should be noted that while the radon monitoring is integrated over one square meter (m^2), the resistivity monitoring is done over a 112 m^2. Therefore, the resulting SGD rates using the ^{222}Rn fluxes do not incorporate the hydrologic and hydrogeologic "heterogeneity". Using the two techniques for calculating SGD rates it allowed us to differentiate between fresh groundwater and recirculated seawater,

delineate seepage faces as depended on sediment heterogeneity and convective flow caused by density differences.

Although short when compared to other studies in different areas outside Texas, we produced a continuous record of ^{222}Rn inventory as well as concentration over time. Excess radon in water inventories (i.e. measured ^{222}Rn in water activity minus ^{226}Ra activities, as a proxy for supported radon in the water column, multiplied by the water depth) for each time interval (15 or 30 minutes) were normalized for changes in tidal height (i.e. almost negligible in south Texas estuaries) and corrected for atmospheric loss (i.e. accounting for continuous ^{222}Rn in air measurements and wind speed), sediment supported ^{222}Rn (i.e. sediment equilibrated radon concentrations), and mixing loss (i.e. maximum negative difference between corrected inventories) in order to estimate total ^{222}Rn fluxes. These total fluxes were then divided by the average groundwater endmember ^{222}Rn activity to convert to water fluxes (i.e. SGD rates). After normalizing for tidal height (i.e. almost negligible in microtidal south Texas estuaries) and making all corrections, we estimated net ^{222}Rn fluxes ranging between -0.4×10^{-4} and 9.7×10^{-2} $Bq/m^2.s$ for July and 1.9×10^{-2} to 1.1×10^{-1} $Bq/m^{2}.s$ for November. Although no correlations are evident between these fluxes and the change in tide, these fluxes seem to fluctuate within the 4 to 8-hour period indicating the existence of other players influencing rates of groundwater discharge. For instance, Spalt (2017) found that winds might play a hydrodynamic role in the investigated system, enhancing or limiting the SGD influx.

The total estimated radon fluxes ($Bq/m^{2}.s$) were divided by the apparent ^{222}Rn activity of the advective fluids determined from geochemical analysis of multiple wells surrounding our study area (8,693 Bq/m^3) for each time interval (30 minutes in this experiment). This results in integrated average water fluxes (over the 4 to 8-hour observation period) ranging from 0.05 to

71.3 cm/day (average = 40.4 cm/d; n = 4) in July and from 25.81 to 88.02 cm/d (average = 52.2 cm/d; n = 3) for November (**Table 2**). The time series station in Aransas West (station 12) was observed to have practically zero SGD from continuous ^{222}Rn measurements after correcting for additional sources and sinks. This minimal SGD rate is supported by the resistivity imaging that indicates a continuous low permeability clay layer around this station that is impeding groundwater discharge (**Figure 10**); consequently, monitoring at this station was not continued in November.

Groundwater ^{222}Rn concentrations were found to vary significantly within the area surrounding Mission-Aransas estuarine system (5,661 to 14,509 Bq/m^3, average 8,693 Bq/m^3). Since changes in hydrologic conditions are expected and can dictate the direction of groundwater flow as well as the source of groundwater discharge, it is likely that the geochemical signature of groundwater discharging at any location within the bay will vary spatially and temporally. Groundwater fluxes determined using radon concentrations are extremely sensitive to the concentration of radon in the upwelling fluid (i.e. radon fluxes are divided by the advective pore fluid ^{222}Rn concentration. A change of one order of magnitude in radon concentration will result in an increase or decrease of the groundwater flux by one order of magnitude as well. Thus groundwater fluxes calculated using our lowest ^{222}Rn endmember concentration are higher by an order of magnitude than those estimated using our highest ^{222}Rn endmember concentration. For example, dividing the radon flux values at Mission Bay mouth (station 7) by the lowest ^{222}Rn activity of the advective fluids increases the SGD rates by over twice the rates derived by dividing by the highest ^{222}Rn activity and almost doubles the rates derived from the average (i.e. July SGD increases from 52.7 cm/d (highest ^{222}Rn activity) to 88.0 cm/d (average activity) to 135.1 cm/d (lowest activity)). Additionally, surficial recirculation of water could increase the

radon flux that is not related to lateral groundwater discharge. To limit the uncertainty associated with these calculations for nutrient flux estimates we use an average groundwater discharge rate.

Major Ion and Stable Isotopes

Major Ions

In an effort to further constrain the groundwater flux estimations, porewater and surface water samples were analyzed for major ions such as sulfate (SO_4^{2-}), chloride (Cl^-), sodium (Na^+), potassium (K^+), total manganese (Khan and Kumar), magnesium (Mg^{2+}), calcium (Ca^{2+}), and total iron (Fe). Most of these major ions are conservative elements. The solubility of the minerals that supply these elements is high in seawater (i.e. NaCl, KCl, $MgSO_4$, and $CaSO_4$). Thus, the concentration of these elements normalized to salinity or Cl^- is generally constant and the ratio of one conservative element to another should be constant also. Until recently, Mg^{2+} was assumed to be conservative but studies show local anomalies of Mg^{2+} in deep waters and it can be completely removed in high temperature hydrothermal vent solutions. Furthermore, SO_4^{2-} is conservative in oxic waters but not in anoxic sediments and waters. Sulfate reducing bacteria use SO_4^{2-} and forms HS^- or H_2S. The concept of residence time is informative in several ways (Murray 2004). Residence time of these elements offers insight related to their fate in seawater. For instance, elements such as Na^+ and Cl^- have long residence times in the ocean and tend to be very soluble in sea water as well as evenly mixed throughout the ocean. Therefore, they occur in the same ratio to one another throughout the ocean regardless of the total salinity. Elements with short residence times such as Fe are relatively reactive or insoluble in sea water (i.e. pH dependent) and therefore, they are easily removed and are unevenly distributed throughout the ocean.

Ratios of the major elements to chlorinity have been used in this study to analyze sources of water to the investigated embayments. Ratios of SO_4^{2-}/Cl^- varied by season with the largest

ratios measured during the summer (July) event followed by winter (January) (**Figure 17, Figure 18, Figure 19**). However, the relationship with chloride, an indicator of salinity, varies by season. The highest ratios are associated with lower Cl concentrations in January, a sampling event following a long period of drought, as displayed in the SO_4^{2-}/Cl^- versus Cl graph (**Figure 18**). This trend has also been observed in Corpus Christi Bay during all three sampling events, all during the drought extending into 2014 but SO_4^{2-} was in excess when compared to seawater (Murgulet et al. 2015). In the Mission-Aransas Estuary however, although an inverse relationship is also observed in January, SO_4^{2-} concentrations are not in excess to seawater. Reduction of SO_4^{2-} seems to occur along a salinity gradient going from Redfish Bay (lower salinity/chloride and highest SO_4^{2-}/Cl^-) to Copano Bay (highest salinity/chloride and lowest SO_4^{2-}/Cl^-) indicative of reverse estuary conditions (Error! Reference source not found.**Figure 18, Figure 20**). The gradient is completely reversed in July, following significant rain and flooding events in South Texas (**Figure 6, Figure 7**), but no linear relationship exists between the ratio and chloride. Although sulfate production is noted across Copano Bay all ratios are lower when compared to seawater especially at stations closer to Aransas River. Sulfate production above seawater levels occurs at most stations (**Figure 17, Figure 20**) Although studies show that riverine inflows to estuaries are likely to increase the SO_4^{2-}/Cl^- ratio (Matson and Brinson 1985), in this study SO_4^{2-} is measured in lower amounts in close proximity to the main riverine inflow to the estuary (i.e. Aransas River). In November, SO_4^{2-}/Cl^- ratios show no trend with salinity/Cl^- (a salinity gradient is measured from Aransas River to Redfish Bay) and are similar across the bays with only slight enrichment in bottom waters in close proximity to Aransas River and in the Aransas Bay (**Figure 18**).

Mass ratios of Mg^{2+}/Cl^-, Ca^{2+}/Cl^-, and K^+/Cl^- show some enrichment of the three elements across seasons with the largest enrichments over chlorinity in January, in Aransas Bay, and July,

in Copano Bay and across the estuary in November (**Figure 21, Figure 22**). The highest enrichment, when compared to seawater, is measured in July and is correlated with the lowest chloride levels, following the spring flooding event (**Figure 23, Figure 24**). An inverse relationship between the ratios of Ca^{2+}/Cl^- and K^+/Cl^- with Cl^- is only observed in July across the estuary, but the change across Copano Bay is much more abrupt and much less dependent on salinity (**Figure 20**) with greatest input/enrichment over chlorinity mid-bay rather than at the river mouth. Concentrations of Mg^{2+} are more depleted in July in Aransas Bay going into Redfish Bay when compared to January and November (**Figure 21, Figure 23**). This could be the result of mineral precipitation enhanced by changes (increase) in pH (**Figure 25**) associated with freshwater inputs. For K^+ and Ca^{2+}, sediment fluxes are likely to enhance their transport to surface waters. Mass ratios of Na^+/Cl^- show similar trends to all the above elements but Na is much more enriched when compared to the seawater Na^+/Cl^- ratio (**Figure 26, Figure 27**). Although lower Na^+/Cl^- ratios are characteristic for the January event, an enrichment of Na^+ over Cl^- in relation to seawater is consistently observed (**Figure 27**). These ratios show that chemical characteristics of water are significantly different from season to season given that significant amounts of runoff of river discharge contribute to estuary.

In most cases the sample ratios exceed the typical seawater ratio (at 18,980 mg/L Cl^-) extending towards higher ratios especially in July, in the Copano Bay. This is clearly the influence of freshwater inflow from riverine inputs and possibly groundwater discharge as a result of increased water table levels (i.e. following rain events starting in March-April (**Figure 6, Figure 7**). Although no significant salinity differences were measured during the post-flooding event in July, larger ratios of most elements are measured at the Mission Bay and Copano Creek River mouth and station closest to the Aransas Bay mouth. Furthermore, at the Aransas River mouth

mass ratios are lower than the stations mentioned above but are larger than the rest of the estuary. Studies show that dilution of interstitial water in the sediments could enhance dissolution of some elements from the sediment and increase the total abundance in elements (Murthy, 1973 #135). Mass ratios are in general more elevated in the Aransas Bay and Redfish Bay in January when very insignificant riverine inflows were measured. November shows a significant decrease of molar ratios in Copano Bay and slight increase in Aransas Bay when compared to July.

Sulfate concentrations show a clear positive relationship with Cl^- for all seasons with slightly more variability for the January event, including difference between bottom and surface water, when the highest concentrations are measured (**Figure 17, Figure 18**). SO_4^{2-}/Cl^- ratios show a positive relationship with Cl^- during January and even more significant during July (**Figure 18**). Although higher concentrations of SO_4^{2-} were measured in January, SO_4^{2-}/Cl^- ratios are lower relative to the conservative seawater one (0.14 mass ratio) (**Figure 17**). Slight enrichment of sulfate over the seawater is only exhibited in some of the surface and bottom water samples in Aransas Bay. The significant SO_4^{2-} reduction in Copano Bay occurs during a season following a long drought record and salinities which could be indicative of anoxic conditions when sulfate reducing bacteria are more prevalent (Minz et al. 1999).

July follows the same pattern as January except concentrations are more homogeneous in both surface and bottom waters (**Figure 17**). Concentrations of sulfate are the lowest in Copano Bay but remain still elevated in the Aransas Bay, following a salinity gradient (higher sulfate associated with higher Cl^-/salinities (**Figure 19, Figure 20**)). This trend is associated with limited riverine inflows but elevated DO concentrations (**Figure 25**). The lower concentrations of SO_4^{2-} in the Copano West (CW) following significant rain and increased freshwater inflows, indicate

that Aransas River is not a contributor of SO_4^{2-} to the estuary. Similar characteristics were evident also with other major dissolve ions as mentioned above (i.e. Na^+, Ca^{2+}, K^+, Mg^{2+}).

By fall most excess SO_4^{2-} has been removed from the water column (**Figure 17**) presumably due to dilution with runoff or river water that is more depleted in SO_4^{2-} along the Copano-Aransas-Redfish Bays gradient or due to SO_4^{2-} reduction as salinity starts to increase again. Some enrichment of SO_4^{2-} over Cl^- is observed in bottom waters in close proximity to the Aransas River mouth. Different chemical processes and sources influence the estuary especially during dry and wet conditions). Although the Mission-Aransas estuary experienced a significant influx of freshwater prior to July, levels of DO are lower than in January (**Figure 25**). In general during summer, more anoxic conditions are prevalent in estuaries. It appears that in the investigated estuary the input of oxygen from river inflow is exceeded by the large primary productivity as a result of large nutrient inputs following the rain events in late spring, especially in Copano Bay and Aransas Bay East and North as indicated by large chlorophyll-a levels (**Figure 33**) (Zhang et al. 2011). Higher oxygen consumption than production during the hot summer months is also possible following a period of continuous production. The higher DO concentrations in January could be caused by continuous mixing of bay waters due to winds with larger effects on shallow water (as expected after a prolonged period of drought).

Iron is an important metal for living organisms. Like other nutrients, iron availability can limit primary production and therefore, the food availability for heterotrophic organisms. Iron limitation of phytoplankton has received attention especially in oceanic regions with low biomass, despite high nutrient levels (de Baar et al. 1999; Gran 1931; Martin et al. 1994). Studies show that although phytoplankton is not iron-starved per se, the low ambient iron concentrations may inhibit biomass accumulation (Boyd et al. 2000; Coale et al. 1996; Martin et al. 1994). The sources of

iron for the pelagic community are several: aeolian input with terrigenous matter; riverine input especially in coastal areas; re-mineralization of organic matter can release iron in deeper waters and after upwelling this can be a source of iron (Bowie et al. 2002). Finally, sediments can be a source of iron if sedimentary iron oxides are reduced (directly or indirectly) during anaerobic mineralization processes and then escape to the overlying water. This last process couples the iron cycle to the carbon cycle.

Iron concentrations are the highest in summer (July) especially in Copano Bay and they decreased along the increasing salinity gradient going towards Aransas Bay South (**Figure 21**). Although the other two seasons show a lower enrichment of Fe over Cl^-, when compared to the seawater, Fe concentrations are in excess across the entire investigation period. Overall the mass ratio of Fe to Cl^- (Fe/Cl^-) show an inverse relationship with Cl^- (salinity), but seasonally, the highest correlation is exhibited in January (**Figure 21**). This is similar to the Mg^{2+} relationship to Cl^-. Also, similar to most other major ions ratios, in November the excess Fe in relation to Cl^- becomes homogeneous across the estuary. The decreasing excess of Fe along with the increasing salinity gradient in July could suggest the possibility that iron is being consumed for primary production of phytoplankton. The lower concentrations starting with Aransas Bay North and East is likely the result of lower degrees of mixing with river waters further away from the inflows. Since the lowest production is expected during winter, iron concentrations are anticipated to be the highest. Regardless if Fe is being used, its concentrations always exceeding the seawater ratio indicate that even in the absence of riverine inflow Fe is being supplied by other sources in this estuary. Remineralization of organic matter and sediment fluxes as well as terrigenous aeolian inputs could lead to these enrichment in Fe.

Because the reduced form of manganese is more mobile, it occurs as solute mostly in porewater. Porewater samples are by one to two orders of magnitude more enriched in manganese compared to surface water with most enriched measurement in January (average: 0.5 mg/L) and similar concentrations for July (average: 0.3 mg/L) and November (average: 0.2 mg/L) (**Figure 28**). Unlike Corpus Christy Bay (Murgulet et al. 2015), with most depleted levels of manganese exhibited in January, in the Mission-Aransas Estuary the lowest concentrations of manganese are measured in November (average: 0.01 mg/L) followed by the January season (average: 0.02 mg/L). The highest concentrations are measured following the persistent rain events in late spring (average: 0.03 mg/L). There are many (bio) geochemical processes that can affect the mobility of manganese are diverse (Slomp et al. 1997) such as oxidation of organic carbon, microbial reduction (Burdige et al. 1992), re-oxidation of Fe (Toomey III), or pyrite and iron sulphide oxidation (Schippers and Jorgensen 2001). A speciation analysis of different cations is necessary to understand processes driving variation in manganese concentrations in this estuary.

Total alkalinity concentrations vary both temporally and spatially (**Figure 29**). The lowest TA concentrations were measured in Copano Bay during the driest monitored season in January accompanied by the highest Cl/salinity levels (**Figure 18, Figure 20**). No correlation between salinity and TA exists for the July and November events and a relatively weak inverse correlation exists for the dry event (January) (i.e. R^2: 0.4) (**Figure 18**) when the riverine input was insignificant due the prolonged drought conditions (starting with 2011) preceding this event. The lack of riverine input during this winter event is also indicated by the spatial distribution of alkalinity concentrations within the secondary bay (i.e. Copano) which is the connection between the primary bay and rivers/streams.

Interestingly, TA concentrations are highest at the Aransas River mouth but abruptly decrease towards Aransas Bay, a trend most significant following the long drought (i.e. January) (**Figure 17**).This significant consumption of alkalinity within the Copano Bay could be attributed to calcification by oyster reefs which are present within this bay (Spalt 2017). During optimal calcification salinities (non-flooding and not hypersaline), calcification by oysters is expected to decrease of TA and lead to more positive correlations with salinity (Dickinson et al. 2012). Furthermore, since river input was negligible in January, the elevated TA concentrations measured at the Aransas River mouth could be attributed to groundwater discharge. Subterranean hydraulic gradients often can direct groundwater flow toward river deltas as a result of sediment deposition near the coast (Taniguchi et al. 2008).

On the other hand, the most elevated TA concentrations also measure at the Aransas River mouth in July are likely attributed to river inflow. Following the significant spring rain events the trend observed in January no longer exists, although some TA consumption still occurs with distance from the Aransas River but not as consistent (**Figure 17**). Furthermore, TA levels have decreased significantly in the Aransas Bay stations 10 through 18 (**Figure 29**). Salinity spatial distribution shows that the lower part of Aransas Bay were not impacted as by freshwater inflow in July as Copano and upper Aransas Bay. Lower TA levels in this portions of Aransas Bay contradict with the much more elevated levels during dry conditions. This revers characterizes could be caused by mass displacement of waters in Aransas Bay with water migrating from Copano Bay (of low TA from early spring) towards south, given a strong riverine current. By fall, the TA consumption in Copano Bay is much less evident and concentrations are in general elevated across the estuary (**Figure 17, Figure 29**). Although differences across the

bay system are not as noticeable, there is a significant amount of heterogeneity across bottom and surface waters, especially in the Aransas Bay (**Figure 17, Figure 29**).

Oxygen and Hydrogen Stable Isotopes

The stable isotopes of oxygen and hydrogen in water are important tracers of the global, regional, and local hydrologic cycle. The importance of these isotopes as tracers in water management has been long recognized by the International Atomic Energy Agency (IAEA) which maintains a Global Network of Isotopes in Precipitation (GNIP) providing the isotopic signatures of precipitation worldwide since 1961. δD and $\delta^{18}O$ ratio abundances ranged from –4.35 ‰ to 12.90 ‰ (average 7.84‰ ± 1‰) and –1.09‰ to 1.91‰ (average 0.98 ± 0.1‰), respectively in January with the most enriched ratios measured in Copano Bay (**Figure 30**) and porewaters providing either the most enriched or most depleted ratios in Aransas Bay (Appendix 3). Minimum and maximum δD ratio abundances for July are –7.22 ‰ and 6.96 ‰ (average –0.60 ± 1‰) and –1.79 ‰ and 0.97 ‰ (average –0.57 ± 0.1‰) for $\delta^{18}O$. Copano Bay samples are more depleted in both δD and $\delta^{18}O$ ratio abundances than Aransas Bay especially in the southern portion of Aransas Bay and Redfish Bay (**Figure 30**). By November, Copano Bay surface and porewater samples and Aransas Bay porewaters are again more enriched in both stable isotope ratio abundances with the exception of the station closest to Aransas River which is the most depleted of surface water ratio abundances though still more enriched than July ratios (**Figure 30**). Ratios of δD and $\delta^{18}O$ range from 1.54 ‰ to 6.70 ‰ (average 4.09 ±1‰) and –0.01 ‰ to 1.03 ‰ (average 0.42 ± 1‰), respectively.

Enriched δD and $\delta^{18}O$ ratios are generally correlated with lower amounts of rainfall and higher evaporation rates (Katz et al. 1997) which are the result of both high wind and high temperature conditions. The magnitude of enrichment in heavy isotope composition due to

evaporation was attributed in the past to the Rayleigh Equilibrium Isotope fractionation process which predicts that δD and $\delta^{18}O$ ratios of residual brines become more enriched during evaporation as more of the isotopically depleted $H_2{}^{16}O$ enters the vapor phase (Craig et al. 1963; Lloyd 1966). δD and $\delta^{18}O$ abundances are much more depleted in groundwater around this area (**Figure 31**) with samples collected in May 2015 as part of this study ranging from –25.22 ‰ to –20.76 ‰ (average –22.59 ± 1‰) and –4.96 ‰ to –3.95 ‰ (average –4.41 ± 1), respectively, which are more depleted than nearby groundwater abundances previously reported by Bighash and Murgulet (2015). The average δD and $\delta^{18}O$ for groundwater samples collected as part of their study in summer 2012 (-16.8 ± 1‰ and -0.9 ± 0.1‰, respectively) and spring 2013 (-9.5 ± 1‰ and -1.8 ± 0.1‰, respectively) show a change towards more enriched δD ratios and slightly depleted $\delta^{18}O$ for the 2013 dry spring season. This clearly shows that shallow groundwater isotope signature could be variable as dependent on recharge conditions. It should be noted that the four groundwater wells used as an endmember for current analyses where identified through grouping of samples of similar geochemical characteristics collected from aquifer depths that are likely to interact with surface waters (Spalt 2017).

We attribute the observed depletion of δD and $\delta^{18}O$ ratios in July (**Figure 31**) to the increased freshwater inflow and shallow groundwater discharge following the high precipitation rates in April and May. Conversely, the observed enrichment of δD and $\delta^{18}O$ ratios in January may be attributed to the evaporative effects on surface water and percolating water to aquifers (**Figure 31**). The greater evaporation effect and riverine inputs of freshwater are more evident in the shallower, secondary Copano Bay which exhibits some of the most enriched ratios of both isotopes in January, after a multi-year regional drought, and November, and the most depleted ratios in July after the flooding event. The greater evaporation effect in a shallower, secondary bay is also

observed in a parallel study in the Nueces River Estuary in November/December 2014 (**Figure 32**), where the shallow, secondary Nueces Bay is observed to have more depleted δD and $\delta^{18}O$ ratios than the deeper, primary Corpus Christi Bay. Additionally, the shallow Laguna Madre exhibited more visible evaporation effects with some of the most enriched ratios of both isotopes in porewater during this sampling period (**Figure 32**).

Spatial-temporal Distribution of Phytoplankton and Nutrients

For the purpose of this section, we refer to stations 1-3 as Copano Bay West (CW), stations 4-8 as Copano Bay East (EC), stations 9-12 as Aransas Bay West (AW), stations 13-15 as Aransas Bay North (AN), stations 16-18 as Aransas Bay East (AE), and stations 19-22 as Aransas Bay South (AS). Surface and near bottom chlorophyll-*a* concentrations were consistently low (< 3 µg/l; **Figure 33, Figure 34A**) among sampling zones in January 2015. This is a seasonal characteristic in many coastal systems during the winter months due to physical environmental factors. Both light and temperature have been found to be associated with primary productivity in other Texas estuaries (Longley et al. 1994). Inorganic nitrogen concentrations were generally low throughout the water column in January (**Figure 35, Figure 36A, Figure 37, Figure 38A**), which is likely another factor contributing to low chlorophyll *a* concentrations at this time. Neither ammonium nor nitrate + nitrite concentrations were above 5 µM (**Figure 36, Figure 38**). Orthophosphate concentrations were also low in January 2015 (**Figure 40, Figure 41A**), but the low DIN:DIP (<8) suggest this system was primarily N-limited during this time (**Table 1**). DON concentrations in the water column were an order of magnitude higher than the DIN concentrations in January (**Figure 39A**). Silicate concentrations in the water column ranged from ~5 - 50 µM (**Figure 42, Figure 43A**), which was the lowest of all sampling events. Low concentrations were especially noticeable in Aransas Bay (**Figure 42,**

Figure 43A). These low silicate concentrations may have important implications for phytoplankton growth in the spring months, as diatoms are one of the most common phytoplankton groups in the Mission-Aransas estuary (described in Longley et al. 1994), and diatom growth tends to be supported by physical conditions in late winter/early spring.

Porewater concentrations of most nutrients in January 2015 were higher than in the water column (silicate, DON, orthophosphate, ammonium). This was most pronounced for ammonium, with porewater samples having 100x higher concentrations than the water column (**Figure 36A**). Unlike the other nutrients measured, nitrate + nitrite concentrations were relatively uniform between water column and porewater samples (**Figure 38A**). Similarly, DOC concentrations were similar among surface, near bottom, and porewater samples in January 2015 (**Figure 44, Figure 45A**).

In the July 2015 sampling event, chlorophyll-*a* concentrations were higher than in January, with peak concentrations for most sample zones (the exception is surface water from zone AS, which peaked in November 2015; **Figure 33, Figure 34B**). While physical factors such as increased light and temperature likely play a role in the increased chlorophyll-*a* concentrations during this time, concentrations of nitrate + nitrite, orthophosphate, silicate, and DON were higher in surface and near bottom water samples in July than in January, suggesting increased nutrient availability may play a role as well (**Figure 38B, Figure 39B, Figure 41B, Figure 43B**). However, ammonium concentrations decreased in all surface, near-bottom, and porewater samples in July (< 1 µM; **Figure 36B**) compared to January, and the DIN:DIP decreased as well (**Table 3**), suggesting more severe N-limitation. Ammonium is typically thought to be a preferred nitrogen source for phytoplankton (Dortch 1990), so the preferential uptake of ammonium may be heightened during times of severe N-limitation as seen in July.

Porewater ammonium concentrations in this study (< 1 µM; **Figure 36B**) contrast those measured by Hou et al. (2012) at two sites in Copano Bay in July 2009, which ranged from 60.3-151.2 µM. This may reflect the temporal variability and potential patchiness of porewater nutrient concentrations. It is also important to note that Hou et al. (2012) sampled in 2009, during an extended drought.

By November 2015, chlorophyll-*a* concentrations generally decreased throughout sampling zones (**Figure 33, Figure 34C**). While silicate concentrations throughout the water column and porewater remained similar to those in July, (**Figure 43C**), concentrations of other nutrients throughout the water column and porewater decreased compared to July, and many resembled concentrations from January (**Figure 36C, Figure 38C, Figure 39C, Figure 41C**). For example, ammonium concentrations (**Figure 36C**) were low in the water column but high in porewater samples; this trend was also seen for orthophosphate (**Figure 41C**), albeit less pronounced. Nitrate + nitrite concentrations (**Figure 38C**) also decreased throughout the water column and porewater compared to July, while DIN:DIP in November was still indicative of N limitation (**Table 3**). Additionally, DON concentrations (**Figure 39C**) decreased compared to July, suggesting the potential for DON to have been remineralized by bacteria in the summer months or a higher reliance on organic nutrients for phytoplankton growth in the fall/winter months.

The year-round N-limitation seen in this system aligns with previous work describing nitrogen to be the primary limiting nutrient in Texas estuaries (Longley et al. 1994; Wetz et al. 2017). Inorganic nutrient concentrations in porewater samples, particularly ammonium and orthophosphate, were often 1->100 fold higher than in water column samples, suggesting that porewater may be an intermittently important source for inorganic nutrients to the Mission-

Aransas estuary. The potential importance of porewater as a source for organic nutrient inputs to the system cannot be ruled out either, although DON concentrations in porewater were highly variable in time-space.

Nutrient Fluxes

Groundwater-derived nutrient fluxes were calculated using the radon-derived SGD rate presented in **Table 2**. Groundwater discharge rates vary by season at most locations; however, the average of all SGD rates exhibited very little change between July (40.4 cm/d) and November (39.1 cm/d). Furthermore, nutrient concentrations measured in the interstitial porewater also vary spatially and temporally (**Figure 35Figure 45**).

The estimates suggest that SGD delivers a DIN load of 1.0 millimoles (mM)/day, 151.5 mM/day of DOC, 41.4 mM/day TDN, 60.3 mM/day silicate, and a 1.8 mM/day load of PO_4^{3-} per meter square of bottom sediment into the mid-Copano Bay, North Aransas Bay and Redfish Bay in July. By late fall the estimated nutrient loads increase significantly for some of the nutrients as follows: 56.4 mM/day of DIN load, 234.5 mM/day of DOC, 41.7 mM/day TDN, 88.2 mM/day silicate, and a 1.6 mM/day load of PO_4^{3-} per square meter of bottom sediment. The most significant change in nutrient fluxes between summer and fall is in the form of ammonium. In November, ammonium fluxes at St. Charles Bay mouth (station 13) and Redfish Bay (station 19) are two and three orders of magnitude, respectively, greater than fluxes in July (**Figure 46, Figure 47**). An increase in ammonium fluxes at Mission Bay mouth is also measured but less than an order of magnitude. These values of nitrogen fluxes are consistent with published values in coastal settings (**Table 4**).

When compared to the 2014 Corpus Christi bay study, there is not much fluctuation among seasons other than the ammonium fluxes. In Corpus Christi Bay most nutrient fluxes increased by

an order of magnitude at all locations (Murgulet et al. 2015). This is explained by not only larger groundwater fluxes but also by and increased nutrient concentration measured in porewaters. On the other hand, in the Mission-Aransas Estuary the SGD-derived nutrient fluxes for each station are less dynamic as a function of hydrologic conditions across seasons and more dependent on spatial inputs. The system-wide nutrient fluxes (i.e. season average) appear to be more dependent upon the nutrient concentrations in the interstitial fluids than on the hydrologic conditions. It should be noted however, that any comparison between the two bay systems is not necessarily relevant as sampling and monitoring of SGD occurred during extreme climatologic conditions: Corpus Christi Bay-during an extended period of drought; Mission-Aransas Estuary- following massive rain and flooding (the 2015 flooding).

Copano Bay was found to receive an input of 2.29×10^5 moles of nitrogen per year (M N/yr) in a dry year and 2.37×10^7 M N/yr in a wet year supplied by the Mission River sub-watershed (Mooney and McClelland 2012). Under dry conditions this is substantially less than the input from Aransas River sub-watershed of 2.38×10^6 M N/yr (a factor of 10.4 less). This difference was attributed to lower nutrient loading and less input from point sources (i.e. wastewater treatment) in the Mission River catchment area than the adjacent Aransas River sub-watershed, and is therefore likely more reliant on other sources of nitrogen (Mooney and McClelland 2012). This study shows that SGD-derived nutrient (i.e. TDN) fluxes from solely along the mainland shoreline of the Copano Bay and Aransas Bay (Aransas West to Redfish Bay), are almost four orders of magnitude lower for both July (1.2×10^{-4} M N/yr) and November (1.3×10^{-4} M N/yr) than the Mission River discharge during a wet year. During a dry year, assuming similar SGD rates at the shoreline, the shoreline SGD-derived input of TDN is only by two orders of magnitude lower for both July (1.2×10^{-2} M N/yr) and November (1.3×10^{-2} M

N/yr). However, the nutrient input associated with sediment benthic fluxes that could be significant in the windy area of South Texas should not be ignored. In areas with hydrologic connections between aquifers and bay floor, benthic fluxes could be significantly enhanced increasing nutrient inputs.

A similar rate of SGD could not be applied across the entire bay floor given the large heterogeneities that could impede groundwater flow, likely for extensive areas as seen in the CRP images (Figure CRP). A small subset was selected to demonstrate the potential contribution of groundwater during March, before the massive flooding event. The selected area of approximately 1 km^2 along the Copano Reef could supply 13 to 57 times more TDN than Mission River discharge during a dry year (Spalt 2017). Using the same nutrient flux range compared to a wet year from Mission River discharge, SGD equates to 12–55% of riverine TDN input. This large range in nutrient flux estimation is based on whether the groundwater (lower estimate) or porewater (higher estimate) concentrations are used in the multiplication of the SGD rate as discussed in methods section.

SUMMARY

The main purpose of this study is to advance understanding of groundwater inflows and nutrient transport to bay systems in South Texas for improved Environmental Flow recommendations and nutrient criteria by explicitly incorporating groundwater discharge into the freshwater inflow needs and nutrient budgets to the south Texas coastal embayments. Specifically, this project builds upon current efforts to estimate freshwater and nutrient contributions from groundwater to the Nueces River, Laguna Madre, and Baffin Bay estuaries (projects underway). This study indicates that SGD may have a large impact on biogeochemical cycles of the Mission-

Aransas Estuary. Nutrient, major ion, stable and radiogenic isotopes, and electrical resistivity (ER) measurements were acquired between January to December (late fall), 2015 at twenty-two stations throughout Copano Bay, Aransas Bay, and Redfish Bay. SGD rates were monitored during July and November 2015 at four locations selected based on preliminary observations.

Average groundwater fluxes, measured using continuous Radon-222, ranged from 0.05 (± 0.05) to 71.3 (± 14.0) cm/d in July and from 28.8 (± 3.96) to 88 cm/d (± 18.46) in November. Average concentrations of nutrients in porewater samples collected were as follows: 298.4 µmol/L dissolved organic carbon (Boyd et al.), 283.1 µmol/L total dissolved nitrogen (TDN) 245.1 µmol/L ammonium (NH_4^+), 0.30 µmol/L nitrate + nitrite (N+N as N), 0.08 µmol/L nitrite (NO_2^-), 3.88 µmol/L orthophosphate (PO_4^{3-}), and 141.3 µmol/L silicate (SiO_4^{4-}) in January; and 343.3 µmol/L dissolved organic carbon (Boyd et al.), 80.2 µmol/L total dissolved nitrogen (TDN), 0.49 µmol/L ammonium (NH_4^+), 2.86 µmol/L nitrate + nitrite (N+N as N), 0.49 µmol/L nitrite (NO_2^-), 2.94 µmol/L orthophosphate (PO_4^{3-}), and 126.6 µmol/L silicate (SiO_4^{4-}) in July; and 332.8 µmol/L dissolved organic carbon (Boyd et al.), 75.5 µmol/L total dissolved nitrogen (TDN), 105.1 µmol/L ammonium (NH_4^+), 0.41 µmol/L nitrate + nitrite (N+N as N), 0.08 µmol/L nitrite (NO_2^-), 3.62 µmol/L orthophosphate (PO_4^{3-}), and 157.6 µmol/L silicate (SiO_4^{4-}) in November.

Levels of NH_4, DOC, and silica were significantly higher in samples from SGD sites than in seawater. Measured SGD rates and nutrient concentrations were used to calculate nutrient loads discharged into the study area. The estimates suggest that SGD delivers a dissolved inorganic nitrogen DIN load of 1.0 millimoles (mM)/day, 151.5 mM/day of DOC, 41.4 mM/day TDN, 60.3 mM/day silicate, and a 1.8 mM/day load of PO_4^{3-} per meter square of bottom sediment into the mid-Copano Bay, North Aransas Bay and Redfish Bay in July. By late fall the estimated nutrient loads increase significantly for some of the nutrients as follows: 56.4 mM/day of DIN load, 234.5

mM/day of DOC, 41.7 mM/day TDN, 88.2 mM/day silicate, and a 1.6 mM/day load of PO_4^{3-} per square meter of bottom sediment. Although limited to three SGD monitoring stations, this study indicates that the influence of porewaters on water column nutrient concentrations and microbial respiration, although patchy, may be significant in these systems under the environmental conditions associated with our sampling regime.

This study shows that SGD-derived nutrient (i.e. TDN) fluxes from solely along the mainland shoreline of the Copano Bay and Aransas Bay (Aransas West to Redfish Bay), are almost four orders of magnitude lower for both July (1.2×10^{-4} M N/yr) and November (1.3×10^{-4} M N/yr) than the Mission River discharge during a wet year. During a dry year, assuming similar SGD rates at the shoreline, the shoreline SGD-derived input of TDN is only by two orders of magnitude lower for both July (1.2×10^{-2} M N/yr) and November (1.3×10^{-2} M N/yr). However, the nutrient input associated with sediment benthic fluxes should not be ignored in this area. In areas with hydrologic connections between aquifers and bay floor, benthic fluxes could be significantly enhanced, increasing nutrient inputs. The electrical resistivity imaging and geochemical characteristics reveal a highly heterogeneous substrate and hydrologic conditions that show the need for further investigations to develop an accurate freshwater and nutrient budget to the estuary. Thus, a similar rate of SGD cannot be applied to the entire bay system due to not only large heterogeneities in hydrologic conditions but also because of variable spatial and temporal porewater nutrient concentrations. However, the additional input from coupled deep and recirculated sediment fluxes should not be ignored as it has the potential to exceed the riverine nutrient input, especially in the form of organic nutrients.

REFERENCES

AGI (Advanced Geosciences Inc.), 2016. SuperSting Marine Resistivity. In. https://www.agiusa.com/supersting-marine-resistivity Accessed March 2016.

Alexander, H. D. & K. H. Dunton, 2006. Treated wastewater effluent as an alternative freshwater source in a hypersaline salt marsh: Impacts on salinity, inorganic nitrogen, and emergent vegetation. J Coastal Res 22(2):377-392 doi:10.2112/04-0234.1.

Archie, G. E., 1942. The electrical resistivity log as an aid in determining some reservoir characteristics. T Am I Min Met Eng 146:54-61.

Armstrong, N. E., M. S. Brody, N. Funicelli & National Wetlands Research Center (U.S.), 1987. The ecology of open-bay bottoms of Texas : a community profile. U.S. Dept. of the Interior, Fish and Wildlife Service, Research and Development, National Wetlands Research Center, Washington, DC.

Ashworth, J. B. & J. Hopkins, 1995. Major and minor aquifers of Texas. In: Board, T. W. D. (ed). 69 p.

Baker, E. T., 1979. Stratigraphic and Hydrogeologic Framework of Part of the Coastal Plain of Texas.

Bighash, P. & D. Murgulet, 2015. Application of factor analysis and electrical resistivity to understand groundwater contributions to coastal embayments in semi-arid and hypersaline coastal settings. Sci Total Environ 532:688-701 doi:10.1016/j.scitotenv.2015.06.077.

Boehm, A. B., A. Paytan, G. G. Shellenbarger & K. A. Davis, 2006. Composition and flux of groundwater from a California beach aquifer: Implications for nutrient supply to the surf zone. Cont Shelf Res 26(2):269-282 doi:10.1016/j.csr.2005.11.008.

Bowie, A. R., E. P. Achterberg, P. N. Sedwick, S. Ussher & P. J. Worsfold, 2002. Real-time monitoring of picomolar concentrations of iron(II) in marine waters using automated flow injection-chemiluminescence instrumentation. Environmental Science & Technology 36(21):4600-4607 doi:10.1021/es020045v.

Boyd, P. W., A. J. Watson, C. S. Law, E. R. Abraham, T. Trull, R. Murdoch, D. C. Bakker, A. R. Bowie, K. Buesseler & H. Chang, 2000. A mesoscale phytoplankton bloom in the polar Southern Ocean stimulated by iron fertilization. Nature 407(6805):695-702 doi:10.1038/35037500.

Breier, J. A., C. F. Breier & H. N. Edmonds, 2010. Seasonal dynamics of dissolved Ra isotopes in the semi-arid bays of south Texas. Mar Chem 122(1-4):39-50 doi:10.1016/j.marchem.2010.08.008.

Brown, R. M., N. I. McClelland, R. A. Deininger & R. G. Tozer, 1970. A WATER QUALITY INDEX- DO WE DARE.

Burdige, D. J., S. P. Dhakar & K. H. Nealson, 1992. Effects of Manganese Oxide Mineralogy on Microbial and Chemical Manganese Reduction. Geomicrobiol J 10(1):27-48.

Burnett, W. C., 2003. Radon and radium isotopes as tracers in the coastal ocean. Abstr Pap Am Chem S 226:U81-U81.

Burnett, W. C. & H. Dulaiova, 2003. Estimating the dynamics of groundwater input into the coastal zone via continuous radon-222 measurements. J Environ Radioactiv 69(1-2):21-35 doi:10.1016/S0265-931x(03)00084-5.

Burnett, W. C., M. Taniguchi & J. Oberdorfer, 2001. Measurement and significance of the direct discharge of groundwater into the coastal zone. J Sea Res 46(2):109-116 doi:10.1016/S1385-1101(01)00075-2.

Cable, J. E., J. B. Martin, P. W. Swarzenski, M. K. Lindenberg & J. Steward, 2004. Advection Within Shallow Pore Waters of a Coastal Lagoon, Florida. Ground Water 42(7):1011-1020 doi:10.1111/j.1745-6584.2004.tb02640.x.

Cardenas, M. B., P. B. Zamora, F. P. Siringan, M. R. Lapus, R. S. Rodolfo, G. S. Jacinto, M. L. San Diego-McGlone, C. L. Villanoy, O. Cabrera & M. I. Senal, 2010. Linking regional sources and pathways for submarine groundwater discharge at a reef by electrical resistivity tomography, Rn-222, and salinity measurements. Geophys Res Lett 37 doi:Artn L16401 10.1029/2010gl044066.

Cech, I., C. Kreitler, H. Prichard, A. Holguin & M. Lemma, 1988. Radon Distribution in Domestic Water of Texas. Ground Water 26(5):561-569 doi:10.1111/j.1745-6584.1988.tb00789.x.

Church, T. M., 1996. An underground route for the water cycle. Nature 380(6575):579-580 doi:10.1038/380579a0.

Coale, K. H., K. S. Johnson, S. E. Fitzwater, R. M. Gordon, S. Tanner, F. P. Chavez, L. Ferioli, C. Sakamoto, P. Rogers & F. Millero, 1996. A massive phytoplankton bloom induced by an ecosystem-scale iron fertilization experiment in the equatorial Pacific Ocean. Nature 383(6600):495-501.

Cooke, M. J., L. A. Stem, J. L. Banner, L. E. Mack, T. W. Stafford & R. S. Toomey, 2003. Precise timing and rate of massive late Quaternary soil denudation. Geology 31(10):853-856 doi:10.1130/G19749.1.

Corbett, D. R., W. C. Burnett, P. H. Cable & S. B. Clark, 1998. A multiple approach to the determination of radon fluxes from sediments. J Radioanal Nucl Ch 236(1-2):247-252 doi:10.1007/Bf02386351.

Craig, H., L. I. Gordon & Y. Horibe, 1963. Isotopic Exchange Effects in Evaporation of Water .1. Low-Temperature Experimental Results. J Geophys Res 68(17):5079-&.

Cyronak, T., I. R. Santos, D. V. Erler & B. D. Eyre, 2013. Groundwater and porewater as major sources of alkalinity to a fringing coral reef lagoon (Muri Lagoon, Cook Islands). Biogeosciences 10(4):2467-2480 doi:10.5194/bg-10-2467-2013.

de Baar, H. J., J. T. de Jong, R. F. Nolting, K. R. Timmermans, M. A. van Leeuwe, U. Bathmann, M. R. van der Loeff & J. Sildam, 1999. Low dissolved Fe and the absence of diatom blooms in remote Pacific waters of the Southern Ocean. Mar Chem 66(1):1-34.

Dickinson, G. H., A. V. Ivanina, O. B. Matoo, H. O. Pörtner, G. Lannig, C. Bock, E. Beniash & I. M. Sokolova, 2012. Interactive effects of salinity and elevated CO2 levels on juvenile eastern oysters, Crassostrea virginica. Journal of Experimental Biology 215(1):29-43.

Dickson, A. G., C. L. Sabine & J. R. Christian, 2007. Guide to best practices for ocean CO2 measurements.

Dimova, N., W. C. Burnett, E. P. Horwitz & D. Lane-Smith, 2007. Automated measurement of Ra-224 and Ra-226 in water. Appl Radiat Isotopes 65(4):428-434 doi:10.1016/j.apradiso.2006.10.005.

Dimova, N. T., W. C. Burnett, J. P. Chanton & J. E. Corbett, 2013. Application of radon-222 to investigate groundwater discharge into small shallow lakes. J Hydrol 486:112-122 doi:10.1016/j.jhydrol.2013.01.043.

Dimova, N. T., W. C. Burnett & K. Speer, 2011. A natural tracer investigation of the hydrological regime of Spring Creek Springs, the largest submarine spring system in Florida. Cont Shelf Res 31(6):731-738 doi:10.1016/j.csr.2011.01.010.

Dimova, N. T., P. W. Swarzenski, H. Dulaiova & C. R. Glenn, 2012. Utilizing multichannel electrical resistivity methods to examine the dynamics of the fresh water-seawater interface in two Hawaiian groundwater systems. J Geophys Res-Oceans 117 doi:Artn C02012 10.1029/2011jc007509.

Dortch, Q., 1990. The Interaction between Ammonium and Nitrate Uptake in Phytoplankton. Mar Ecol Prog Ser 61(1-2):183-201 doi:10.3354/meps061183.

Dulaiova, H., W. C. Burnett, J. P. Chanton, W. S. Moore, H. J. Bokuniewicz, M. A. Charette & E. Sholkovitz, 2006. Assessment of groundwater discharges into West Neck Bay, New York, via natural tracers. Cont Shelf Res 26(16):1971-1983 doi:10.1016/j.csr.2006.07.011.

Friedel, S., 2003. Resolution, stability and efficiency of resistivity tomography estimated from a generalized inverse approach. Geophys J Int 153(2):305-316 doi:10.1046/j.1365-246X.2003.01890.x.

Gran, H. H., 1931. On the conditions for the production of plankton in the sea. Conseil Perm Internat pour I'Explor de la Mer Rapp et Proces-Verb 75:37-46.

Green, R. T., J. R. Winterle & J. D. Prikryl, 2008. Discharge From the Edwards Aquifer Through the Leona River Floodplain, Uvalde, Texas1. Wiley Online Library.

Greenwood, W. J., S. Kruse & P. Swarzenski, 2006. Extending electromagnetic methods to map coastal pore water salinities. Ground Water 44(2):292-9 doi:10.1111/j.1745-6584.2005.00137.x.

Grossman, E. L., L. A. Cifuentes & I. M. Cozzarelli, 2002. Anaerobic methane oxidation in a landfill-leachate plume. Environ Sci Technol 36(11):2436-42 doi:10.1021/es015695y.

Guckian, W. J., R. Molina & J. A. Divin, 1988. Soil survey of Refugio County, Texas.

Guo, W. & C. D. Langevin, 2002. User's guide to SEAWAT; a computer program for simulation of three-dimensional variable-density ground-water flow Techniques of Water-Resources Investigations. Supersedes OFR 01-434 edn.

Harred, L. B. & L. Campbell, 2014. Predicting harmful algal blooms: a case study with Dinophysis ovum in the Gulf of Mexico. Journal of Plankton Research:fbu070.

Hou, L. J., M. Liu, S. A. Carini & W. S. Gardner, 2012. Transformation and fate of nitrate near the sediment-water interface of Copano Bay. Cont Shelf Res 35:86-94 doi:10.1016/j.csr.2012.01.004.

Hwang, D. W., G. B. Kim, Y. W. Lee & H. S. Yang, 2005. Estimating submarine inputs of groundwater and nutrients to a coastal bay using radium isotopes. Mar Chem 96(1-2):61-71 doi:10.1016/j.marchem.2004.11.002.

Johnson, T. C., R. J. Versteeg, M. Rockhold, L. D. Slater, D. Ntarlagiannis, W. J. Greenwood & J. Zachara, 2012. Characterization of a contaminated wellfield using 3D electrical resistivity tomography implemented with geostatistical, discontinuous boundary, and known conductivity constraints. Geophysics 77(6):En85-En96 doi:10.1190/Geo2012-0121.1.

Kattner, G., 1999. Storage of dissolved inorganic nutrients in seawater: poisoning with mercuric chloride. Mar Chem 67(1-2):61-66 doi:Doi 10.1016/S0304-4203(99)00049-3.

Katz, B. G., T. B. Coplen, T. D. Bullen & J. H. Davis, 1997. Use of chemical and isotopic tracers to characterize the interactions between ground water and surface water in mantled karst. Ground Water 35(6):1014-1028 doi:10.1111/j.1745-6584.1997.tb00174.x.

Khan, S. & A. R. Kumar, 2012. Interpretation of Groundwater Quality using Correlation and Linear Regression Analysis from Tiruchengode taluk, Namakkal district, Tamilnadu, India. Journal of Chemical and Pharmaceutical Research 4(10):4514-4521.

Kim, G., W. C. Burnett, H. Dulaiova, P. W. Swarzenski & W. S. Moore, 2001. Measurement of Ra-224 and Ra-226 activities in natural waters using a radon-in-air monitor. Environmental Science & Technology 35(23):4680-4683 doi:10.1021/es010804u.

Kim, H. C. & P. A. Montagna, 2012. Effects of climate-driven freshwater inflow variability on macrobenthic secondary production in Texas lagoonal estuaries: A modeling study. Ecol Model 235:67-80 doi:10.1016/j.ecolmodel.2012.03.022.

Knee, K. L., E. Garcia-Solsona, J. Garcia-Orellana, A. B. Boehm & A. Paytan, 2011. Using radium isotopes to characterize water ages and coastal mixing rates: A sensitivity analysis. Limnol Oceanogr-Meth 9:380-395 doi:10.4319/lom.2011.9.380.

Lebreton, B., J. B. Pollack, B. Blomberg, T. A. Palmer, L. Adams, G. Guillou & P. A. Montagna, 2016. Origin, composition and quality of suspended particulate organic matter in relation to freshwater inflow in a South Texas estuary. Estuar Coast Shelf S 170:70-82 doi:10.1016/j.ecss.2015.12.024.

Lee, M. W. & T. S. Collett, 2006. Gas hydrate and free gas saturations estimated from velocity logs on Hydrate Ridge, offshore Oregon, USA. Proc Ocean Drill Program Sci Results 204:1-25 doi:10.2973.

Lloyd, R. M., 1966. Oxygen Isotope Enrichment of Sea Water by Evaporation. Geochim Cosmochim Ac 30(8):801-& doi:10.1016/0016-7037(66)90133-5.

Longley, W. L., G. L. Powell, A. W. Green & T. W. D. Board, 1994. Freshwater inflows to Texas bays and estuaries: ecological relationships and methods for determination of needs. Texas Water Development Board, Austin, TX.

Mace, R. E., W. F. Mullican, E. S. Angle, S. C. Davidson & Texas Water Development Board., 2006. Aquifers of the Gulf coast of Texas. Texas Water Development Board, Austin, Tex.

Manheim, F. T., D. E. Krantz & J. F. Bratton, 2004. Studying Ground Water Under Delmarva Coastal Bays Using Electrical Resistivity. Ground Water 42(7):1052-1068 doi:10.1111/j.1745-6584.2004.tb02643.x.

Martin, J. H., K. H. Coale, K. S. Johnson, S. E. Fitzwater, R. M. Gordon, S. J. Tanner, ... & N. W. Tindale, 1994. Testing the iron hypothesis in ecosystems of the equatorial Pacific-Ocean. Nature 371(6493):123-129 doi:10.1038/371123a0.

Matson, E. A. & M. M. Brinson, 1985. Sulfate Enrichments in Estuarine Waters of North-Carolina. Estuaries 8(3):279-289 doi:10.2307/1351488.

Minz, D., J. L. Flax, S. J. Green, G. Muyzer, Y. Cohen, M. Wagner, B. E. Rittmann & D. A. Stahl, 1999. Diversity of sulfate-reducing bacteria in oxic and anoxic regions of a microbial mat characterized by comparative analysis of dissimilatory sulfite reductase genes. Appl Environ Microbiol 65(10):4666-71.

Montagna, P. A. & C. Ritter, 2006. Direct and indirect effects of hypoxia on benthos in Corpus Christi Bay, Texas, USA. J Exp Mar Biol Ecol 330(1):119-131 doi:10.1016/j.jembe.2005.12.021.

Mooney, R. F. & J. W. McClelland, 2012. Watershed Export Events and Ecosystem Responses in the Mission-Aransas National Estuarine Research Reserve, South Texas. Estuar Coast 35(6):1468-1485 doi:10.1007/s12237-012-9537-4.

Moore, W. S., 1996. Large groundwater inputs to coastal waters revealed by Ra-226 enrichments. Nature 380(6575):612-614 doi:10.1038/380612a0.

Morehead, S., P. Montagna & M. C. Kennicutt, 2008. Comparing fixed-point and probabilistic sampling designs for monitoring the marine ecosystem near McMurdo Station, Ross Sea, Antarctica. Antarct Sci 20(5):471-484 doi:10.1017/S0954102008001326.

Morell, I., E. Gimenez & M. V. Esteller, 1996. Application of principal components analysis to the study of salinization on the Castellon Plain (Spain). Sci Total Environ 177:161-171 doi:10.1016/0048-9697(95)04893-6.

Morton, R. A. & J. McGowen, 1980. Modern depositional environments of the Texas coast. University of Texas at Austin, Bureau of Economic Geology.

Murgulet, D. & G. R. Tick, 2016. Effect of variable-density groundwater flow on nitrate flux to coastal waters. Hydrological Processes 30(2):302-319 doi:10.1002/hyp.10580.

Murgulet, D., M. S. Wetz, A. Douglas, W. McBee, N. Spalt & K. Linares, 2015. Evaluating Groundwater Inflow and Nutrient Transport to Texas Coastal Embayments. Texas General Land Office.

Murray, J., 2004. Chapter 4: Major Ions of Seawater. In: Chemical Oceanography Lecture Notes. University of Washington. https://www.ocean.washington.edu/courses/oc400/Lecture_Notes/CHPT4.pdf Accessed March 2017.

Nelson, K. & P. A. Montagna, 2009. Causes and Monitoring of Hypoxia in Corpus Christi Bay.

NOAA (National Oceanic and Atmospheric Administration), 2014. National Weather Service. In. https://www.ncdc.noaa.gov/.

Nyquist, J. E., P. A. Freyer & L. Toran, 2008. Stream bottom resistivity tomography to map ground water discharge. Ground Water 46(4):561-9 doi:10.1111/j.1745-6584.2008.00432.x.

Palmer, T. A., P. A. Montagna, J. B. Pollack, R. D. Kalke & H. R. DeYoe, 2011. The role of freshwater inflow in lagoons, rivers, and bays. Hydrobiologia 667(1):49-67 doi:10.1007/s10750-011-0637-0.

RCRA SOP, 2009. Protocol for Groundwater/Surface Water Interface Sampling Using a Pore Water Sampler. In: Beneski, B. & E. Bonenfant (eds) Standard Operating Procedure Change Record. Department of Environmental Protection Bureau of Remediation and Waste Management RCRA Program.

Samouelian, A., I. Cousin, A. Tabbagh, A. Bruand & G. Richard, 2005. Electrical resistivity survey in soil science: a review. Soil Till Res 83(2):173-193 doi:10.1016/j.still.2004.10.004.

Santos, I. R., W. C. Burnett, J. Chanton, B. Mwashote, I. G. N. A. Suryaputra & T. Dittmar, 2008. Nutrient biogeochemistry in a Gulf of Mexico subterranean estuary and groundwater-derived fluxes to the coastal ocean. Limnol Oceanogr 53(2):705-718 doi:DOI 10.4319/lo.2008.53.2.0705.

Santos, I. R., J. de Weys, D. R. Tait & B. D. Eyre, 2013. The Contribution of Groundwater Discharge to Nutrient Exports from a Coastal Catchment: Post-Flood Seepage Increases Estuarine N/P Ratios. Estuar Coast 36(1):56-73 doi:10.1007/s12237-012-9561-4.

Schippers, A. & B. B. Jorgensen, 2001. Oxidation of pyrite and iron sulfide by manganese dioxide in marine sediments. Geochim Cosmochim Ac 65(6):915-922 doi:10.1016/S0016-7037(00)00589-5.

Schmidt, D. H. & K. A. Garland, 2012. Bone Dry in Texas: Resilience to Drought on the Upper Texas Gulf Coast. J Plan Lit 27(4):434-445 doi:10.1177/0885412212454013.

Schoenbaechler, C., C. G. Guthrie & Q. Lu, 2011. Coastal Hydrology for the Mission-Aransas Estuary. Austin, Texas, 15.

Shellenbarger, G. G., S. G. Monismith, A. Genin & A. Paytan, 2006. The importance of submarine groundwater discharge to the nearshore nutrient supply in the Gulf of Aqaba (Israel). Limnol Oceanogr 51(4):1876-1886.

Slomp, C. P., J. F. P. Malschaert, L. Lohse & W. VanRaaphorst, 1997. Iron and manganese cycling in different sedimentary environments on the North Sea continental margin. Cont Shelf Res 17(9):1083-1117 doi:10.1016/S0278-4343(97)00005-8.

Spalt, N., 2017. Relating estuarine geology to groundwater discharge at an oyster reed in Copano Bay, TX [Masters Thesis]. Texas A&M University - Corpus Christi.

Street, J. H., K. L. Knee, E. E. Grossman & A. Paytan, 2008. Submarine groundwater discharge and nutrient addition to the coastal zone and coral reefs of leeward Hawai'i. Mar Chem 109(3-4):355-376 doi:10.1016/j.marchem.2007.08.009.

Su, N., W. C. Burnett, K. T. Eller, H. L. MacIntyre, B. Mortazavi, J. D. Liefer & L. Novoveská, 2012. Radon and radium isotopes, groundwater discharge and harmful algal blooms in Little Lagoon, Alabama. Interdisciplinary studies on environmental chemistry 6:329-337.

Sun, Y. & T. Torgersen, 1998. The effects of water content and Mn-fiber surface conditions on Ra-224 measurement by Rn-220 emanation. Mar Chem 62(3-4):299-306 doi:10.1016/S0304-4203(98)00019-X.

Taniguchi, M., T. Ishitobi, J. Chen, S. i. Onodera, K. Miyaoka, W. C. Burnett, R. Peterson, G. Liu & Y. Fukushima, 2008. Submarine groundwater discharge from the Yellow River delta to the Bohai Sea, China. Journal of Geophysical Research: Oceans 113(C6).

Testa, J. M., M. A. Charette, E. R. Sholkovitz, M. C. Allen, A. Rago & C. W. Herbold, 2002. Dissolved iron cycling in the subterranean estuary of a coastal bay: Waquoit Bay, Massachusetts. Biol Bull-Us 203(2):255-6 doi:10.2307/1543427.

Thareja, S., S. Choudhury & P. Trivedi, 2011. Assessment of water quality of Ganga River in Kanpur by using principal components analysis. Adv Appl Sci Res 2(5):84-91.

Toomey III, R., 1993. Late Pleistocene and Holocene faunal and environmental changes at Hall's Cave. Kerr County, Texas [Ph D thesis]: Austin, University of Texas.

Troiani, B. T., A. R. Simms, T. Dellapenna, E. Piper & Y. Yokoyama, 2011. The importance of sea-level and climate change, including changing wind energy, on the evolution of a coastal estuary: Copano Bay, Texas. Mar Geol 280(1-4):1-19 doi:10.1016/j.margeo.2010.10.003.

TWDB (Texas Water Development Board), 2017. Mission-Aransas Estuary. In: Bays & Estuaries. http://www.twdb.texas.gov/surfacewater/bays/major_estuaries/mission_aransas/ Accessed March 2017.

Urquidi-Gaume, M., I. R. Santos & C. Lechuga-Deveze, 2016. Submarine groundwater discharge as a source of dissolved nutrients to an arid coastal embayment (La Paz, Mexico). Environ Earth Sci 75(2) doi:Artn 154 10.1007/S12665-015-4891-8.

USDA (U.S. Department of Agriculture and Natural Resources Conservation Service), 2012. National Soil Survey Handbook, Title 430-VI. In. http://www.nrcs.usda.gov/wps/portal/nrcs/detail/soils/ref/?cid=nrcs142p2_054242 Accessed April 2012.

USGS (Office of Groundwater Branch of Geophysics), 2013. Continuous Resistivity Profiling. In. http://water.usgs.gov/ogw/bgas/crp/ Accessed 9/1/2015 2015.

Voudouris, K., A. Panagopoulos & J. Koumantakis, 2000. Multivariate statistical analysis in the assessment of hydrochemistry of the northern Korinthia prefecture alluvial aquifer system (Peloponnese, Greece). Natural Resources Research 9(2):135-146.

Warnken, K. W., G. A. Gill, L. L. Griffin & P. H. Santschi, 2001. Sediment-water exchange of Mn, Fe, Ni and Zn in Galveston Bay, Texas. Mar Chem 73(3-4):215-231 doi:Doi 10.1016/S0304-4203(00)00108-0.

Warnken, K. W., G. A. Gill, P. H. Santschi & L. L. Griffin, 2000. Benthic exchange of nutrients in Galveston Bay, Texas. Estuaries 23(5):647-661 doi:Doi 10.2307/1352891.

Waterstone & Parsons, 2003. Groundwater availability of the central Gulf Coast aquifer--Numerical simulations to 2050, Central Gulf Coast, Texas.

Wetz, M. S., E. K. Cira, B. Sterba-Boatwright, P. A. Montagna, T. A. Palmer & K. C. Hayes, 2017. Exceptionally high organic nitrogen concentrations in a semi-arid South Texas estuary susceptible to brown tide blooms. Estuarine, Coastal and Shelf Science 188:27-37.

White, P. A., 1988. Measurement of Groundwater Parameters Using Salt-Water Injection and Surface Resistivity. Ground Water 26(2):179-186 doi:10.1111/j.1745-6584.1988.tb00381.x.

Wood, W. W., 1976. Guidelines for collection and field analysis of ground-water samples for selected unstable constituents. US Geological Survey.

Zhang, Y. Z., H. Lin, C. Q. Chen, L. D. Chen, B. Zhang & A. A. Gitelson, 2011. Estimation of chlorophyll-a concentration in estuarine waters: case study of the Pearl River estuary, South China Sea. Environ Res Lett 6(2):024016 doi:Artn 024016 10.1088/1748-9326/6/2/024016.

TABLE LEGEND

Table 1: Average Radon and Radium concentrations and water mass ages by sampling region in January, July and November 2015. Sample regions: Copano Bay West (CW), Copano Bay East (Cech et al.), Aransas Bay West (Boyd et al.), Aransas Bay North (AN), Bay East (AE), Aransas Bay South (AS).

Table 2: Submarine groundwater discharge rates (cm/d) calculated from continuous ^{222}Rn monitoring. November average includes the July SGD rate for station 12 as representative of the presence of negligible SGD areas. Errors are the standard deviation of all measurement intervals (30 minutes) for the monitoring period.

Table 3: Ratio of inorganic nitrogen (ammonium, N+N) to orthophosphate in the water column (surface and near bottom) in January, July and November 2015. Sample regions: Copano Bay West (CW), Copano Bay East (Cech et al.), Aransas Bay West (Boyd et al.), Aransas Bay North (AN), Bay East (AE), Aransas Bay South (AS).

Table 4: Comparison of groundwater and solute fluxes in similar coastal and estuarine settings (expressed in $m^3 \cdot m^{-2} \cdot d^{-1}$ and $mmol \cdot m^2 \cdot d^{-1}$, respectively; modified from Spalt (2017)).

Sampled Regions	^{222}Rn (Bq/m^3)	^{224}Ra (dpm/m^3)	^{226}Ra (dpm/m^3)	$^{224}Ra/^{226}Ra$	Water Mass Ages (days)
January 2015					
CW	39.5	859.9	775.3	1.1	10.6
CE	34.2	470.6	666.2	0.7	14.0
AW	29.4	512.25	787.6	0.7	18.4
AN	48.6	656.6	600.2	1.1	6.7
AE	28.9	335.2	601.5	0.6	18.1
AS	20.9	474.4	404.7	1.2	5.9
Copano Bay Average	36.9	665.2	720.8	0.9	12.3
Aransas Bay Average	32.0	494.6	598.5	0.9	12.3
Event Average	33.6	551.5	639.3	0.9	12.3
July 2015					
CW	31.4	774.1	618.8	1.3	5.3
CE	17.0	537.0	302.9	1.8	3.4
AW	13.2	520.6	506.0	1.0	7.6
AN	6.5	434.0	516.2	0.8	10.4
AE	14.8	–	347.6	–	–
AS	13.0	373.6	353.1	1.1	13.9
Copano Bay Average	24.2	655.5	460.9	1.5	4.4
Aransas Bay Average	11.9	442.7	430.7	1.0	10.6
Event Average	16.0	527.9	440.8	1.2	8.1
November 2015					
CW	29.5	769.7	883.0	0.9	9.3
CE	71.9	531.0	804.0	0.7	16.8
AW	17.6	279.1	719.0	0.4	27.4
AN	46.5	640.1	751.5	0.9	10.2
AE	16.2	1014.9	640.2	1.6	2.8
AS	14.3	502.8	489.0	1.0	8.3
Copano Bay Average	50.7	650.4	843.5	0.8	13.1
Aransas Bay Average	23.6	609.2	649.9	1.0	12.1
Event Average	32.7	622.9	714.5	0.9	12.5

Table 1: Average Radon and Radium concentrations and water mass ages by sampling region in January, July and November 2015. Sample regions: Copano Bay West (CW), Copano Bay East (Cech et al.), Aransas Bay West (Boyd et al.), Aransas Bay North (AN), Bay East (AE), Aransas Bay South (AS).

Station	July	November
7	50.46 ± 5.25	88.02 ± 18.46
12	0.05 ± 0.05	–
13	71.28 ± 14.01	28.81 ± 3.96
19	39.91 ± 7.97	42.75 ± 9.86
Average	40.4	39.9

Table 2: Submarine groundwater discharge rates (cm/d) calculated from continuous ^{222}Rn monitoring. November average includes the July SGD rate for station 12 as representative of the presence of negligible SGD areas. Errors are the standard deviation of all measurement intervals (30 minutes) for the monitoring period.

Date	Sample Region	DIN:DIP
January	CW	4.3
	CE	2.4
	AW	2.8
	AN	7.8
	AE	7.2
	AS	7.4
July	CW	0.7
	CE	1.0
	AW	0.1
	AN	0.5
	AE	0.9
	AS	2.9
November	CW	3.3
	CE	2.2
	AW	1.2
	AN	1.2
	AE	0.5
	AS	3.0

Table 3: Ratio of inorganic nitrogen (ammonium, N+N) to orthophosphate in the water column (surface and near bottom) in January, July and November 2015. Sample regions: Copano Bay West (CW), Copano Bay East (Cech et al.), Aransas Bay West (Boyd et al.), Aransas Bay North (AN), Bay East (AE), Aransas Bay South (AS).

Site	SGD	DOC	TDN	NH_4^+	DIN	Reference
Eilat, Israel	0.26–0.60	–	–	–	2.9–10	(Shellenbarger et al. 2006)
Huntington Beach, USA	0.06–0.92	–	–	–	0.7–12	(Boehm et al. 2006)
Jeju, South Korea	0.44	–	–	–	21.4	(Hwang et al. 2005)
Kuauaiwa, USA	0.37–0.39	–	–	–	6.8–7.0	(Street et al. 2008)
Balandra, Mexico	0.18	–	–	–	2.07–51.6	(Urquidi-Gaume et al. 2016)
Merito, Mexico	0.02–0.18	–	–	–	2.13–4.72	(Urquidi-Gaume et al. 2016)
Tuckean Swamp, Australia	–	–	–	35	3.6	(Santos et al. 2013)
Turkey Point, Florida	0.11	34.3	8.23	4.81	1.13	(Santos et al. 2008)
Muri Lagoon, Cook Islands	–	–	–	–	–	(Cyronak et al. 2013)
Galveston Bay, USA	–	–	–	0.45–2.2	–	(Warnken et al. 2001; Warnken et al. 2000)
Mission-Aransas Estuary, USA	0.40–0.88	49–450	9–92	0.2–156	0.5–156	This Study

Table 4: Comparison of groundwater and solute fluxes in similar coastal and estuarine settings (expressed in $m^3 \cdot m^{-2} \cdot d^{-1}$ and $mmol \cdot m^2 \cdot d^{-1}$, respectively; modified from Spalt (2017)).

FIGURE LEGEND

Figure 1: Study area showing stream gauges for Aransas River, Mission River, and Copano Creek (yellow triangles), all groundwater wells sampled (green dots), and the geochemically similar wells (red squares) used for analysis.

Figure 2: Image showing the continuous recording and storing of data from a GPS receiver using the SuperSting Marine. The SuperSting Marine continuously records and stores data from a GPS receiver. Current is injected every 3 seconds and 8 apparent resistivity values representing 8 depth levels are read for each current injection. Depth of penetration depends on length of the cable and array type (typically approximately 20% of the electrode spread length) (AGI 2016).

Figure 3: January sampling stations with locations where porewater and radium were sampled are identified.

Figure 4: July sampling stations with locations where porewater and radium were sampled are identified.

Figure 5: November sampling stations with locations where porewater and radium were sampled are identified.

Figure 6: Daily mean streamflow (m^3/s) for Aransas River near Skidmore (08189700), Mission River at Refugio (08189500), and Copano Creek near Refugio (08189200), TX. Sampling periods are highlighted in blue.

Figure 7: Monthly mean precipitation (mm) at Copano East Monitoring Station.

Figure 8: Conceptual model showing the radon inventory per unit area for estimating groundwater discharge (Burnett and Dulaiova 2003).

Figure 9: Study site and continuous resistivity transects. The inset shows transects from the study in the geological influences on groundwater discharge.

Figure 10: Continuous Resistivity Profile (CRP) transects. A-A' = Copano West. B-B' = Copano East. C-C' = Aransas West. D-D' = Aransas North and Aransas East.

Figure 11: Radon concentrations (Bq/m^3) by station in surface ("S") and near bottom ("B") waters of Copano Bay and Aransas Bay for January, July, and November 2015.

Figure 12: Average radium-226 activities (dpm/m^3) in Copano Bay and Aransas Bay in January, July, and November 2015.

Figure 13: Average radium-224 activities (dpm/m^3) in Copano Bay and Aransas Bay in January, July, and November 2015.

Figure 14: January radium ages (days) derived from $^{224}Ra/^{226}Ra$ activity ratios of surface water and shallow groundwater. Average wind direction is indicated by the arrows. Average wind speed was 1.2 m/s.

Figure 15: July radium ages (days) derived from $^{224}Ra/^{226}Ra$ activity ratios of surface water and shallow groundwater. Average wind direction is indicated by the arrows. Average wind speed was 6.5 m/s.

Figure 16: November radium ages (days) derived from $^{224}Ra/^{226}Ra$ activity ratios of surface water and shallow groundwater. Average wind direction is indicated by the arrows. Average wind speed was 1.5 m/s.

Figure 17: Mass ratios of sulfate to chlorinity (SO_4^-/Cl^-) and total alkalinity (μmol/kg as HCO_3^-) to chlorinity (TA/Cl^-) by station. The horizontal line represents the typical seawater ratios at 35 parts per million salinity.

Figure 18: Relationships of mass ratios of sulfate to chlorinity (SO_4^-/Cl^-) with chloride (Cl^-) and total alkalinity (μmol/kg as HCO_3^-) to salinity (psu).

Figure 19: Cross-correlation between sulfate (mg/L) and chloride (mg/L) for January, July, and November.

Figure 20: Spatial distribution using Inverse Distance Weighted (IDW) interpolation of salinity (psu) for January, July, and November. Surface = 0.2m below the air-water interface. Bottom = 0.2m above the sediment-water interface.

Figure 21: Mass ratios of magnesium to chlorinity (Mg^{2+}/Cl^-) and total iron to chlorinity (Fe/Cl^-) by station. The horizontal line represents the typical seawater ratios at 35 parts per million salinity.

Figure 22: Mass ratios of potassium to chlorinity (K^+/Cl^-) and calcium to chlorinity (Ca^{2+}/Cl^-) by station. The horizontal line represents the typical seawater ratios at 35 parts per million salinity.

Figure 23: Relationships of mass ratios of magnesium to chlorinity (Mg^{2+}/Cl^-) and total iron to chlorinity (Fe/Cl^-) with chloride (Cl^-).

Figure 24: Relationships of mass ratios of potassium to chlorinity (K^+/Cl^-) and calcium to chlorinity (Ca^{2+}/Cl^-) with chloride (Cl^-).

Figure 25: Spatial distribution using Inverse Distance Weighted (IDW) interpolation of Dissolved Oxygen (mg/L) and pH for January, July, and November.

Figure 26: Mass ratios of sodium to chlorinity (Na^+/Cl^-) and bromide to chlorinity (Br^-/Cl^-) by station. The horizontal line represents the typical seawater ratios at 35 parts per million salinity.

Figure 27: Relationships of mass ratios of sodium to chlorinity (Na^+/Cl^-) and bromide to chlorinity (Br^-/Cl^-) with chloride (Cl^-). No bromide data was available for January.

Figure 28: Cross-correlation between manganese (mg/L) and chloride (mg/L) for January, July, and November 2015.

Figure 29: Spatial distribution using Inverse Distance Weighted (IDW) interpolation of Total Alkalinity (TA, µmol/L as HCO_3^-) for January, July, and November. Surface = 0.2m below the air-water interface. Bottom = 0.2m above the sediment-water interface.

Figure 30: Spatial distribution using Inverse Distance Weighted (IDW) interpolation of δD (‰ VSMOW) and $\delta^{18}O$ (‰ VSMOW) for January, July, and November.

Figure 31: Cross-correlation between δD (‰ V-SMOW) and $\delta^{18}O$ (‰ V-SMOW) for the study period. GMWL = Global Meteoric Water Line (Craig et al. 1963). WMWL = Waco Meteoric Water Line.

Figure 32: Cross-correlation of δD (‰ V-SMOW) and $\delta^{18}O$ (‰ V-SMOW) showing the comparison of primary and secondary bays in the Nueces River and Mission-Aransas Estuaries. GMWL = Global Meteoric Water Line (Craig et al. 1963). WMWL = Waco Meteoric Water Line.

Figure 33: Spatial distribution using Inverse Distance Weighted (IDW) interpolation of Chlorophyll-a (µg/L) for January, July, and November. Surface = 0.2m below the air-water interface. Bottom = 0.2m above the sediment-water interface.

Figure 34: Chlorophyll-a concentration (µg/L) in surface ("S") and near bottom ("B") waters of Copano Bay and Aransas Bay in January 2015 (A), July 2015 (B), and November 2015 (C).

Figure 35: Spatial distribution using Inverse Distance Weighted (IDW) interpolation of Ammonium (NH_4, µmol/L) for January, July, and November. Surface = 0.2m below the air-water interface. Bottom = 0.2m above the sediment-water interface.

Figure 36: Ammonium concentrations (µM) in surface ("S"), near bottom ("B"), and porewater ("P") of Copano Bay and Aransas Bay in January 2015 (A), July 2015 (B), and November 2015 (C).

Figure 37: Spatial distribution using Inverse Distance Weighted (IDW) interpolation of Nitrate+Nitrite (N+N, μmol/L) for January, July, and November. Surface = 0.2m below the air-water interface. Bottom = 0.2m above the sediment-water interface.

Figure 38: Nitrate + nitrite concentrations (μM) in surface ("S"), near bottom ("B"), and porewater ("P") of Copano Bay and Aransas Bay in January 2015 (A), July 2015 (B), and November 2015 (C).

Figure 39: Dissolved organic nitrogen concentrations (μM) in surface ("S"), near bottom ("B"), and porewater ("P") of Copano Bay and Aransas Bay in January 2015 (A), July 2015 (B), and November 2015 (C).

Figure 40: Spatial distribution using Inverse Distance Weighted (IDW) interpolation of O-Phosphate (PO_4, μmol/L) for January, July, and November. Surface = 0.2m below the air-water interface. Bottom = 0.2m above the sediment-water interface.

Figure 41: Orthophosphate concentrations (μM) in surface ("S"), near bottom ("B"), and porewater ("P") of Copano Bay and Aransas Bay in January 2015 (A), July 2015 (B), and November 2015 (C).

Figure 42: Spatial distribution using Inverse Distance Weighted (IDW) interpolation of Silicate (SiO_4, μmol/L) for January, July, and November. Surface = 0.2m below the air-water interface. Bottom = 0.2m above the sediment-water interface.

Figure 43: Silicate concentrations (μM) in surface ("S"), near bottom ("B"), and porewater ("P") of Copano Bay and Aransas Bay in January 2015 (A), July 2015 (B), and November 2015 (C).

Figure 44: Spatial distribution using Inverse Distance Weighted (IDW) interpolation of Dissolved Inorganic Carbon (DOC, μmol/L) for January, July, and November. Surface = 0.2m below the air-water interface. Bottom = 0.2m above the sediment-water interface.

Figure 45: Dissolved organic carbon concentrations (μM) in surface ("S"), near bottom ("B"), and porewater ("P") of Copano Bay and Aransas Bay in January 2015 (A), July 2015 (B), and November 2015 (C).

Figure 46: Groundwater nutrient fluxes (μmol/m·d) at Mission Bay Mouth (station 7), St. Charles Bay mouth (station 13), and Redfish Bay (station 19) for July 2015.

Figure 47: Groundwater nutrient fluxes (μmol/m·d) at Mission Bay Mouth (station 7), St. Charles Bay mouth (station 13), and Redfish Bay (station 19) for November 2015.

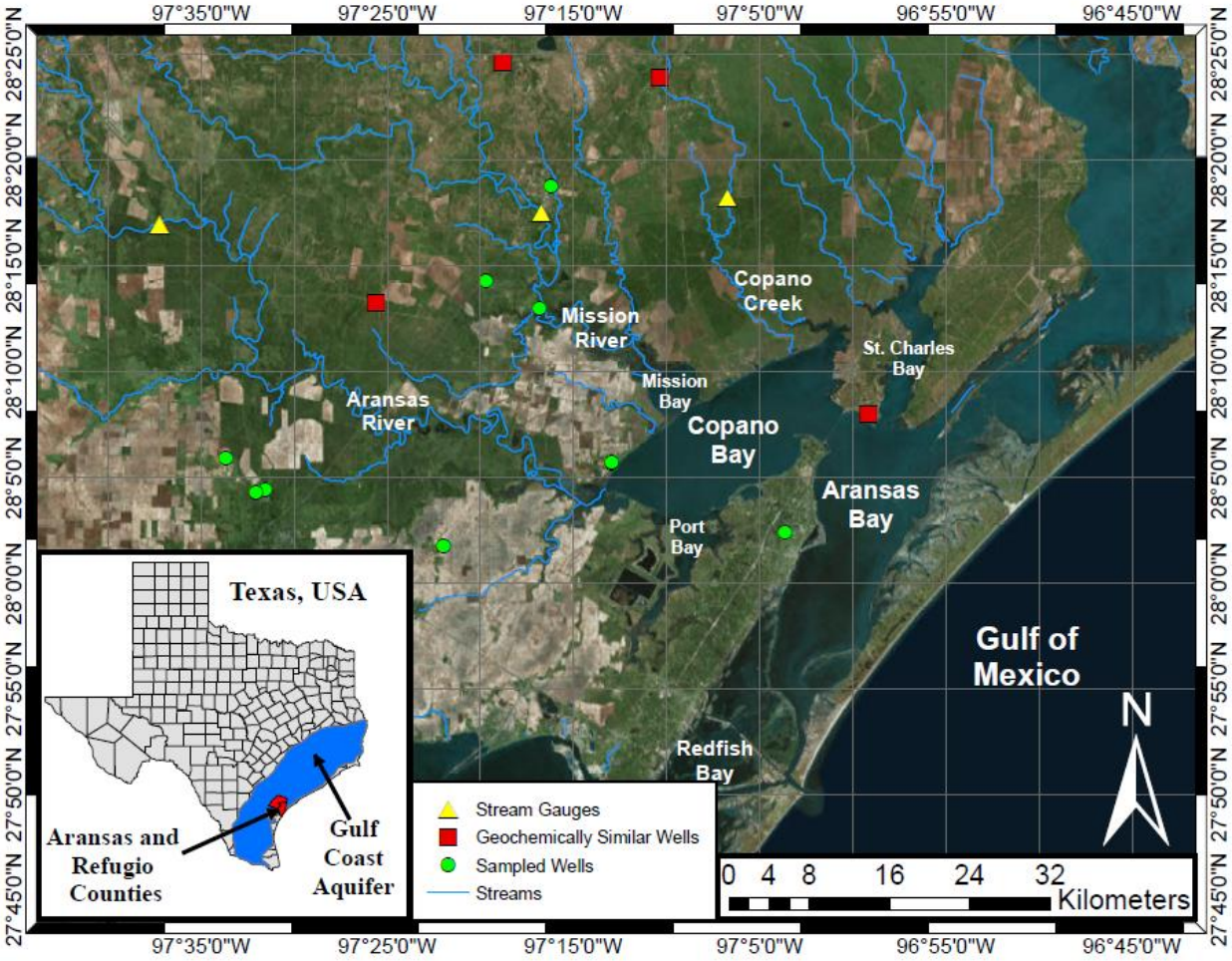

Figure 1: Study area showing stream gauges for Aransas River, Mission River, and Copano Creek (yellow triangles), all groundwater wells sampled (green dots), and the geochemically similar wells (red squares) used for analysis.

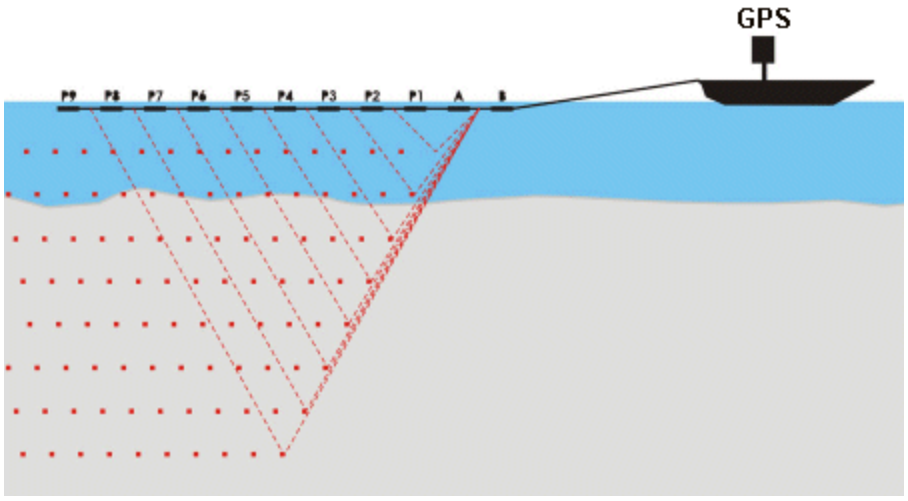

Figure 2: Image showing the continuous recording and storing of data from a GPS receiver using the SuperSting Marine. The SuperSting Marine continuously records and stores data from a GPS receiver. Current is injected every 3 seconds and 8 apparent resistivity values representing 8 depth levels are read for each current injection. Depth of penetration depends on length of the cable and array type (typically approximately 20% of the electrode spread length) (AGI 2016).

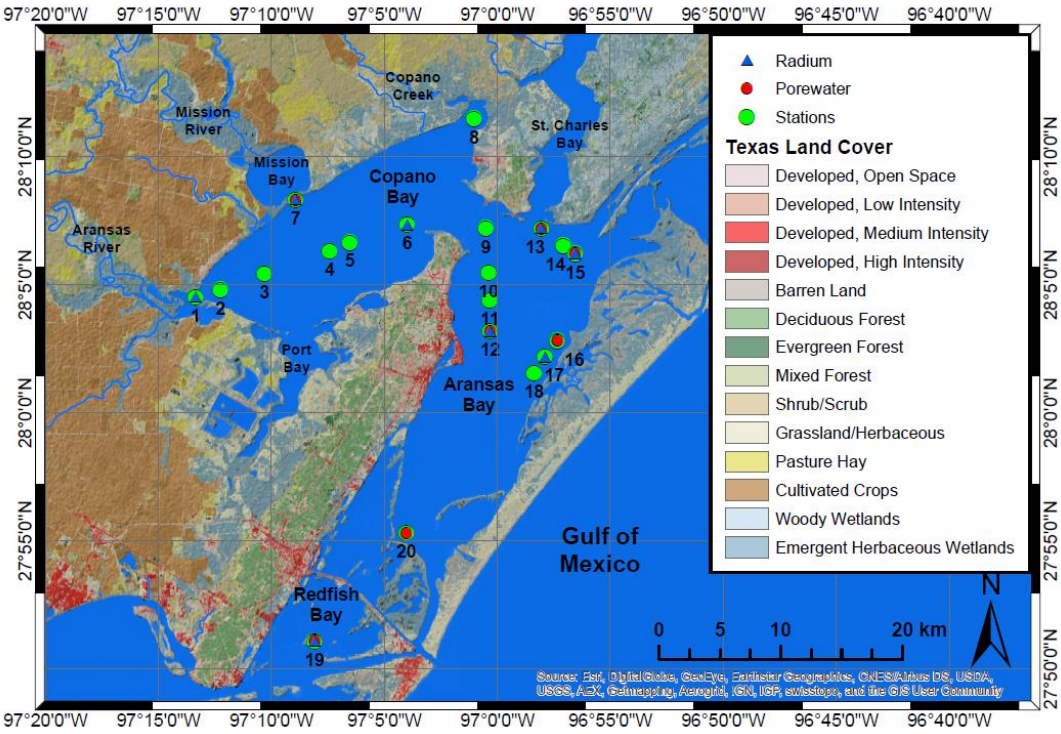

Figure 3: January sampling stations with locations where porewater and radium were sampled are identified.

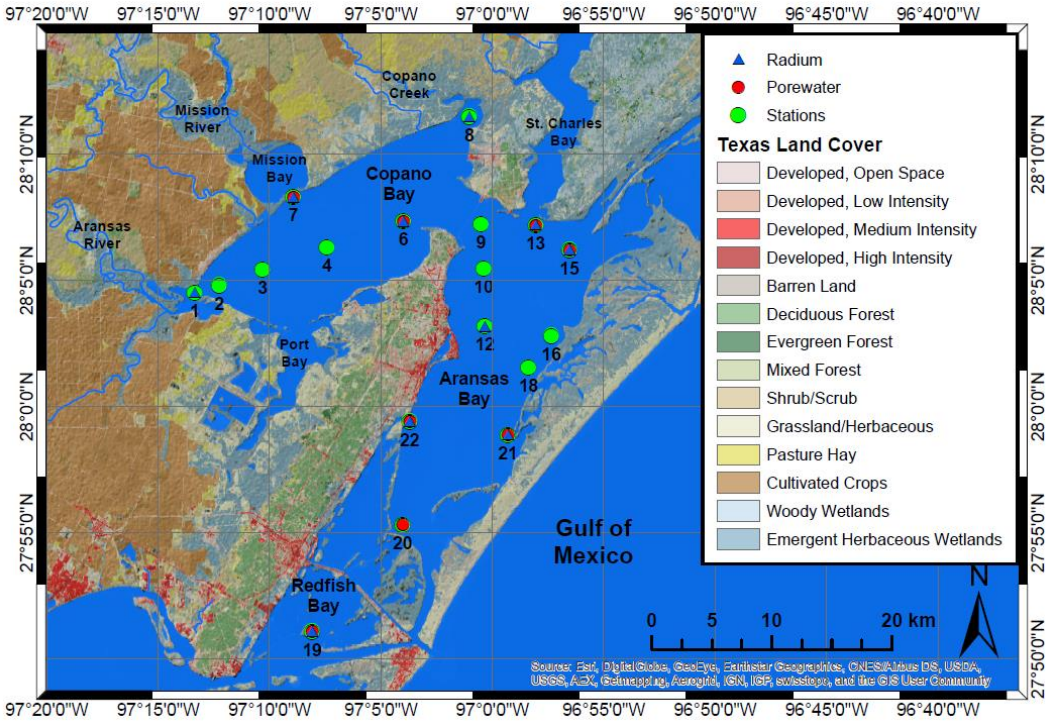

Figure 4: July sampling stations with locations where porewater and radium were sampled are identified.

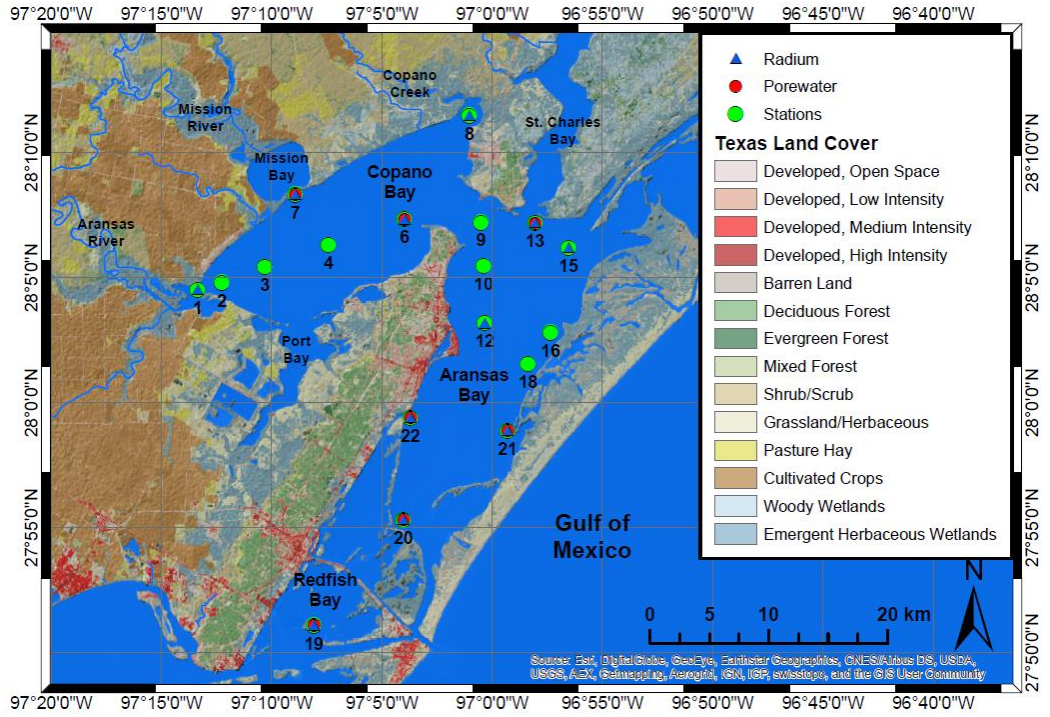

Figure 5: November sampling stations with locations where porewater and radium were sampled are identified.

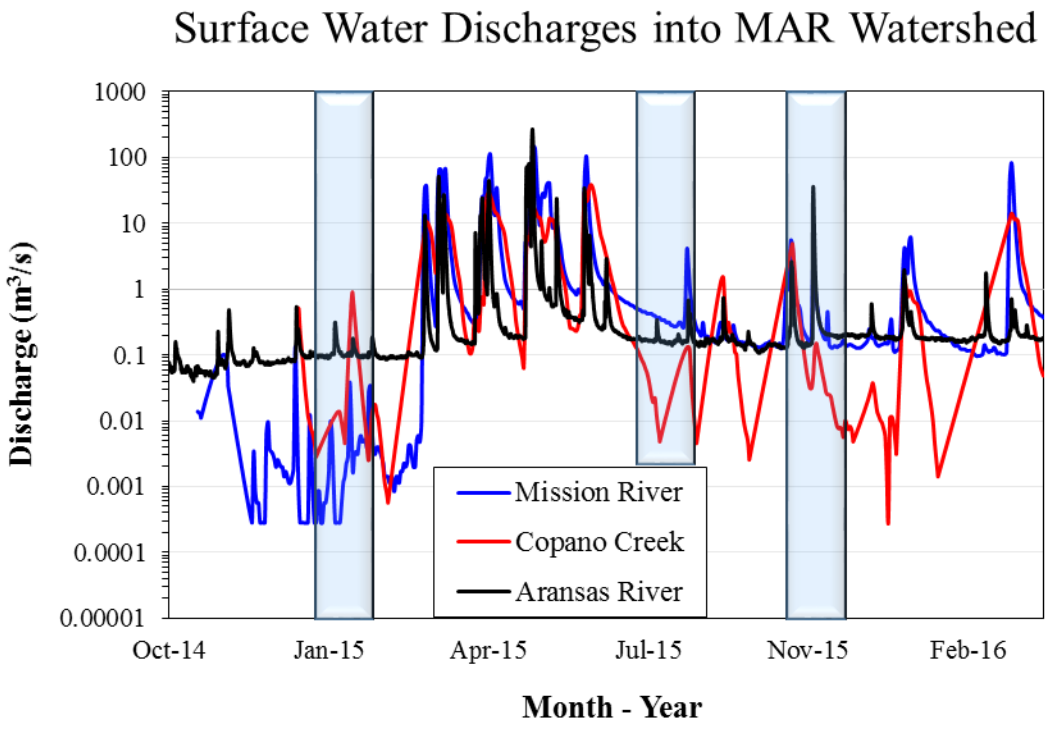

Figure 6: Daily mean streamflow (m^3/s) for Aransas River near Skidmore (08189700), Mission River at Refugio (08189500), and Copano Creek near Refugio (08189200), TX. Sampling periods are highlighted in blue.

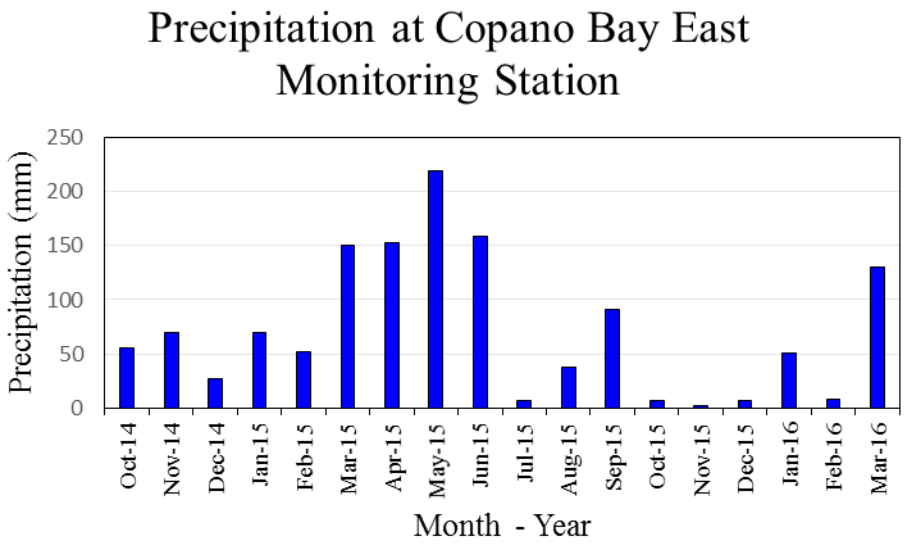

Figure 7: Monthly mean precipitation (mm) at Copano East Monitoring Station.

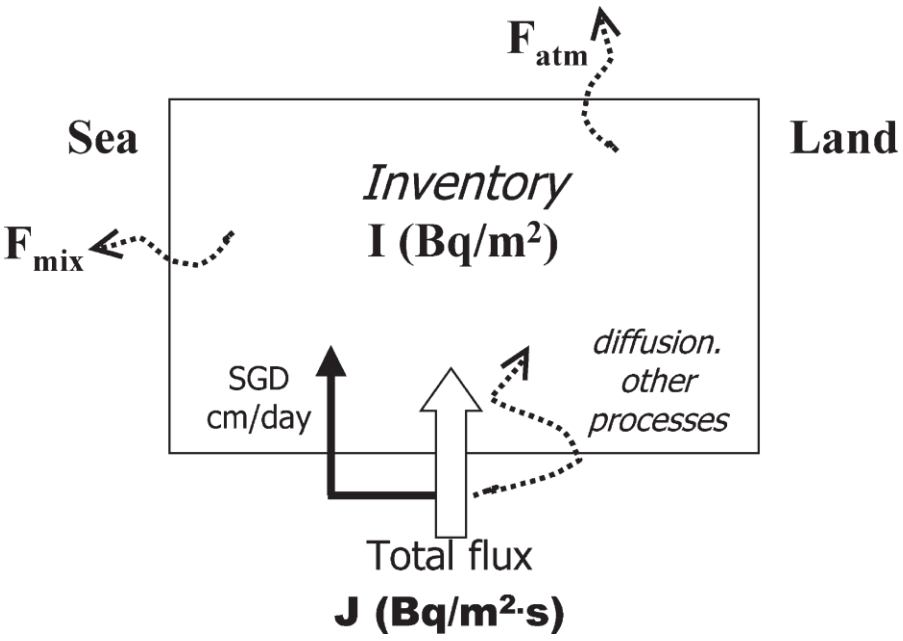

Figure 8: Conceptual model showing the radon inventory per unit area for estimating groundwater discharge (Burnett and Dulaiova 2003).

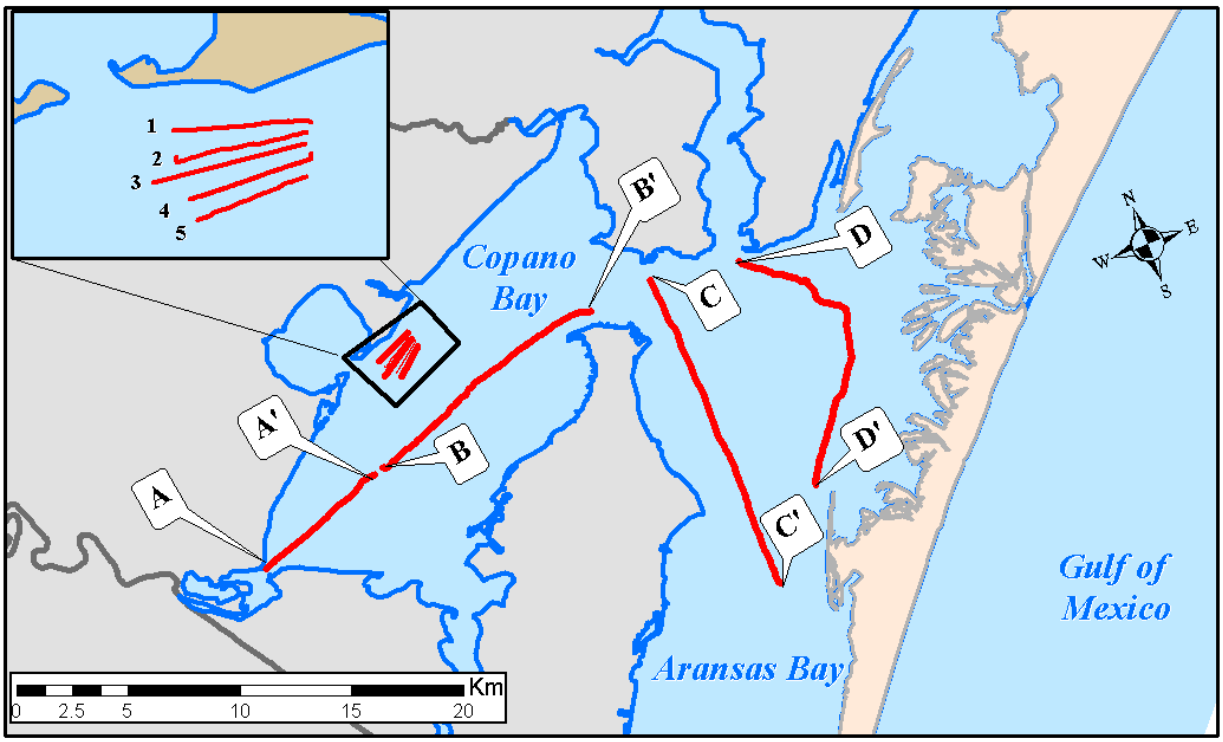

Figure 9: Study site and continuous resistivity transects. The inset shows transects from the study in the geological influences on groundwater discharge.

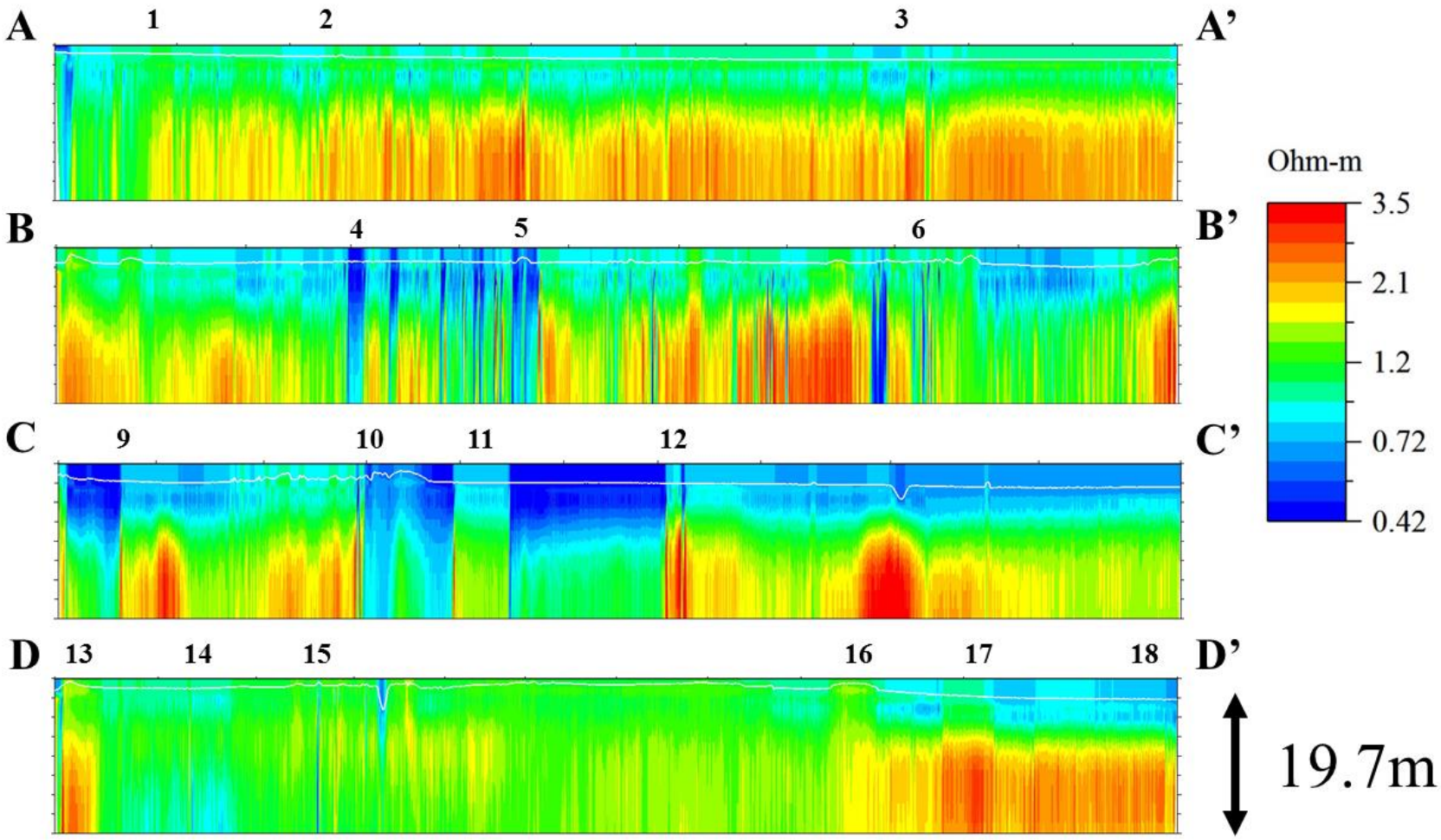

Figure 10: Continuous Resistivity Profile (CRP) transects. A-A' = Copano West. B-B' = Copano East. C-C' = Aransas West. D-D' = Aransas North and Aransas East.

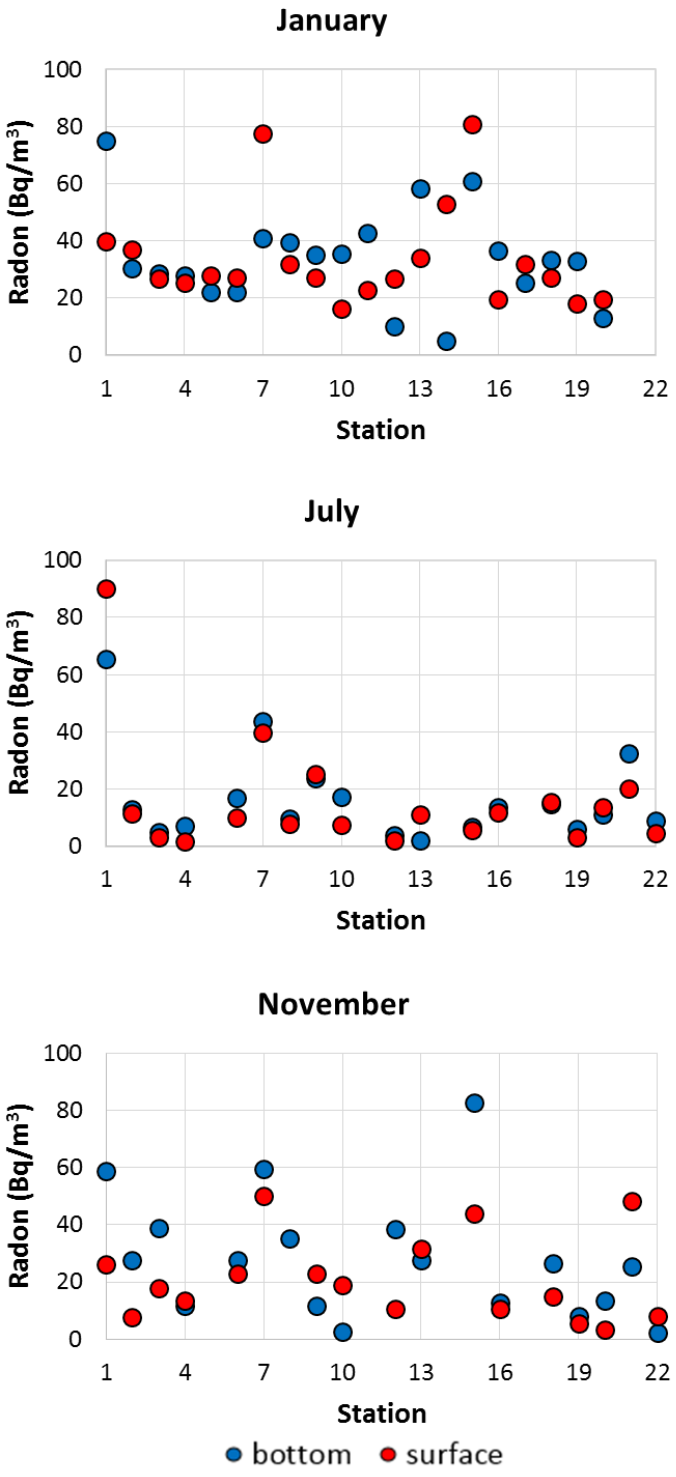

Figure 11: Radon concentrations (Bq/m^3) by station in surface ("S") and near bottom ("B") waters of Copano Bay and Aransas Bay for January, July, and November 2015.

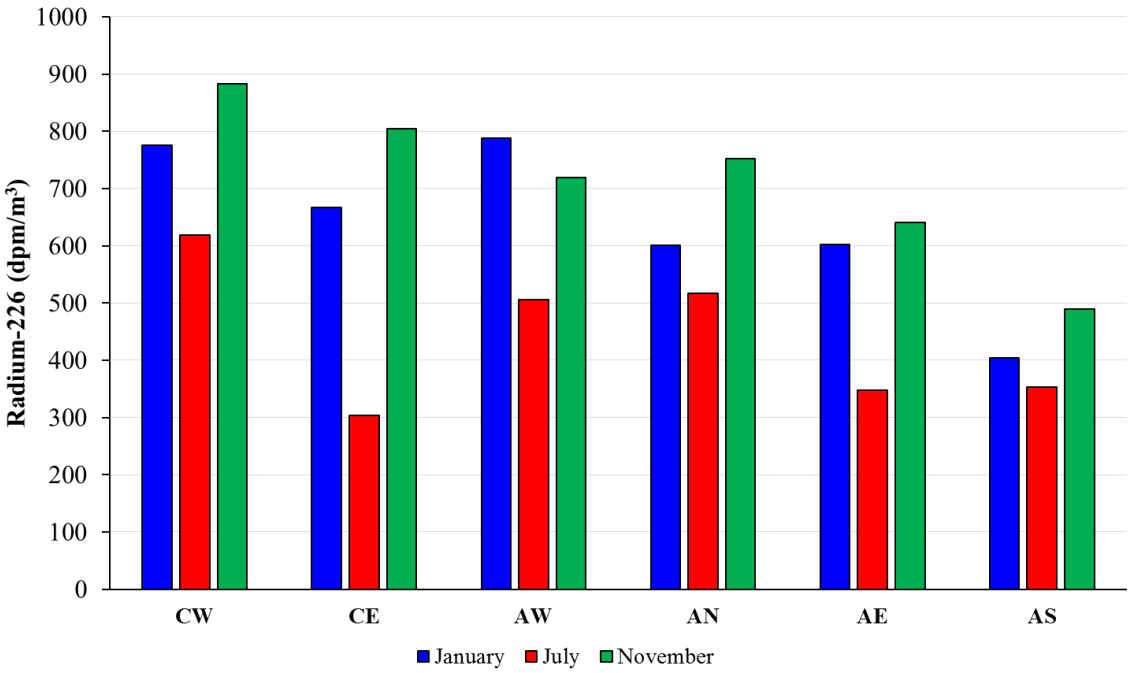

Figure 12: Average radium-226 activities (dpm/m^3) in Copano Bay and Aransas Bay in January, July, and November 2015.

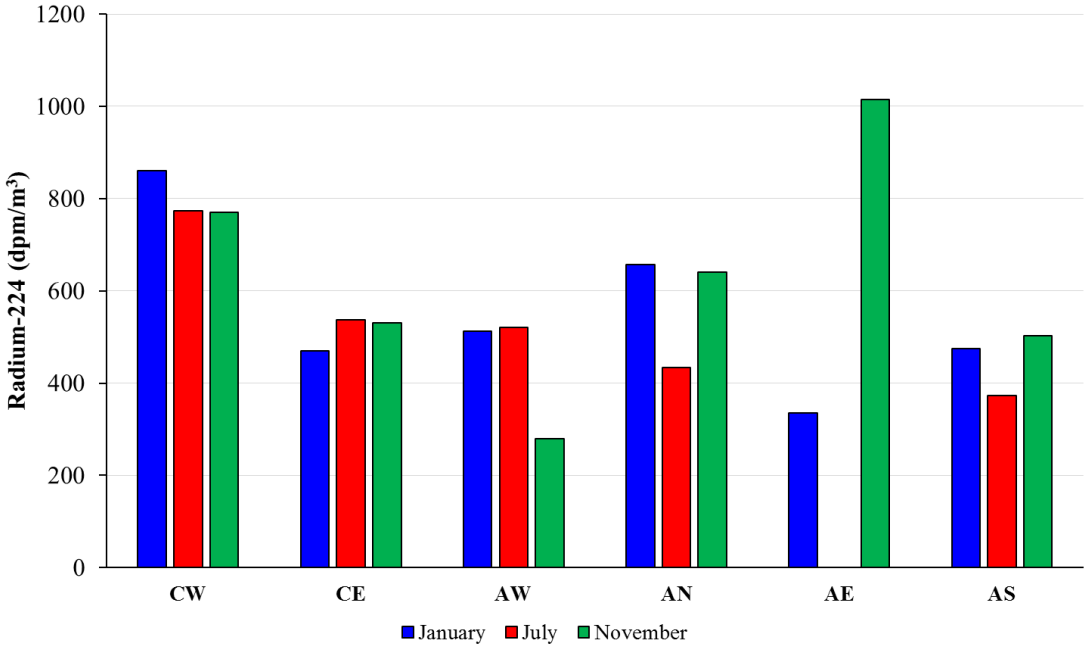

Figure 13: Average radium-224 activities (dpm/m^3) in Copano Bay and Aransas Bay in January, July, and November 2015.

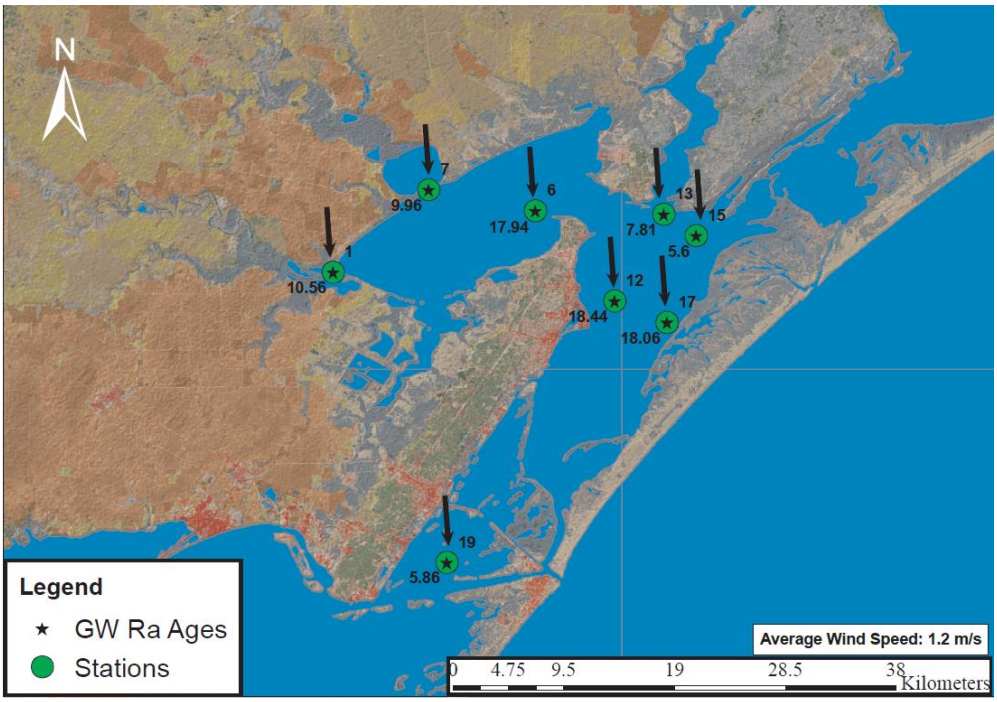

Figure 14: January radium ages (days) derived from $^{224}Ra/^{226}Ra$ activity ratios of surface water and shallow groundwater. Average wind direction is indicated by the arrows. Average wind speed was 1.2 m/s.

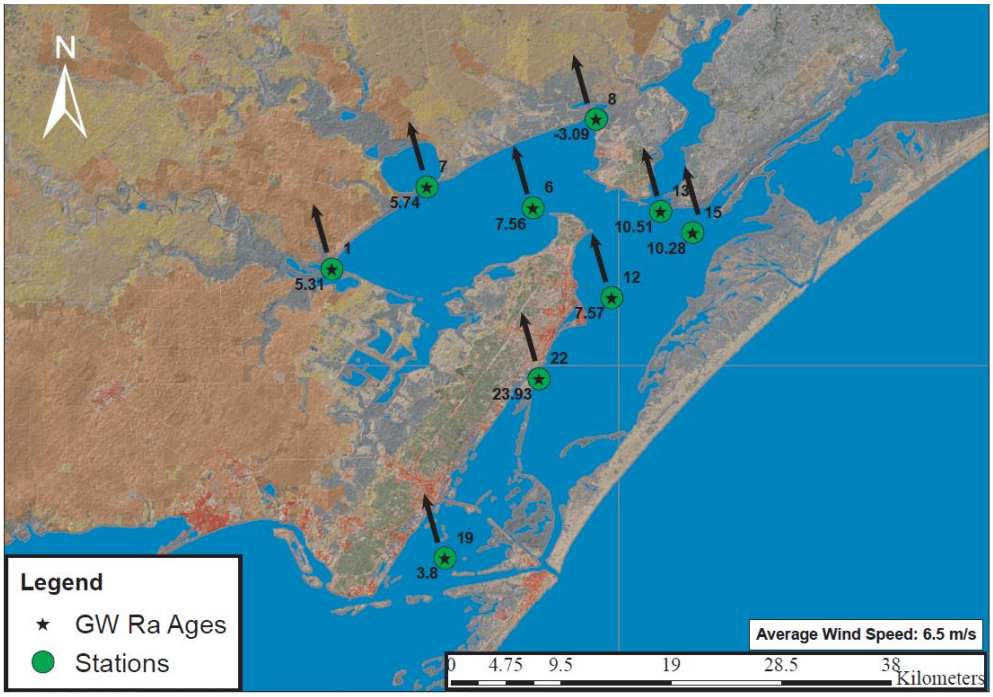

Figure 15: July radium ages (days) derived from $^{224}Ra/^{226}Ra$ activity ratios of surface water and shallow groundwater. Average wind direction is indicated by the arrows. Average wind speed was 6.5 m/s.

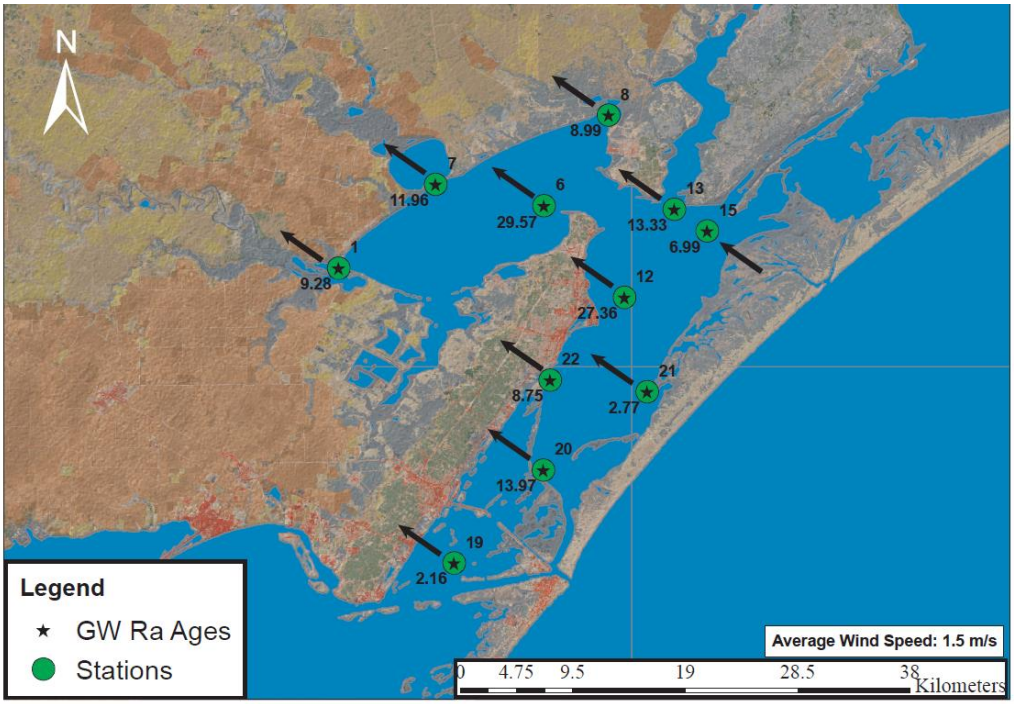

Figure 16: November radium ages (days) derived from $^{224}Ra/^{226}Ra$ activity ratios of surface water and shallow groundwater. Average wind direction is indicated by the arrows. Average wind speed was 1.5 m/s.

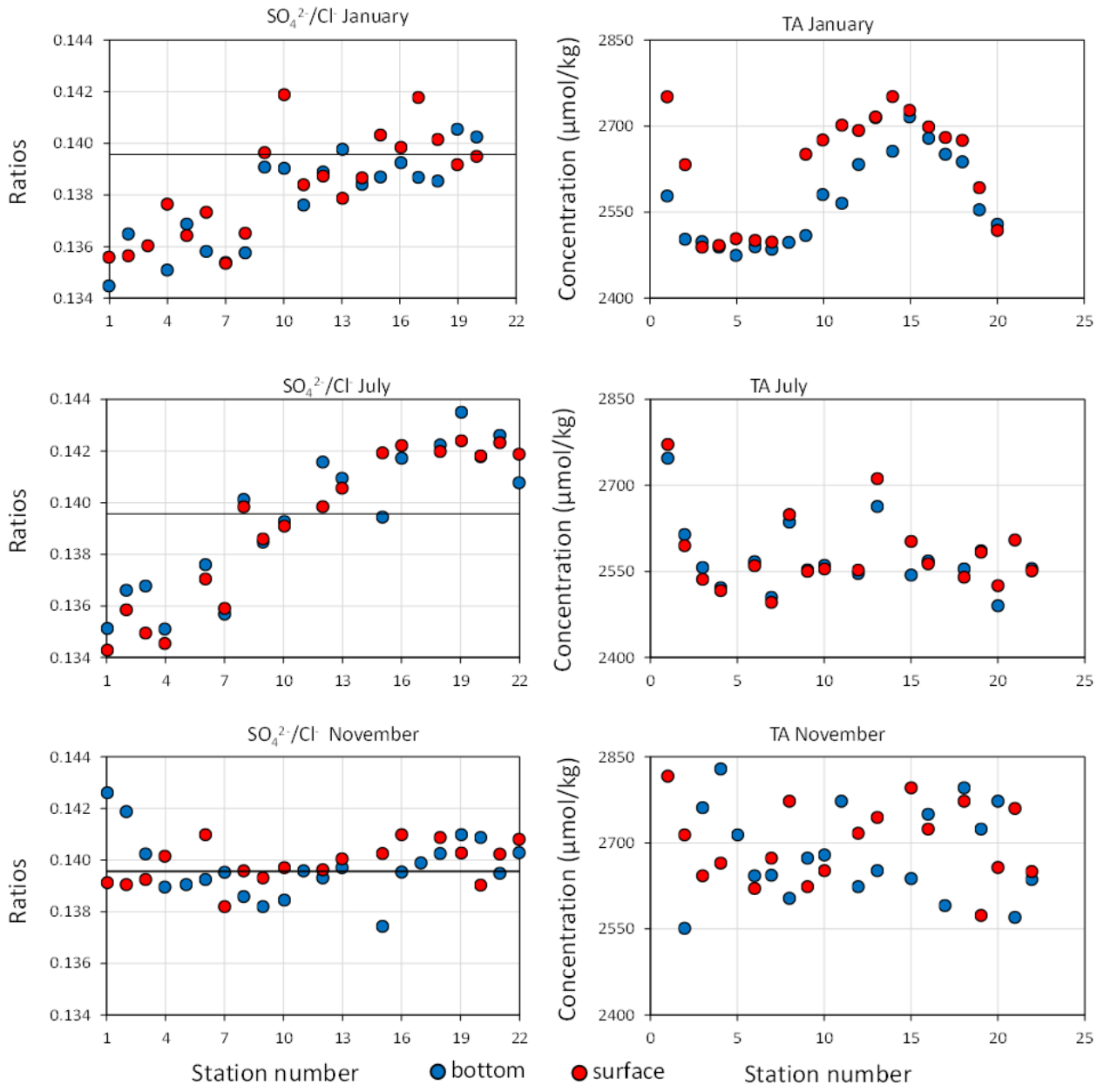

Figure 17: Mass ratios of sulfate to chlorinity (SO_4^-/Cl^-) and total alkalinity (µmol/kg as HCO_3^-) to chlorinity (TA/Cl^-) by station. The horizontal line represents the typical seawater ratios at 35 parts per million salinity.

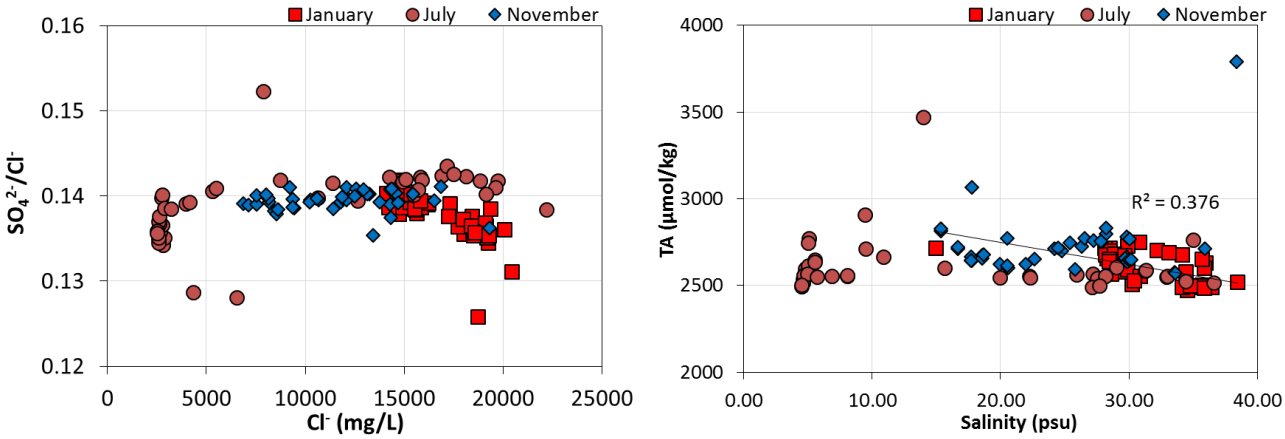

Figure 18: Relationships of mass ratios of sulfate to chlorinity (SO_4^-/Cl^-) with chloride (Cl^-) and total alkalinity (µmol/kg as HCO_3^-) to salinity (psu).

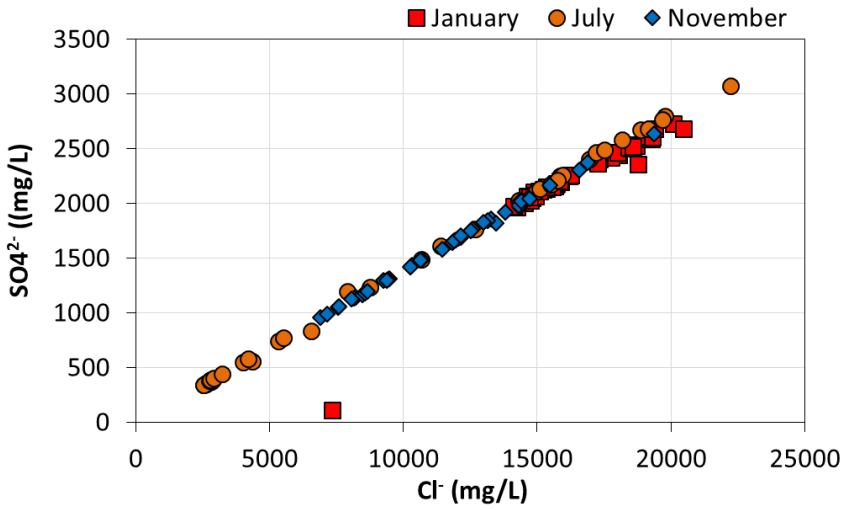

Figure 19: Cross-correlation between sulfate (mg/L) and chloride (mg/L) for January, July, and November.

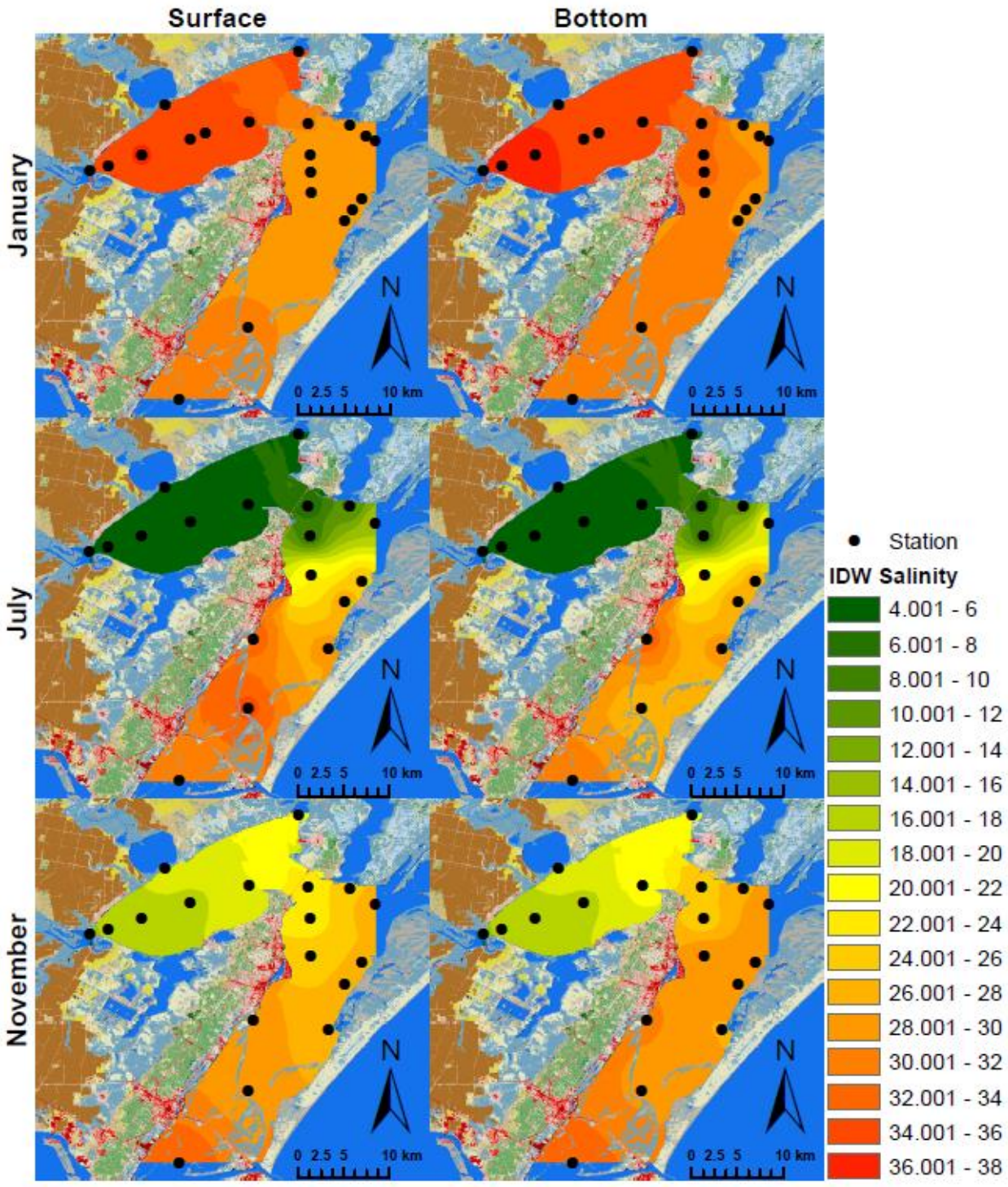

Figure 20: Spatial distribution using Inverse Distance Weighted (IDW) interpolation of salinity (psu) for January, July, and November. Surface = 0.2m below the air-water interface. Bottom = 0.2m above the sediment-water interface.

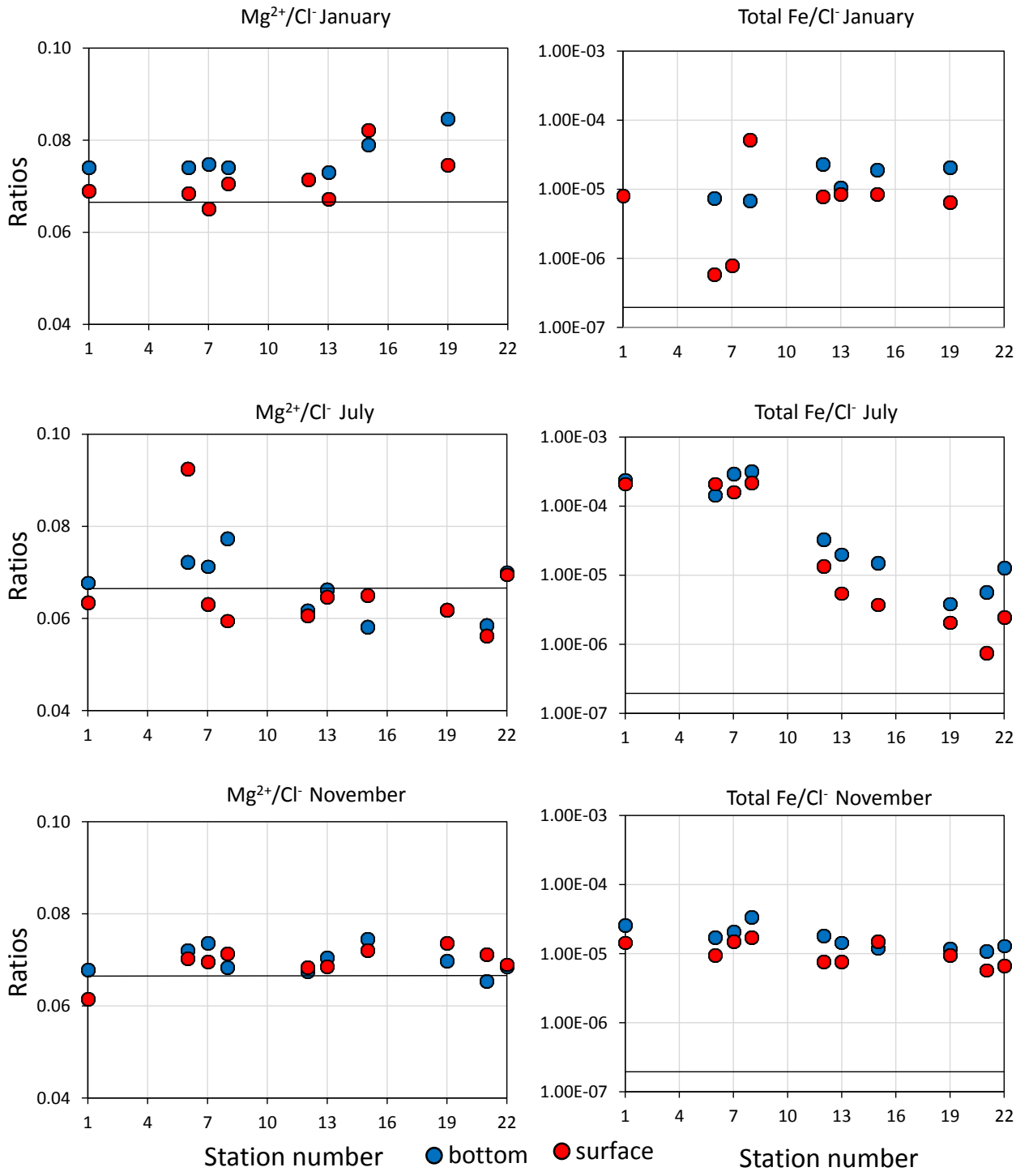

Figure 21: Mass ratios of magnesium to chlorinity (Mg^{2+}/Cl^{-}) and total iron to chlorinity (Fe/Cl^{-}) by station. The horizontal line represents the typical seawater ratios at 35 parts per million salinity.

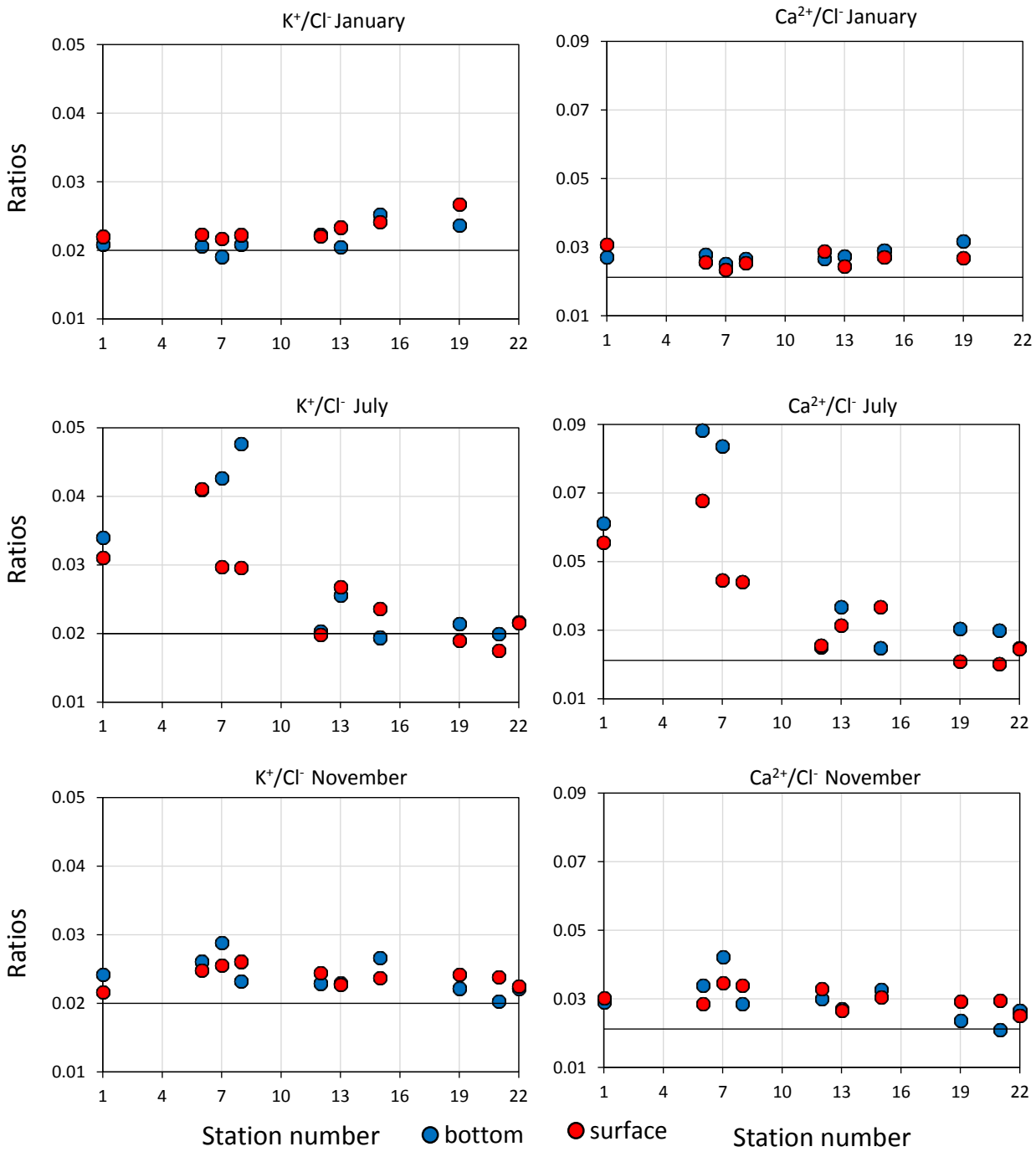

Figure 22: Mass ratios of potassium to chlorinity (K^+/Cl^-) and calcium to chlorinity (Ca^{2+}/Cl^-) by station. The horizontal line represents the typical seawater ratios at 35 parts per million salinity.

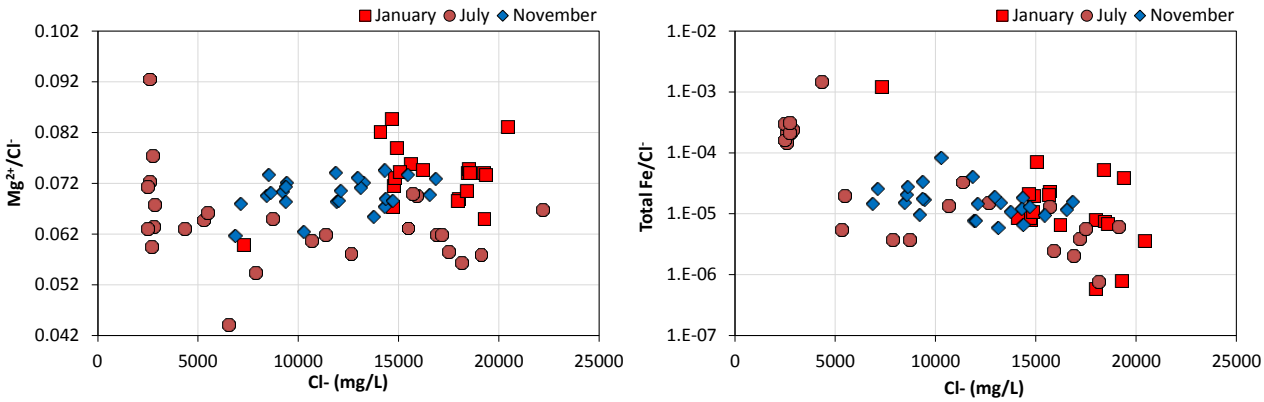

Figure 23: Relationships of mass ratios of magnesium to chlorinity (Mg^{2+}/Cl^{-}) and total iron to chlorinity (Fe/Cl^{-}) with chloride (Cl^{-}).

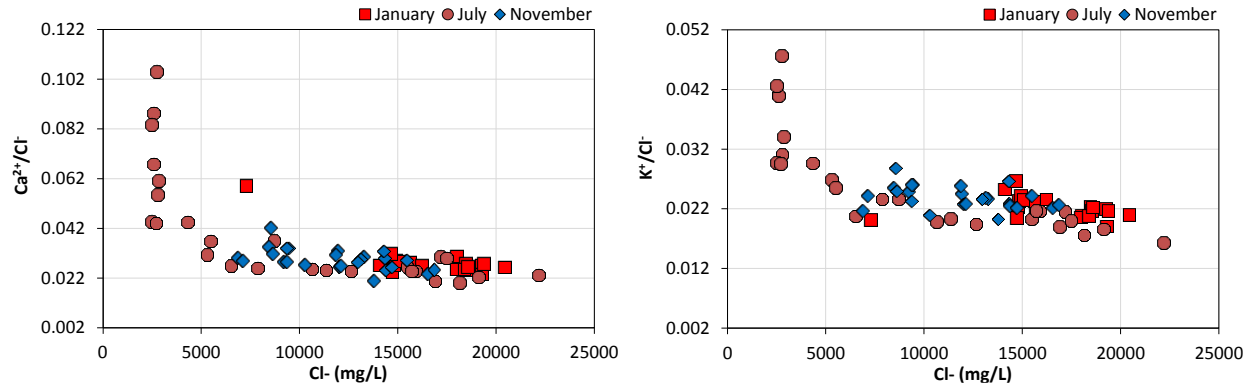

Figure 24: Relationships of mass ratios of potassium to chlorinity (K^{+}/Cl^{-}) and calcium to chlorinity (Ca^{2+}/Cl^{-}) with chloride (Cl^{-}).

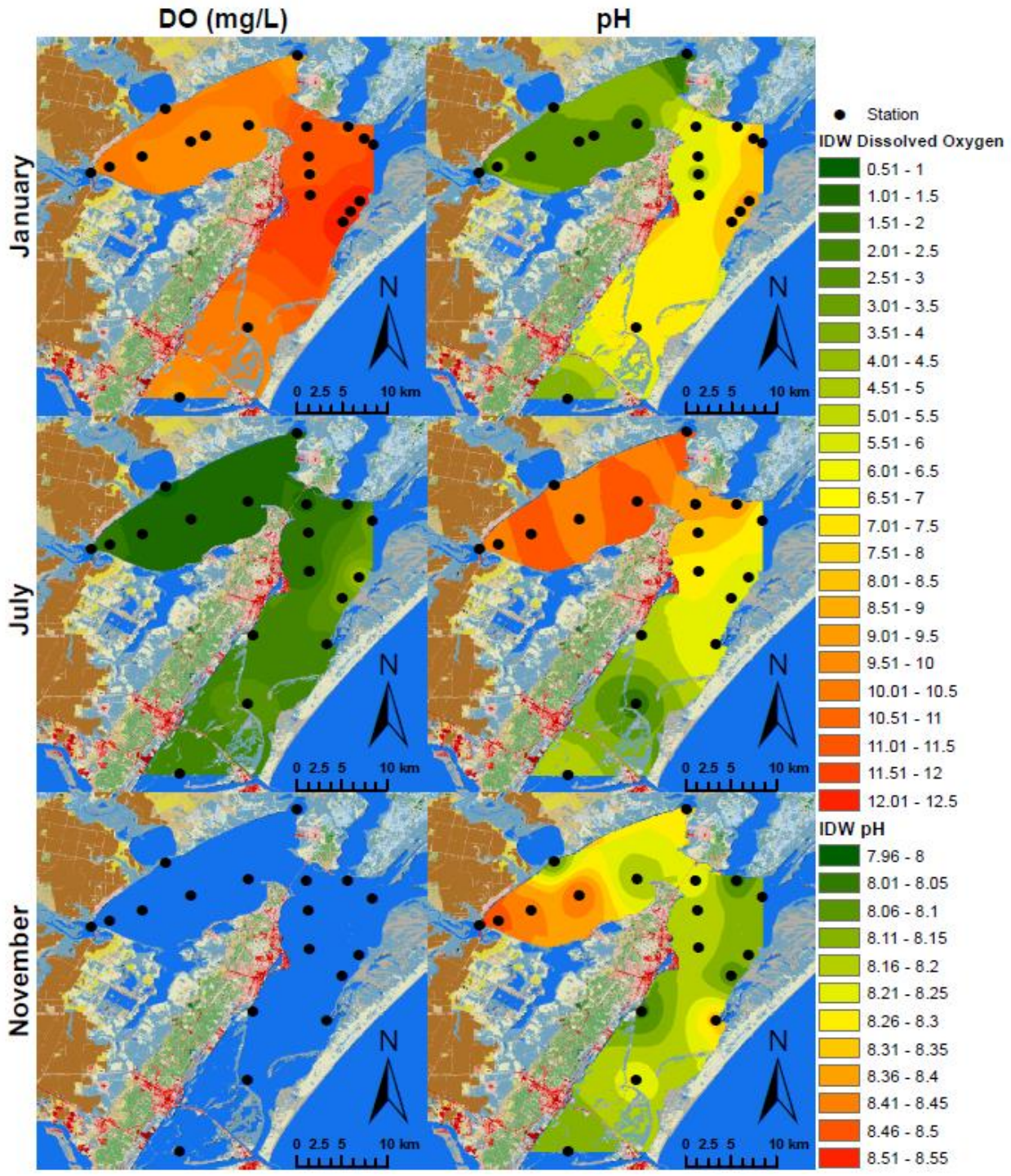

Figure 25: Spatial distribution using Inverse Distance Weighted (IDW) interpolation of Dissolved Oxygen (mg/L) and pH for January, July, and November.

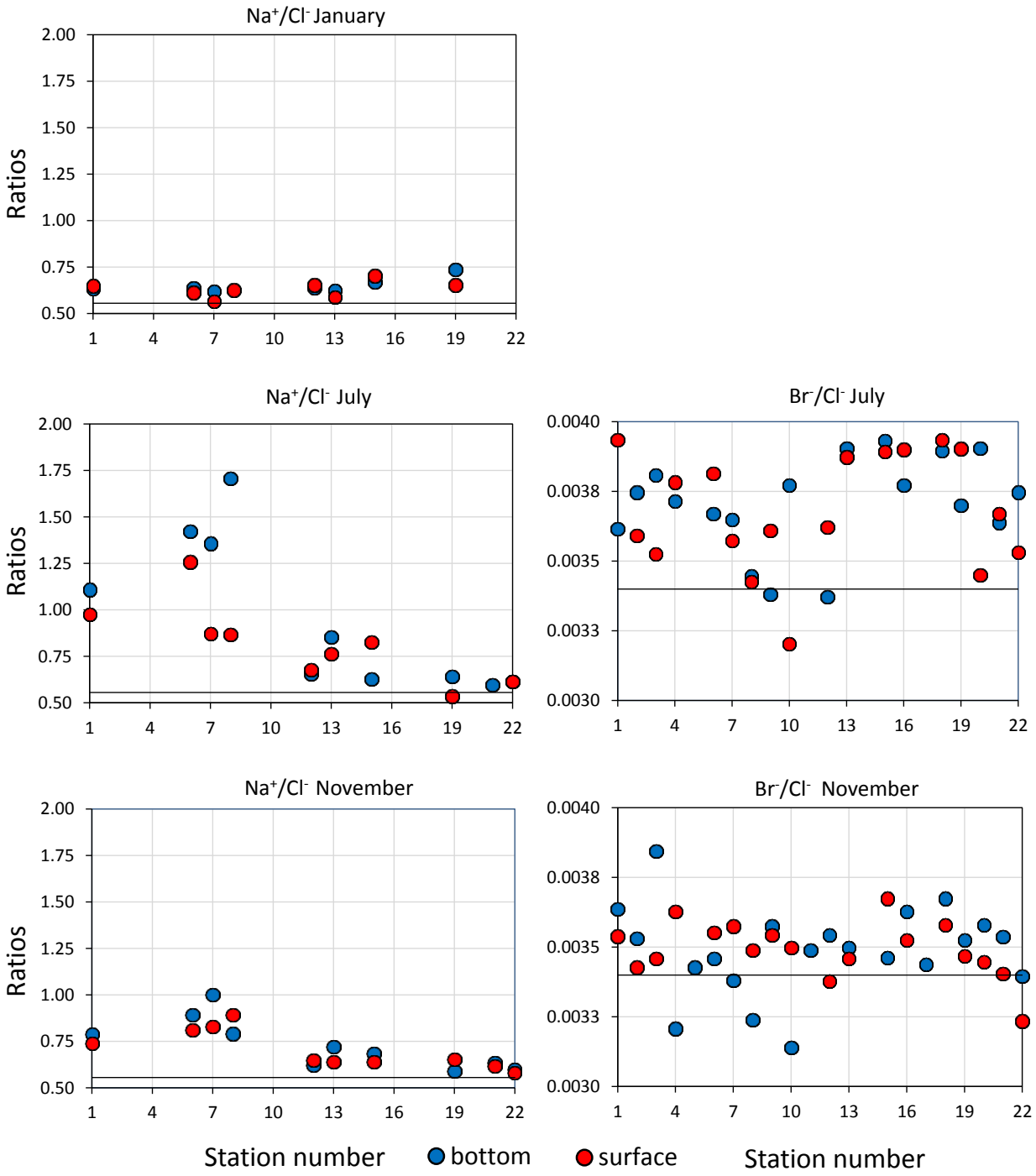

Figure 26: Mass ratios of sodium to chlorinity (Na^+/Cl^-) and bromide to chlorinity (Br^-/Cl^-) by station. The horizontal line represents the typical seawater ratios at 35 parts per million salinity.

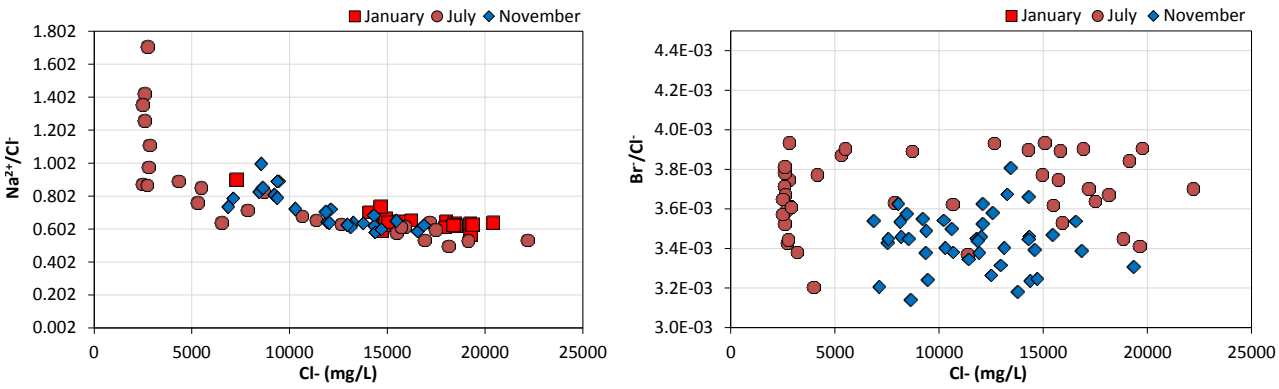

Figure 27: Relationships of mass ratios of sodium to chlorinity (Na^+/Cl^-) and bromide to chlorinity (Br^-/Cl^-) with chloride (Cl^-). No bromide data was available for January.

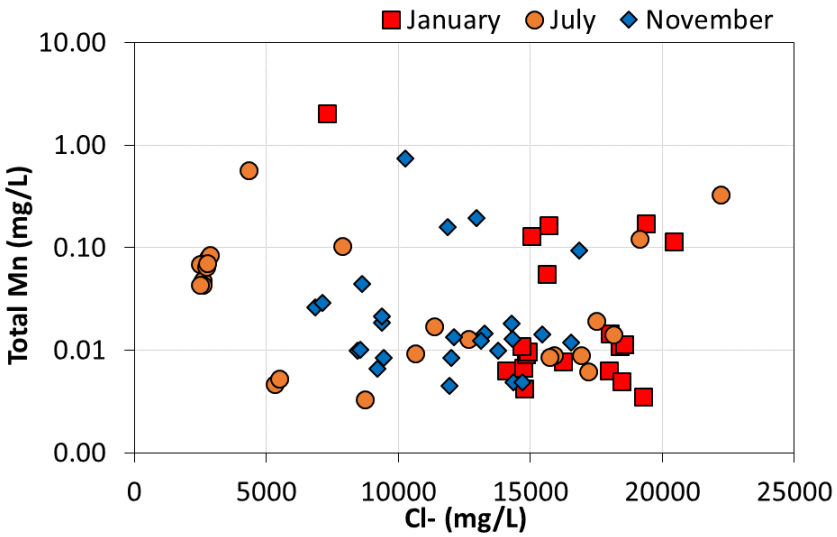

Figure 28: Cross-correlation between manganese (mg/L) and chloride (mg/L) for January, July, and November 2015.

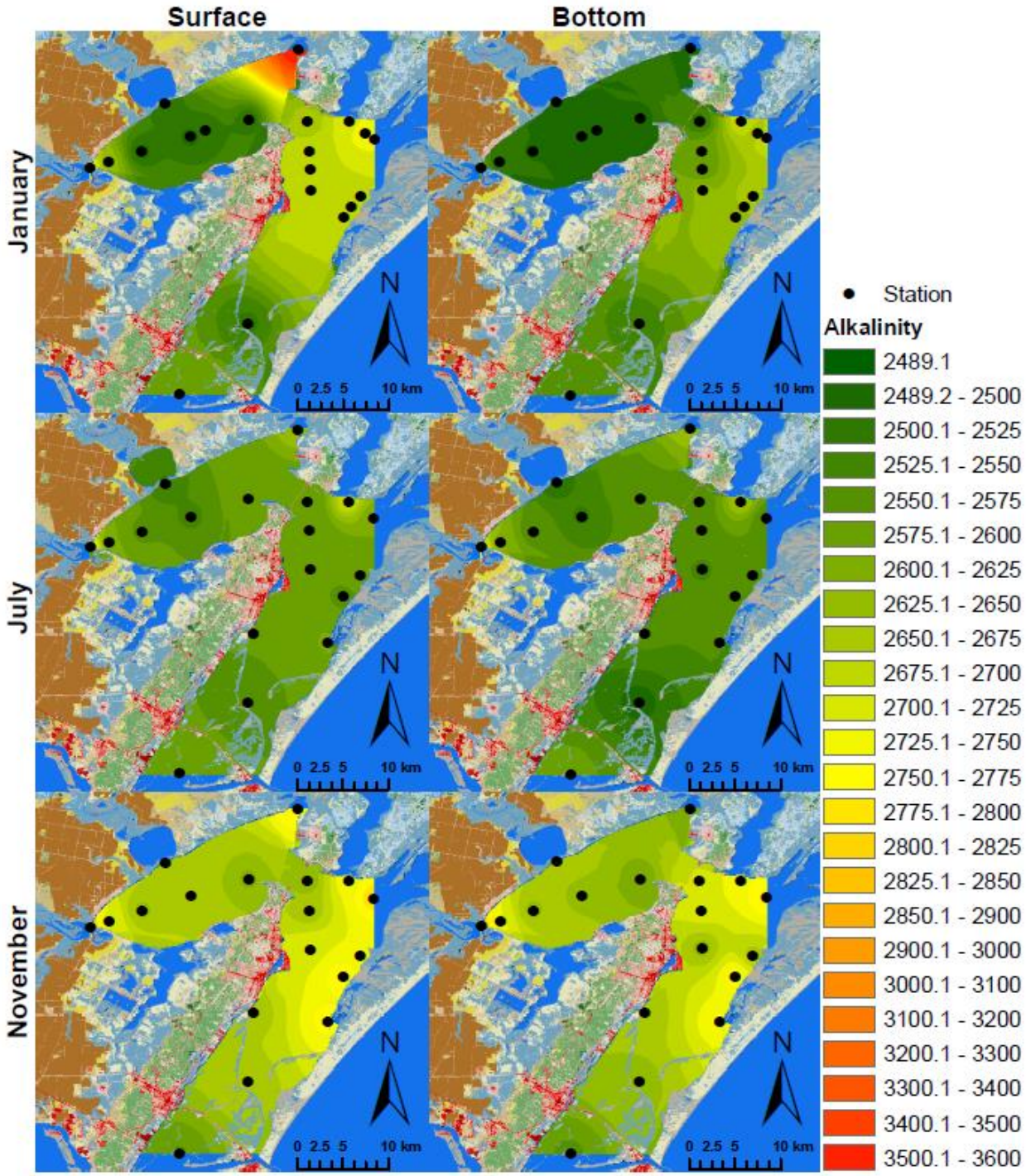

Figure 29: Spatial distribution using Inverse Distance Weighted (IDW) interpolation of Total Alkalinity (TA, µmol/L as HCO_3^-) for January, July, and November. Surface = 0.2m below the air-water interface. Bottom = 0.2m above the sediment-water interface.

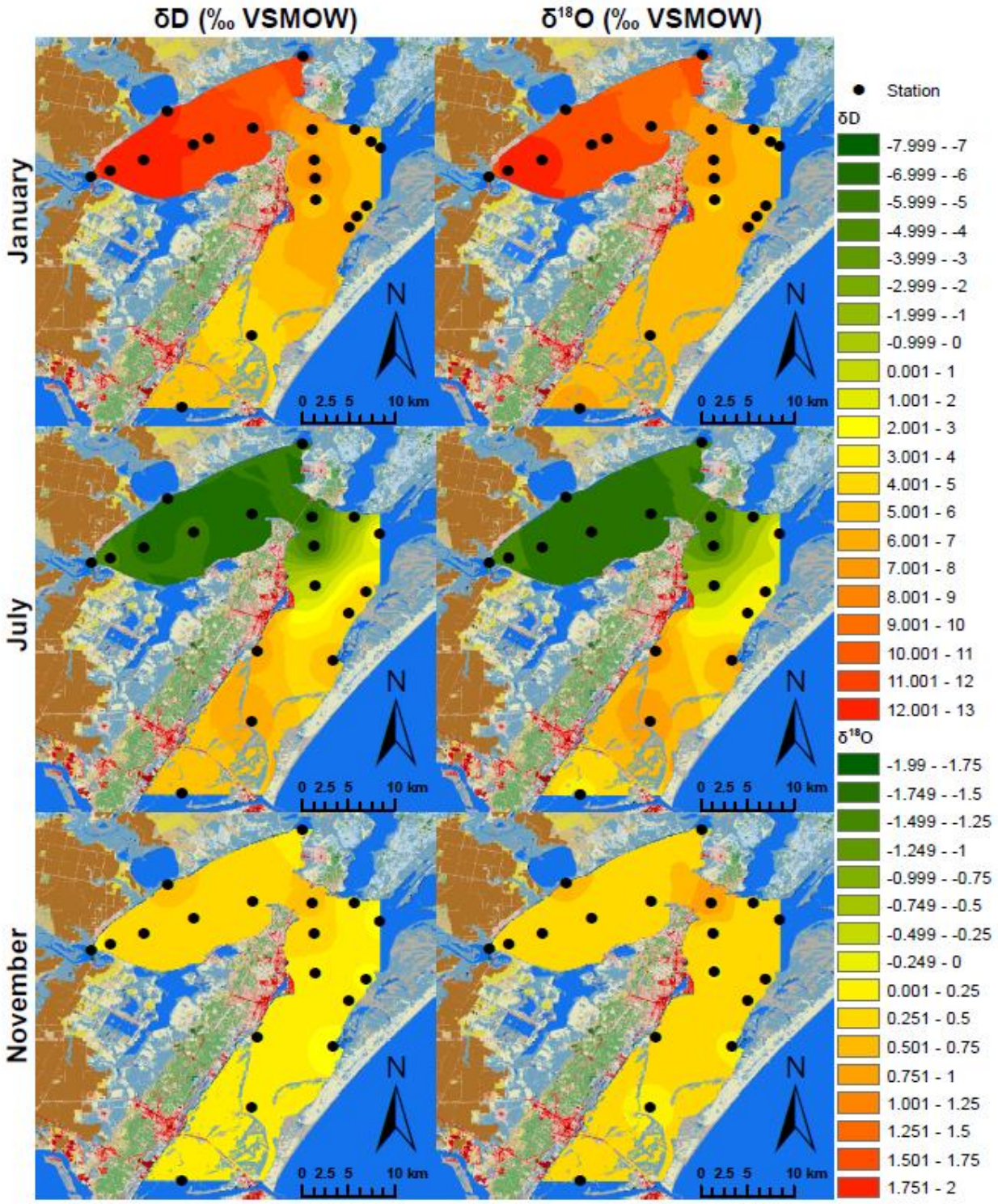

Figure 30: Spatial distribution using Inverse Distance Weighted (IDW) interpolation of δD (‰ VSMOW) and $\delta^{18}O$ (‰ VSMOW) for January, July, and November.

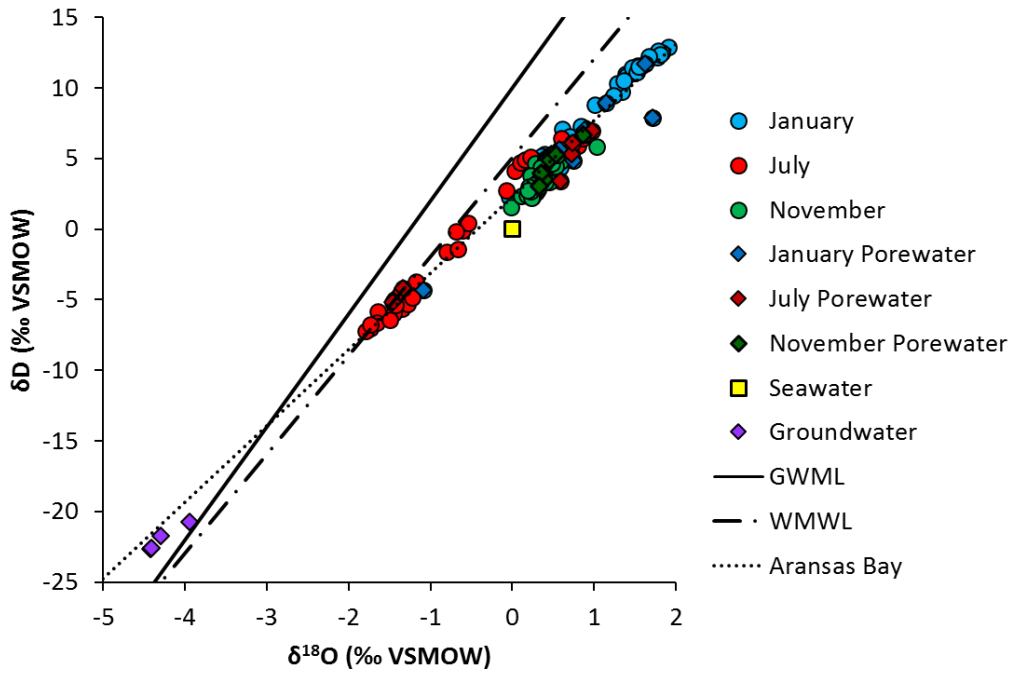

Figure 31: Cross-correlation between δD (‰ V-SMOW) and $\delta^{18}O$ (‰ V-SMOW) for the study period. GMWL = Global Meteoric Water Line (Craig et al. 1963). WMWL = Waco Meteoric Water Line.

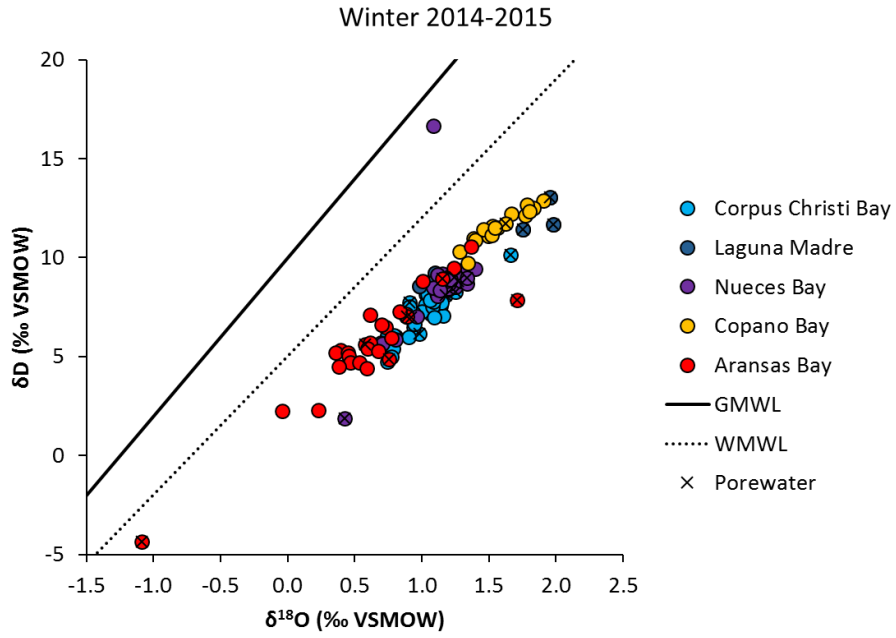

Figure 32: Cross-correlation of δD (‰ V-SMOW) and $\delta^{18}O$ (‰ V-SMOW) showing the comparison of primary and secondary bays in the Nueces River and Mission-Aransas Estuaries. GMWL = Global Meteoric Water Line (Craig et al. 1963). WMWL = Waco Meteoric Water Line.

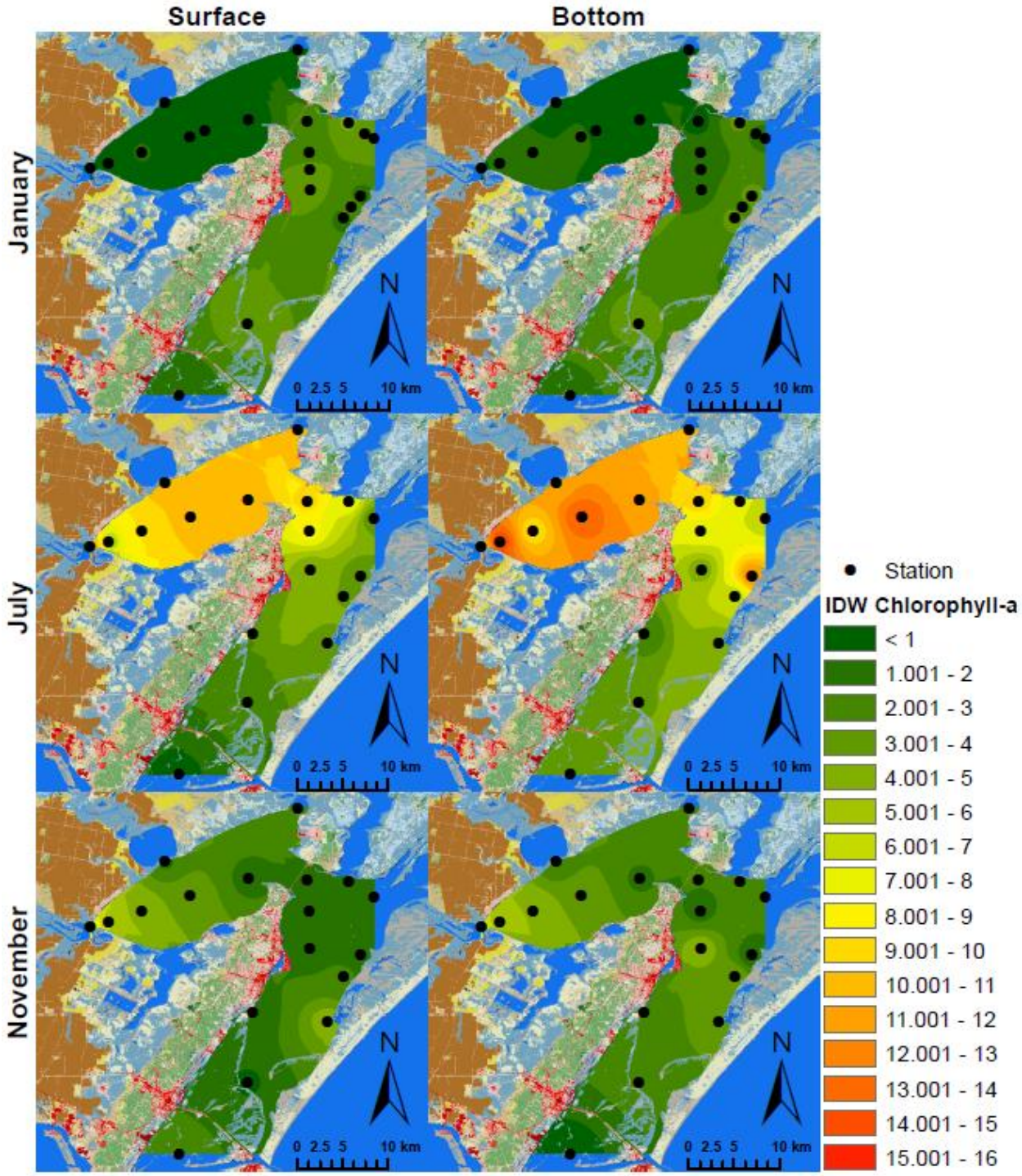

Figure 33: Spatial distribution using Inverse Distance Weighted (IDW) interpolation of Chlorophyll-a (µg/L) for January, July, and November. Surface = 0.2m below the air-water interface. Bottom = 0.2m above the sediment-water interface.

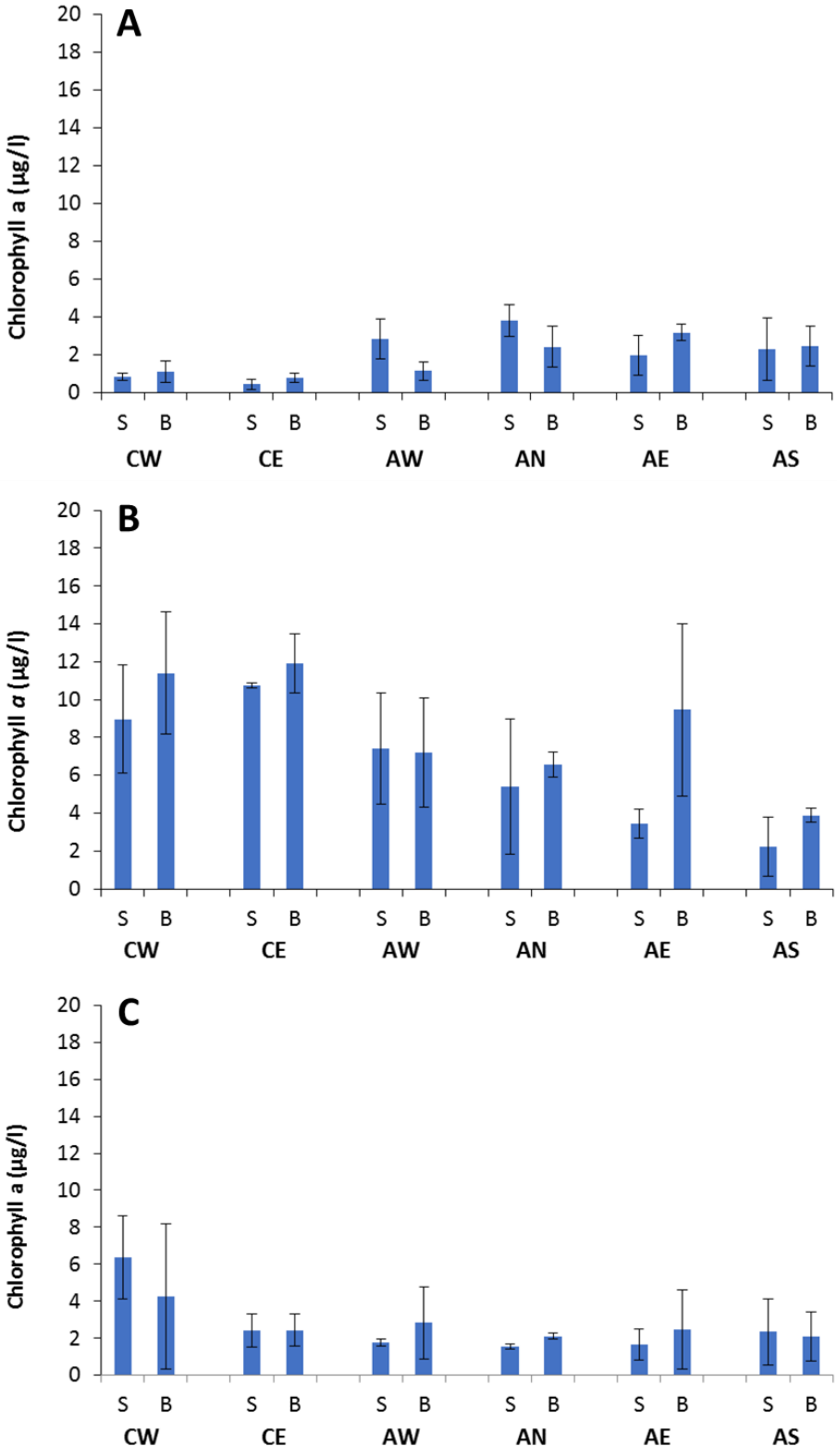

Figure 34: Chlorophyll-a concentration (µg/L) in surface ("S") and near bottom ("B") waters of Copano Bay and Aransas Bay in January 2015 (A), July 2015 (B), and November 2015 (C).

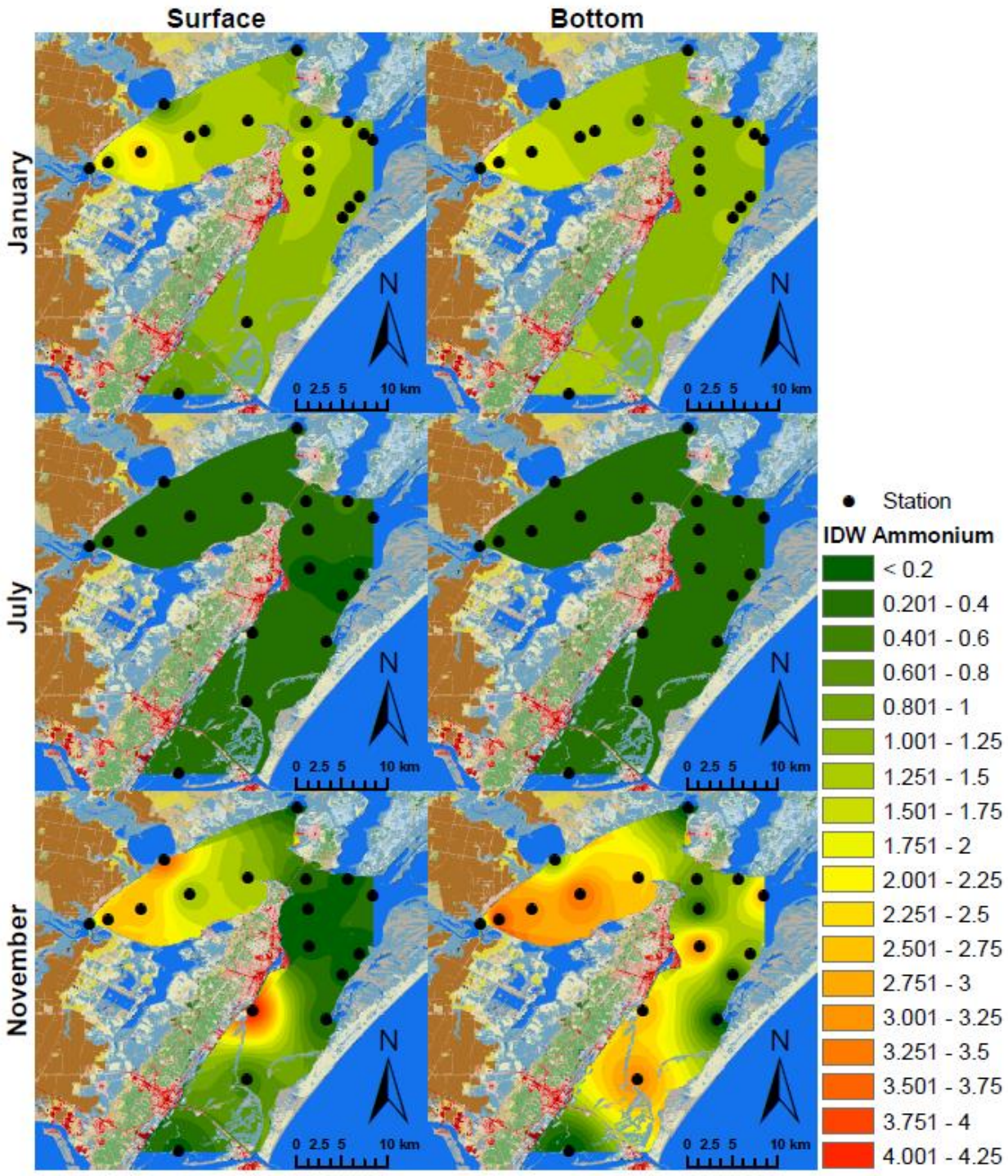

Figure 35: Spatial distribution using Inverse Distance Weighted (IDW) interpolation of Ammonium (NH_4, µmol/L) for January, July, and November. Surface = 0.2m below the air-water interface. Bottom = 0.2m above the sediment-water interface.

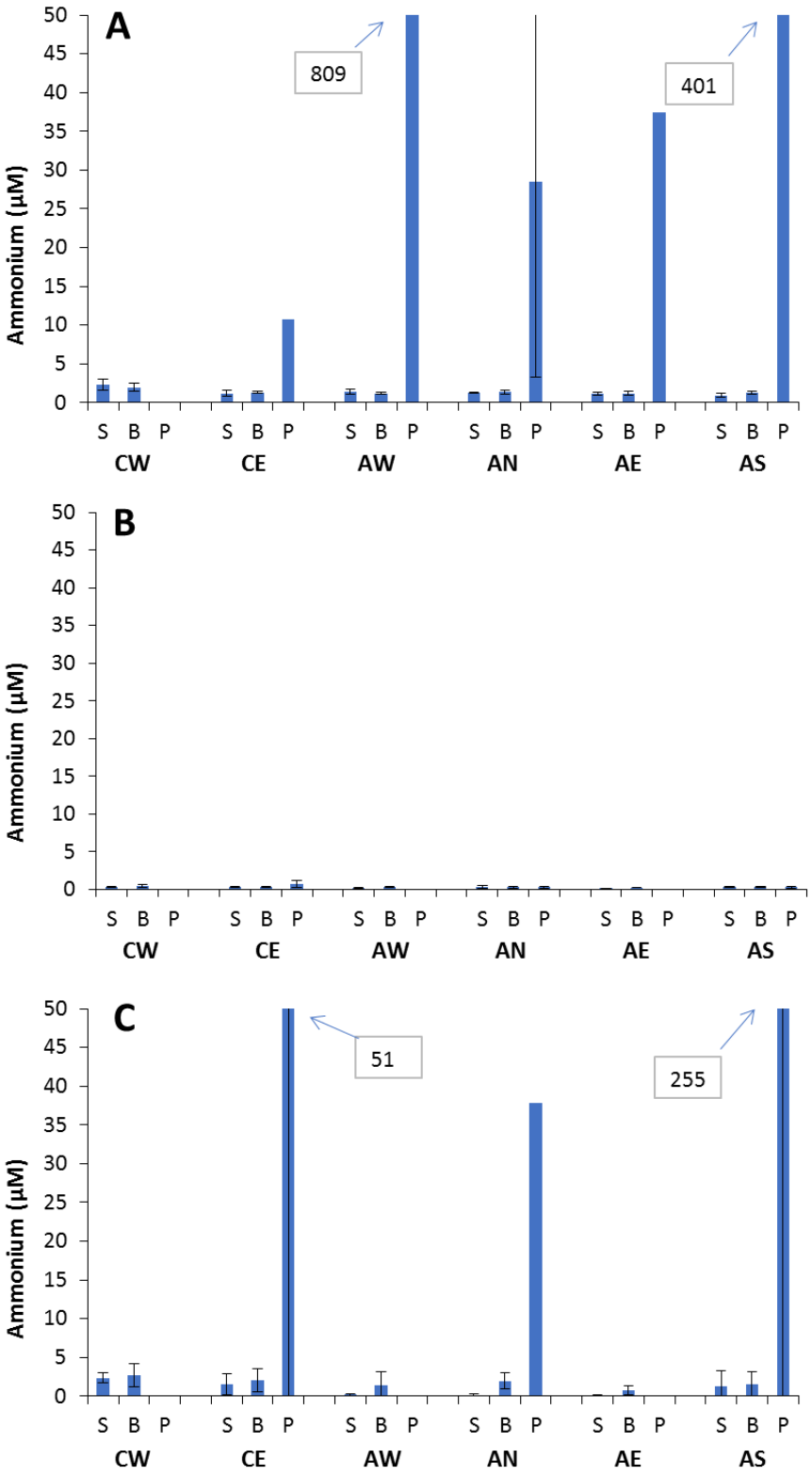

Figure 36: Ammonium concentrations (µM) in surface ("S"), near bottom ("B"), and porewater ("P") of Copano Bay and Aransas Bay in January 2015 (A), July 2015 (B), and November 2015 (C).

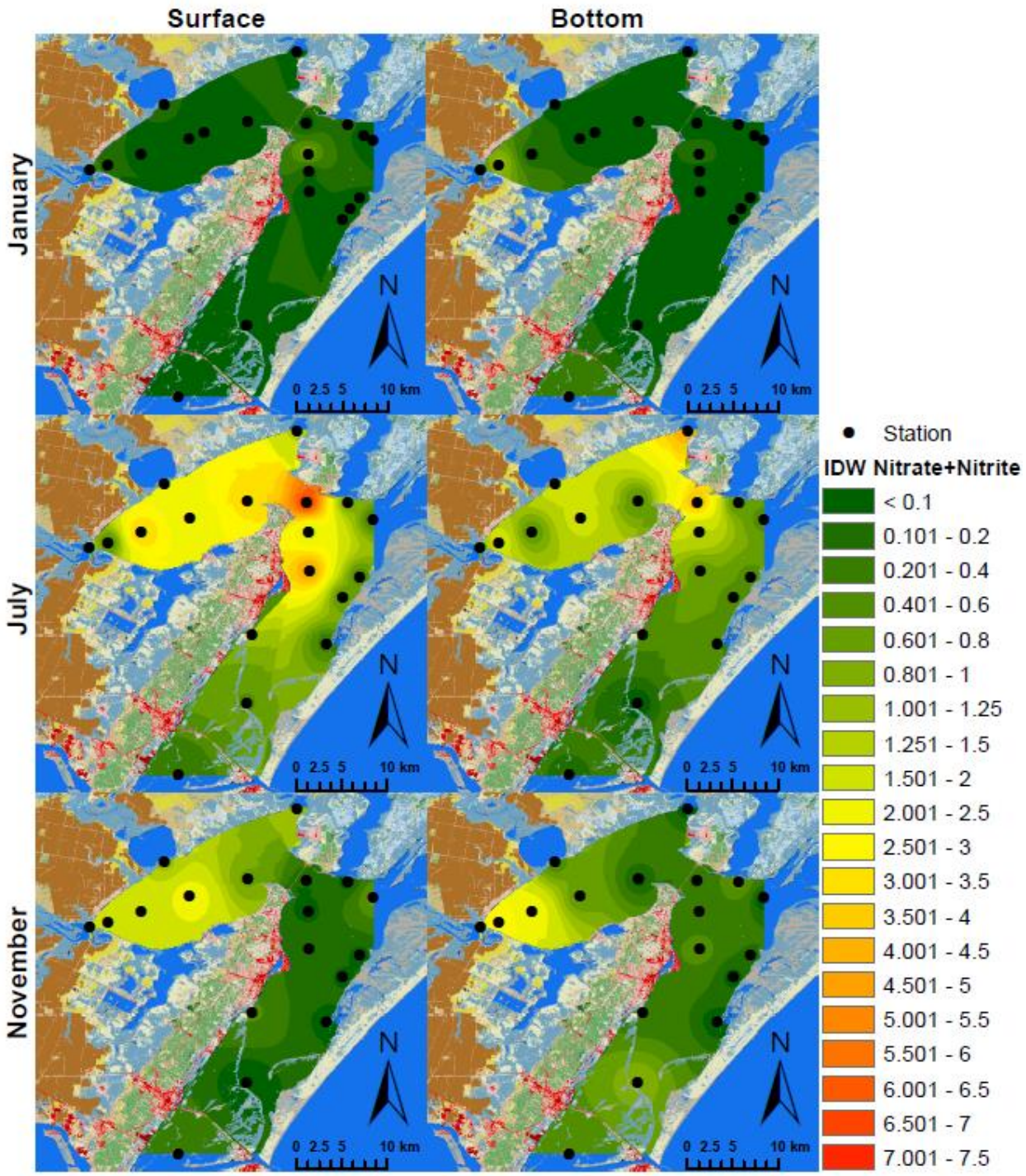

Figure 37: Spatial distribution using Inverse Distance Weighted (IDW) interpolation of Nitrate+Nitrite (N+N, µmol/L) for January, July, and November. Surface = 0.2m below the air-water interface. Bottom = 0.2m above the sediment-water interface.

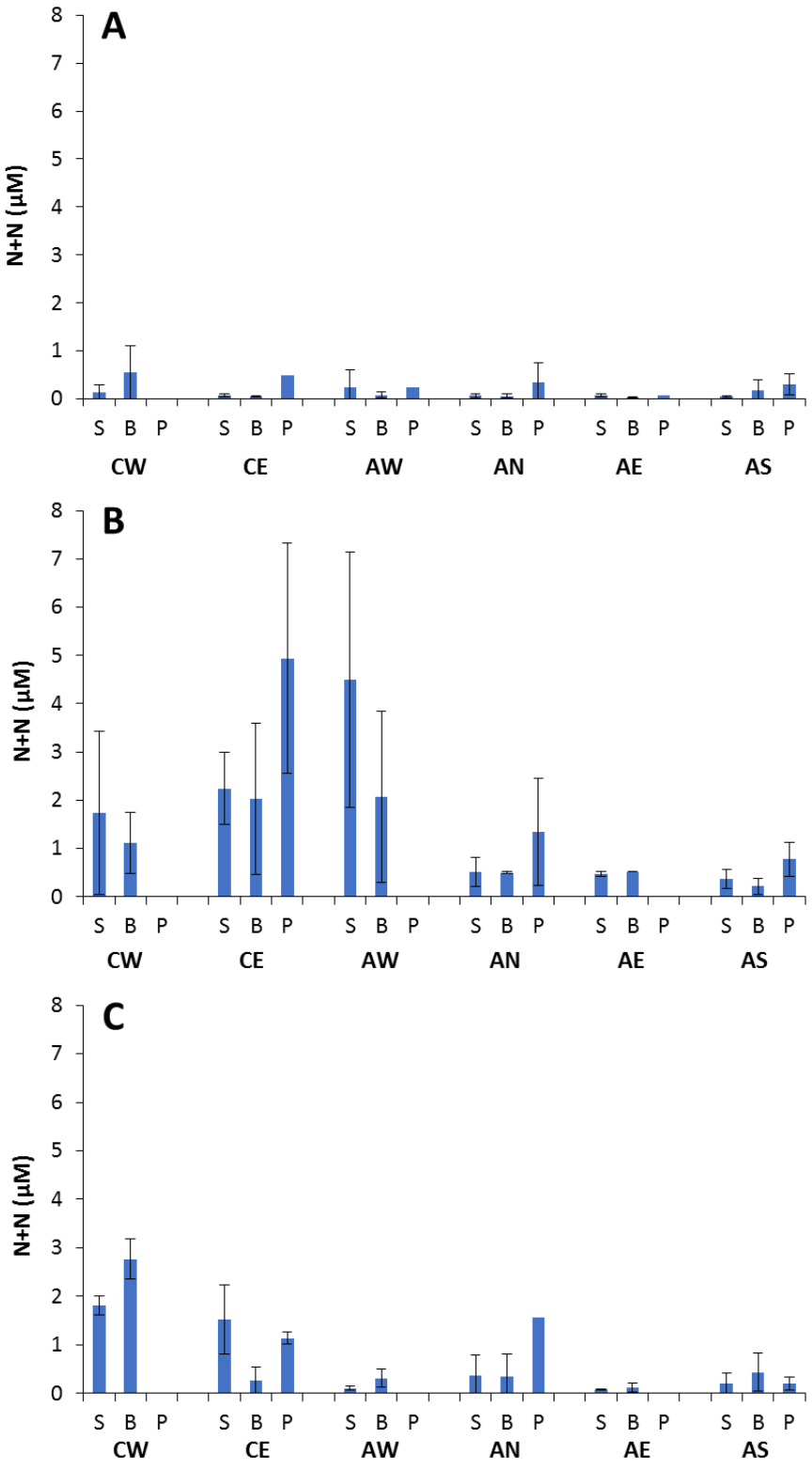

Figure 38: Nitrate + nitrite concentrations (µM) in surface ("S"), near bottom ("B"), and porewater ("P") of Copano Bay and Aransas Bay in January 2015 (A), July 2015 (B), and November 2015 (C).

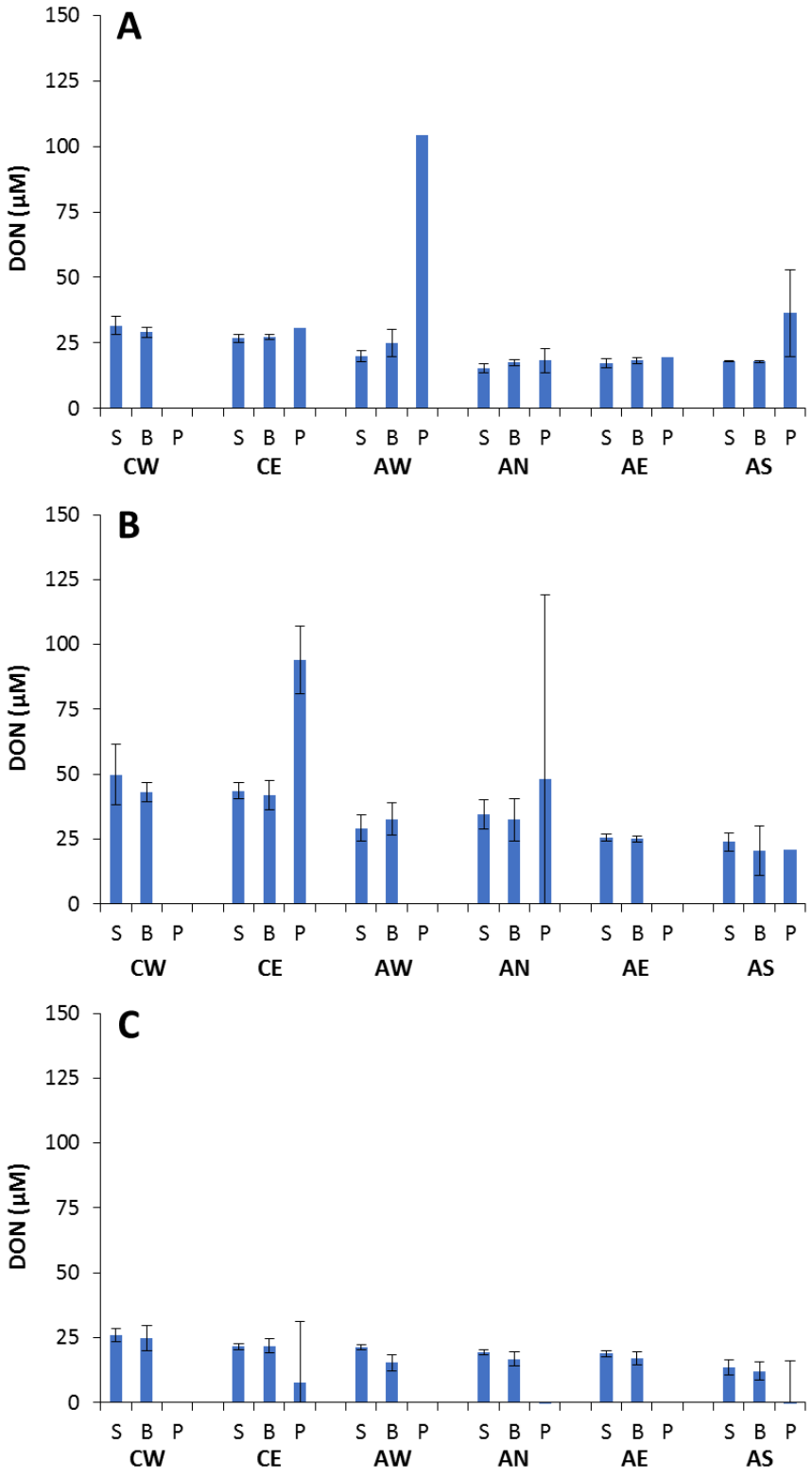

Figure 39: Dissolved organic nitrogen concentrations (µM) in surface ("S"), near bottom ("B"), and porewater ("P") of Copano Bay and Aransas Bay in January 2015 (A), July 2015 (B), and November 2015 (C).

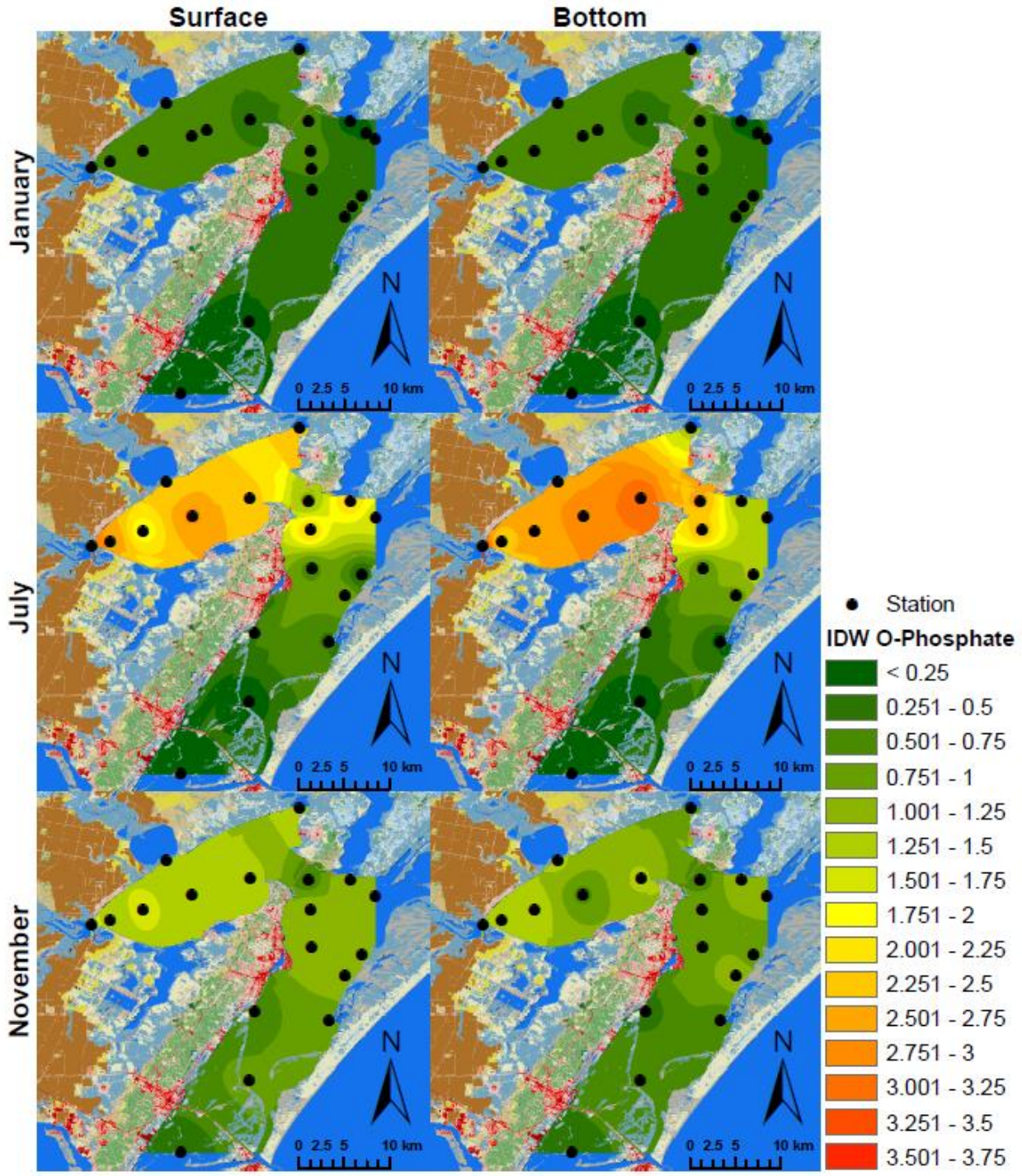

Figure 40: Spatial distribution using Inverse Distance Weighted (IDW) interpolation of O-Phosphate (PO_4, µmol/L) for January, July, and November. Surface = 0.2m below the air-water interface. Bottom = 0.2m above the sediment-water interface.

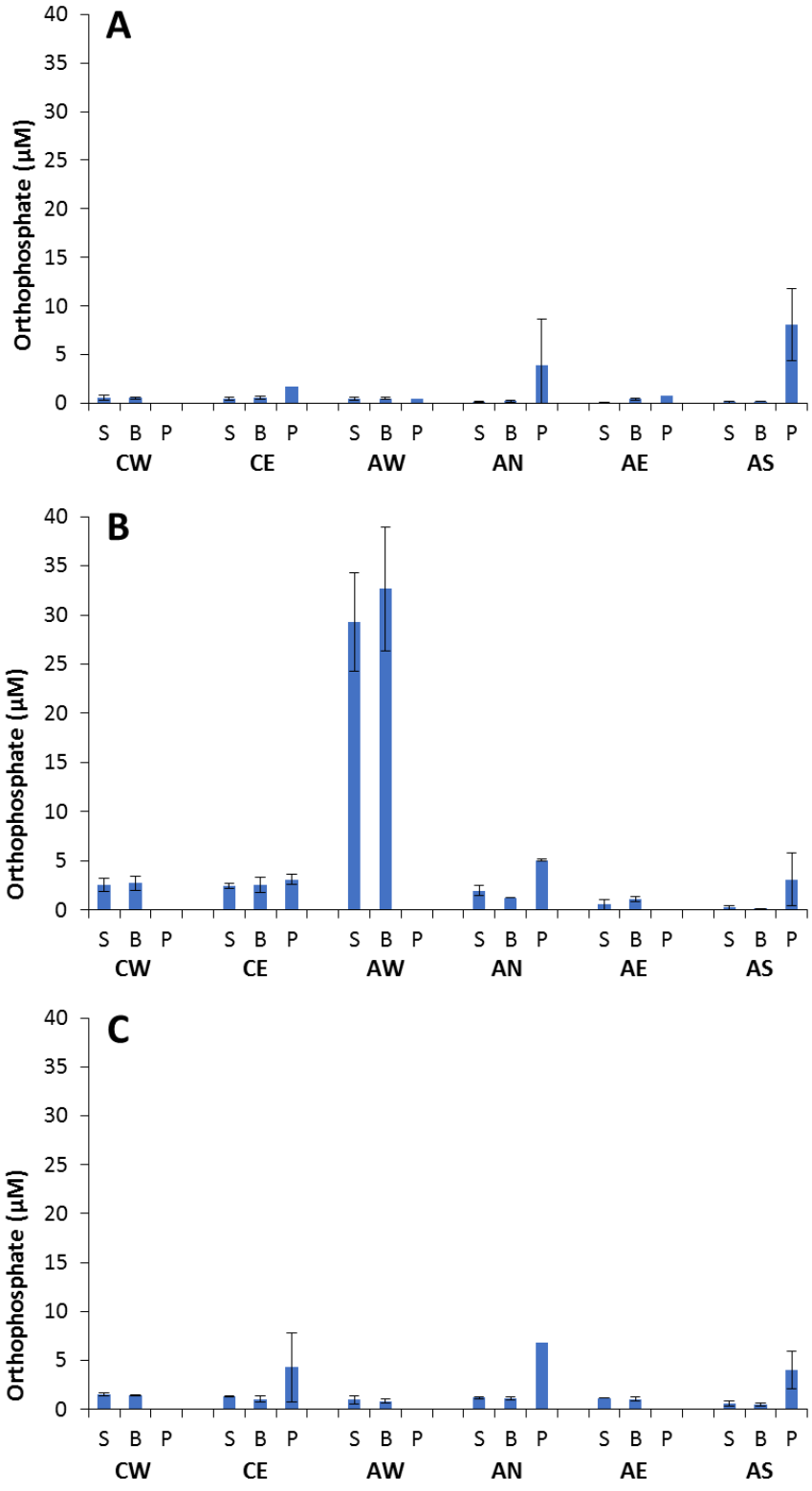

Figure 41: Orthophosphate concentrations (µM) in surface ("S"), near bottom ("B"), and porewater ("P") of Copano Bay and Aransas Bay in January 2015 (A), July 2015 (B), and November 2015 (C).

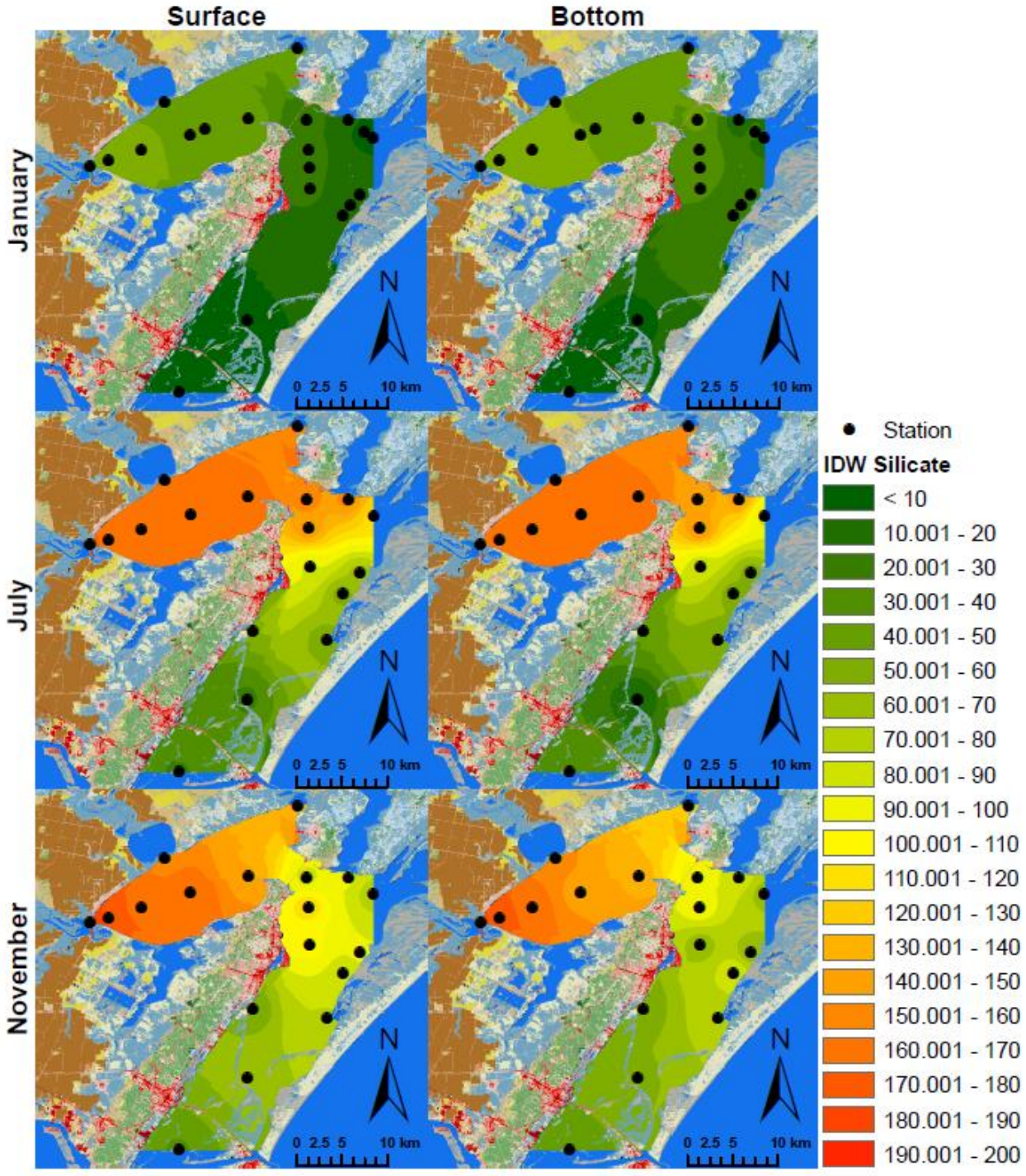

Figure 42: Spatial distribution using Inverse Distance Weighted (IDW) interpolation of Silicate (SiO_4, µmol/L) for January, July, and November. Surface = 0.2m below the air-water interface. Bottom = 0.2m above the sediment-water interface.

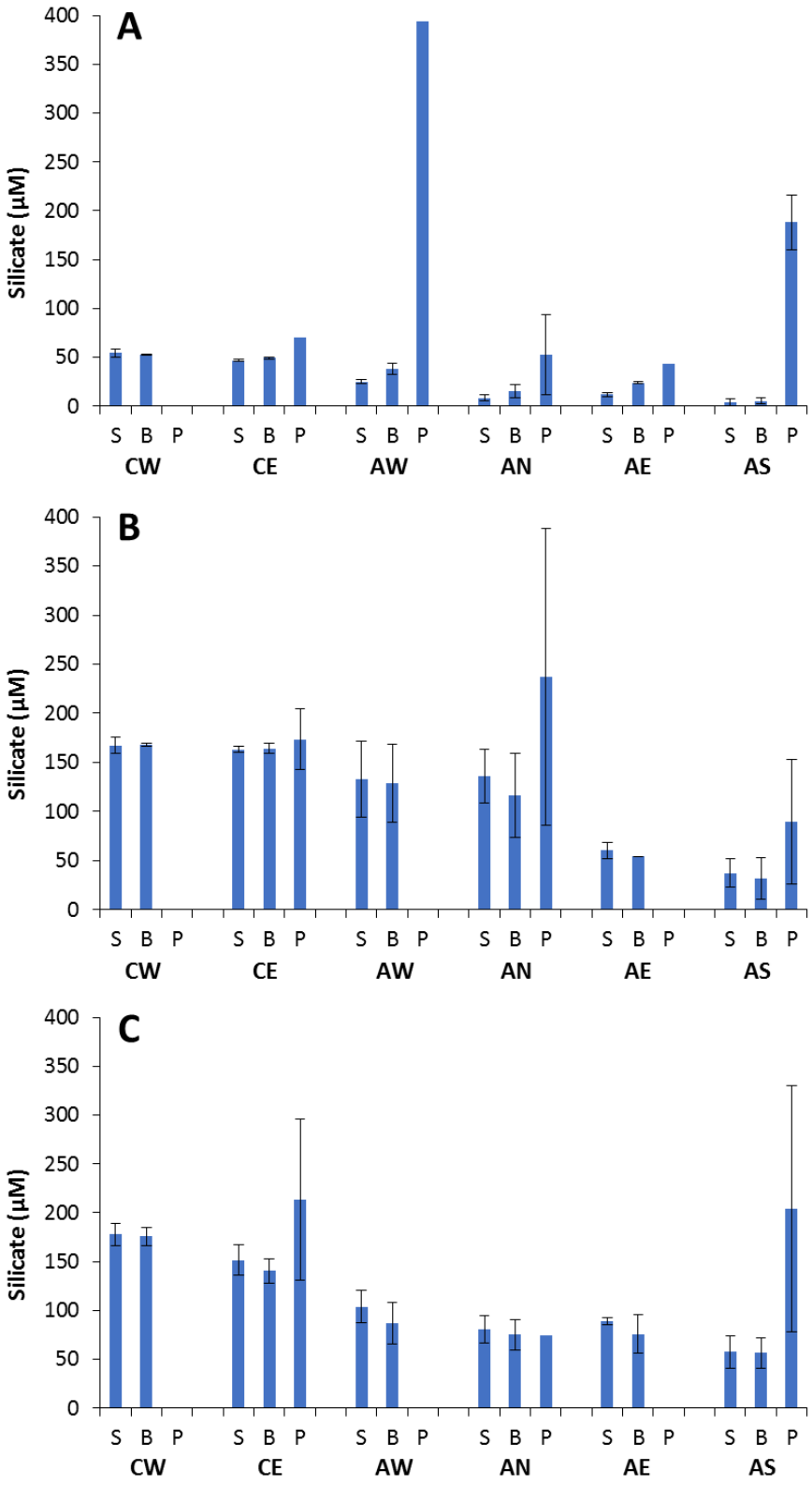

Figure 43: Silicate concentrations (µM) in surface ("S"), near bottom ("B"), and porewater ("P") of Copano Bay and Aransas Bay in January 2015 (A), July 2015 (B), and November 2015 (C).

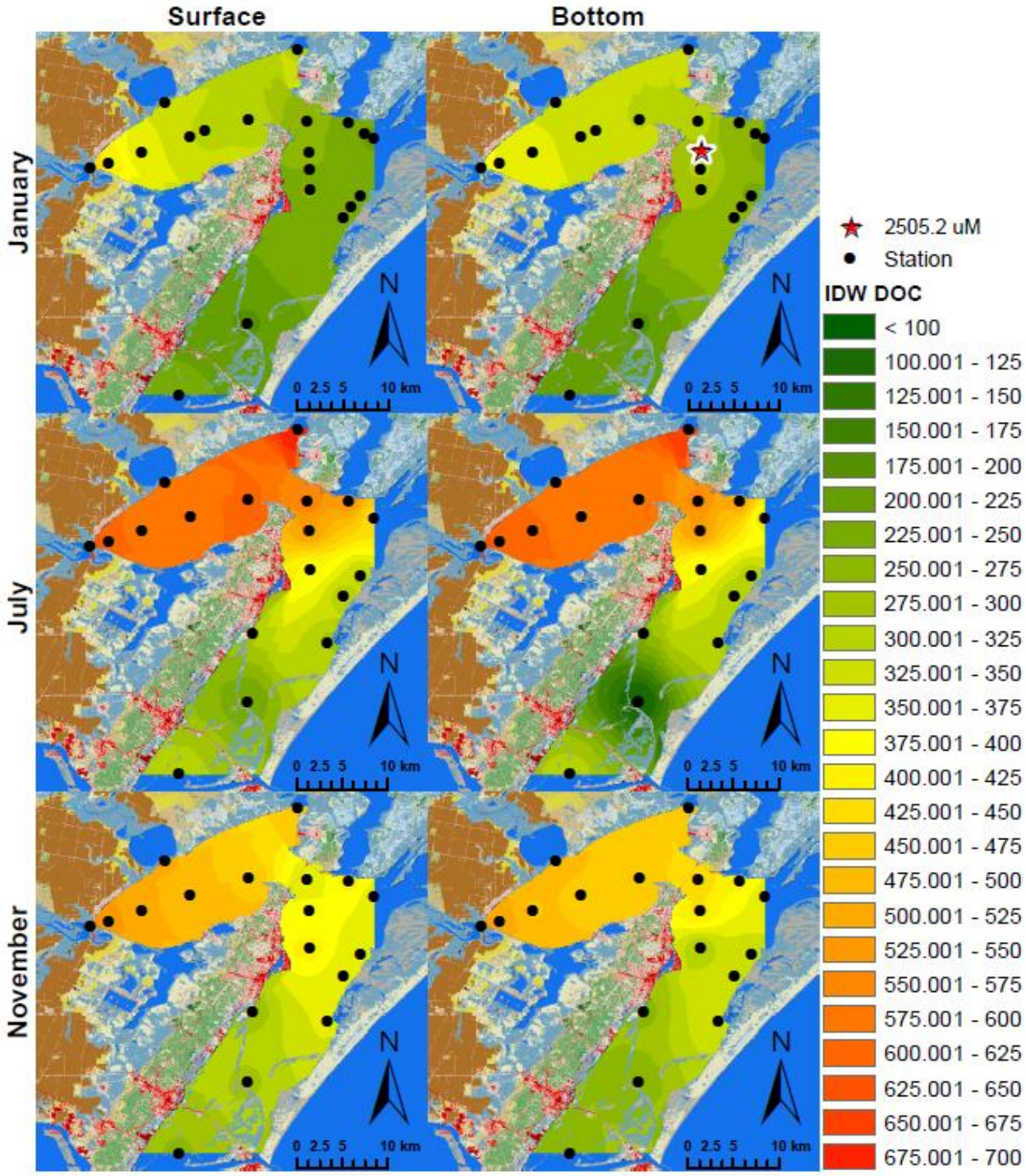

Figure 44: Spatial distribution using Inverse Distance Weighted (IDW) interpolation of Dissolved Inorganic Carbon (DOC, µmol/L) for January, July, and November. Surface = 0.2m below the air-water interface. Bottom = 0.2m above the sediment-water interface.

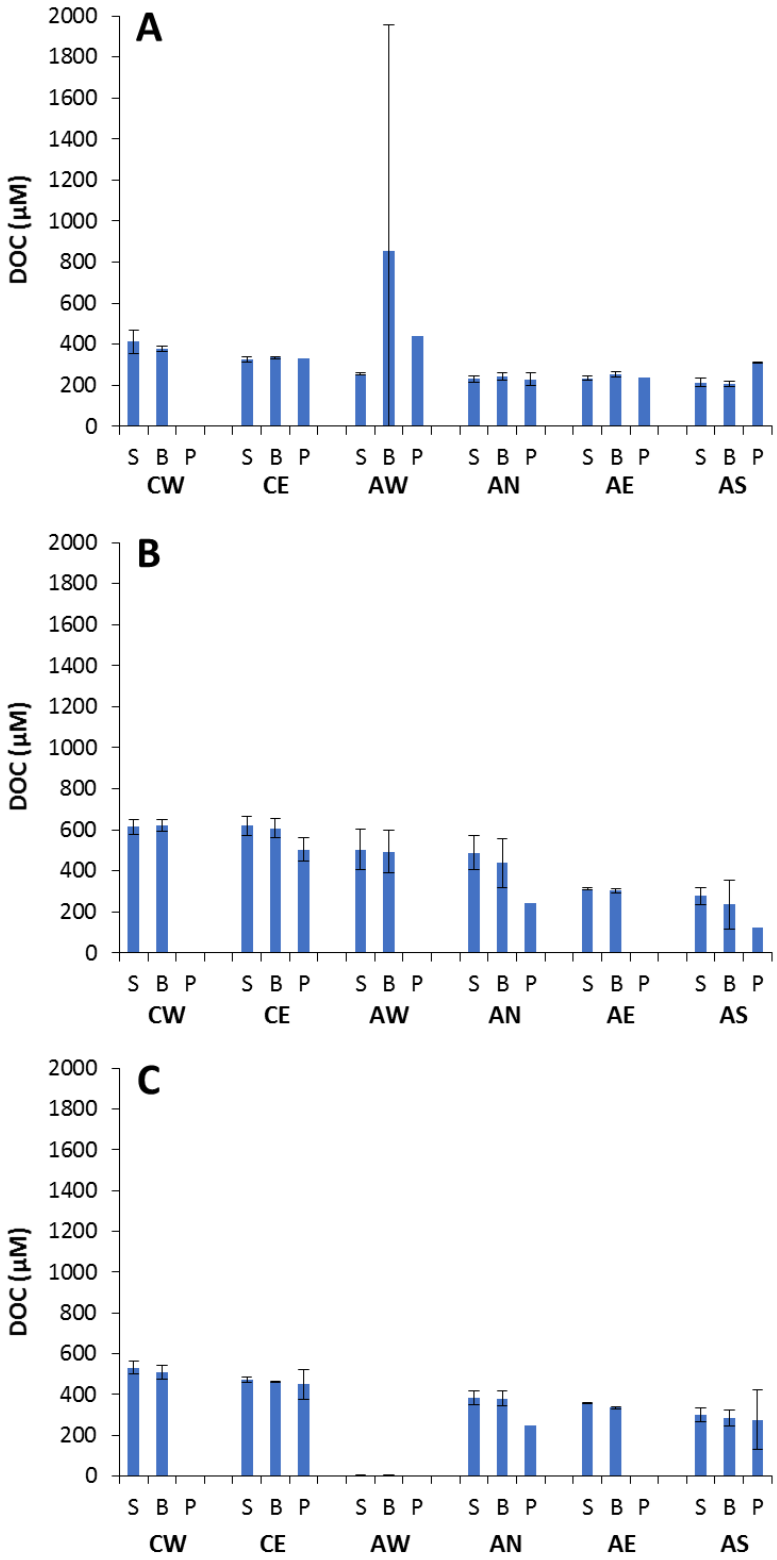

Figure 45: Dissolved organic carbon concentrations (µM) in surface ("S"), near bottom ("B"), and porewater ("P") of Copano Bay and Aransas Bay in January 2015 (A), July 2015 (B), and November 2015 (C).

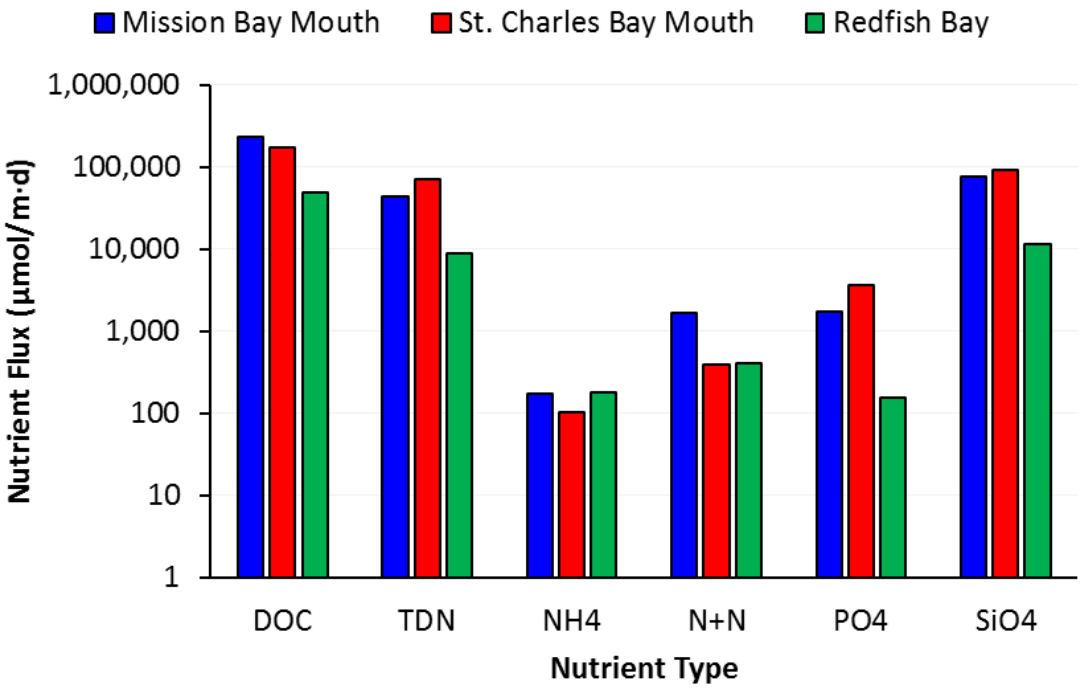

Figure 46: Groundwater nutrient fluxes (µmol/m·d) at Mission Bay Mouth (station 7), St. Charles Bay mouth (station 13), and Redfish Bay (station 19) for July 2015.

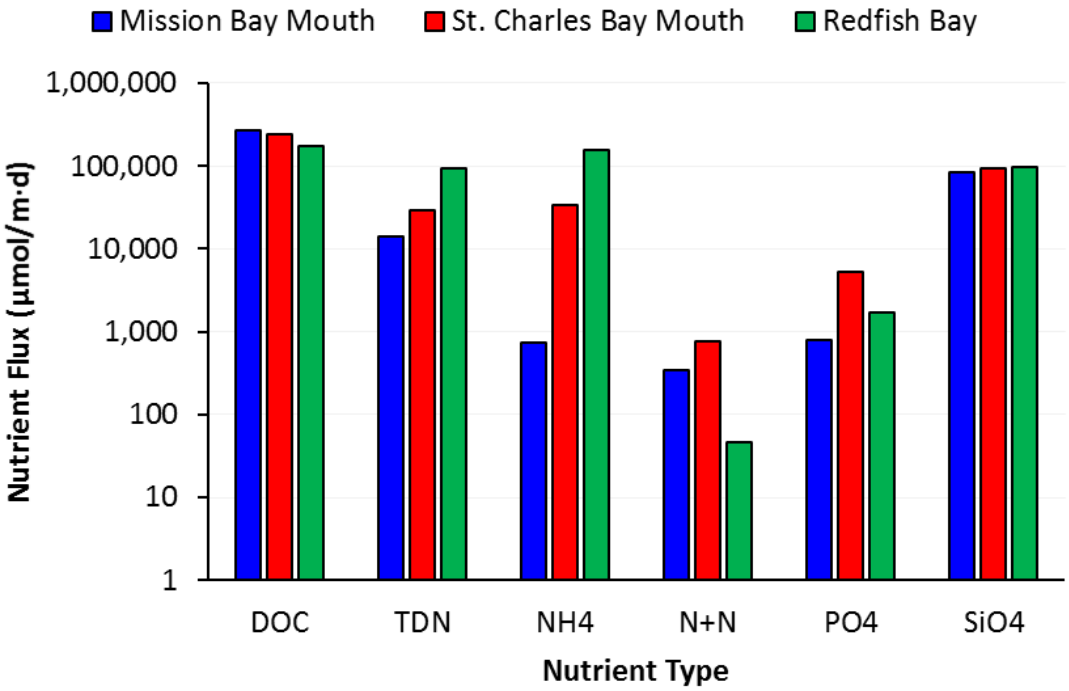

Figure 47: Groundwater nutrient fluxes (µmol/m·d) at Mission Bay Mouth (station 7), St. Charles Bay mouth (station 13), and Redfish Bay (station 19) for November 2015.

APPENDIX LEGEND

Appendix 1. Time-lapse electrical resistivity (ER) inversions for first and last monitoring time and the final percent change in resistivity images for groundwater monitoring stations: Oso Bay Inlet, Laguna Madre mouth, and Shamrock Island (see Figure 1 in the main report for locations).

Appendix 2. Summary of all geochemical and isotope data collected in January, July, and November, 2015.

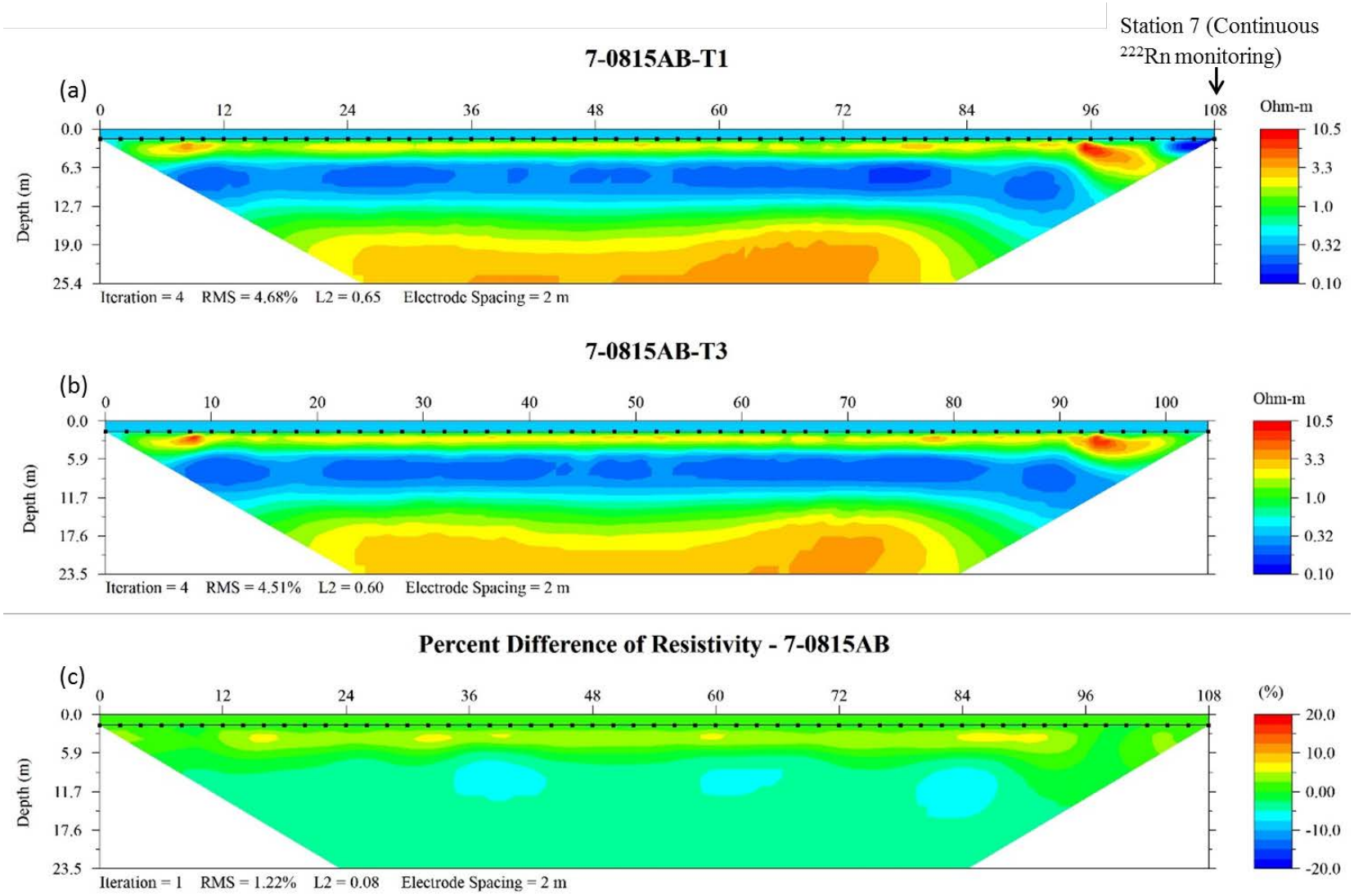

Figure TL 1: Summer time-lapse resistivity profiles (first (a) and last (b) time steps) for station 7 at Mission Mouth (see Figure 10 for geographic reference). The computed percent difference in resistivity (c) shows the change in porewater resistivity over a four-hour period.

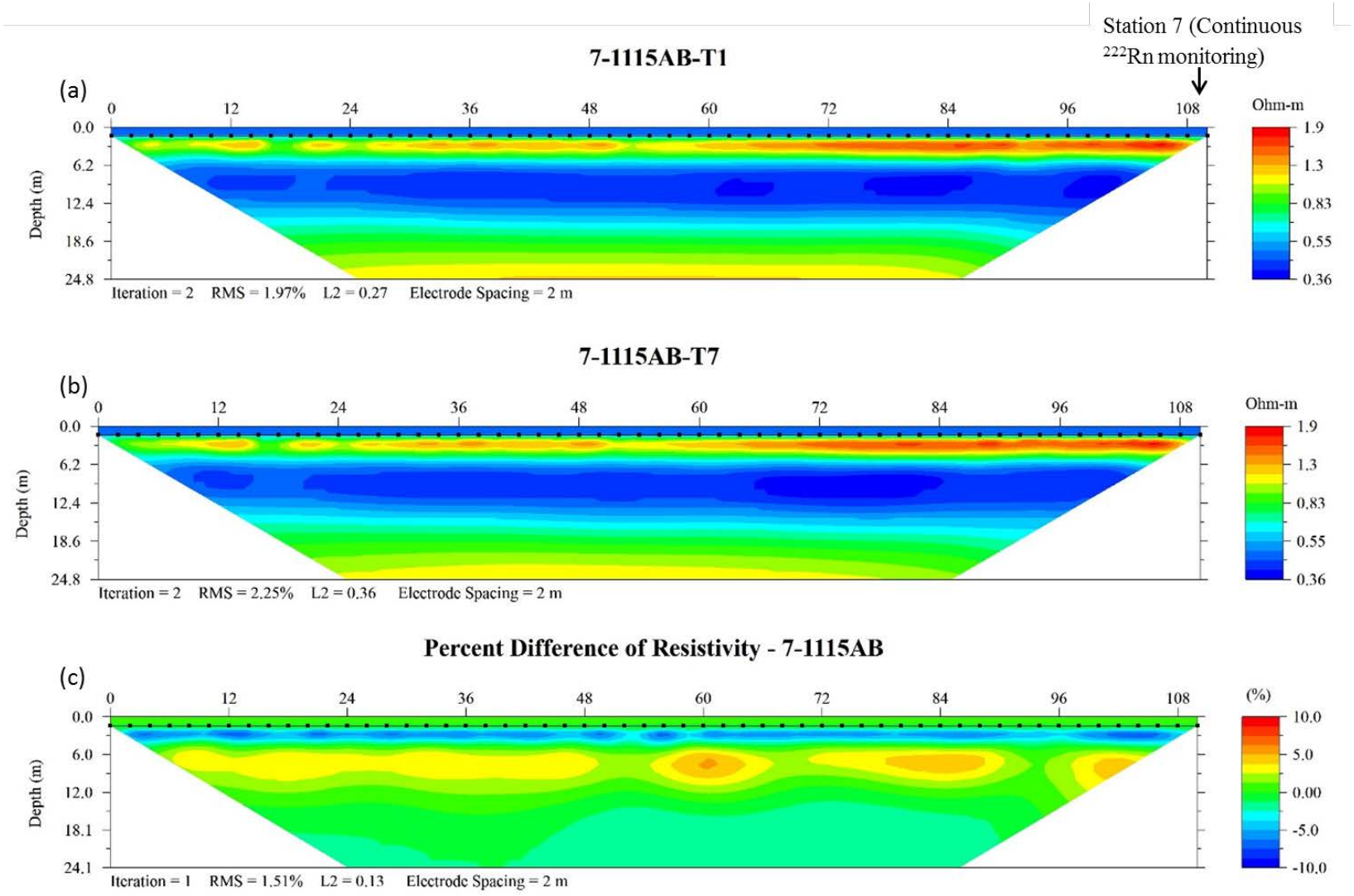

Figure TL 2: Fall time-lapse resistivity profiles (first (a) and last (b) time steps) for station 7 Mission Mouth (see Figure 11 for geographic reference). The computed percent difference in resistivity (c) shows the change in porewater resistivity over an eight-hour period.

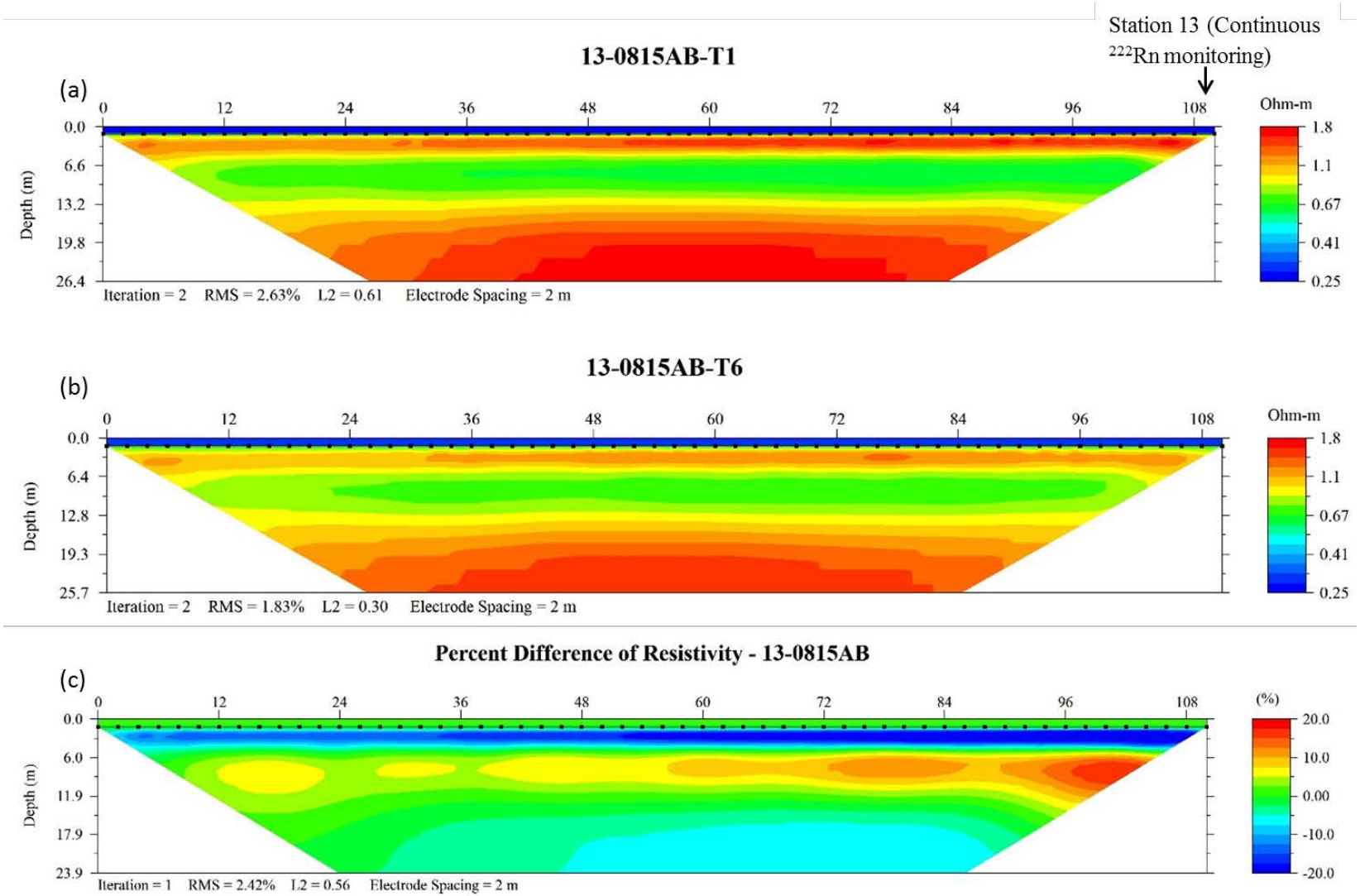

Figure TL 3: Summer time-lapse resistivity profiles (first (a) and last (b) time steps) for station 13 at St. Charles Mouth (see Figure 10 for geographic reference). The computed percent difference in resistivity (c) shows the change in porewater resistivity over a seven-hour period.

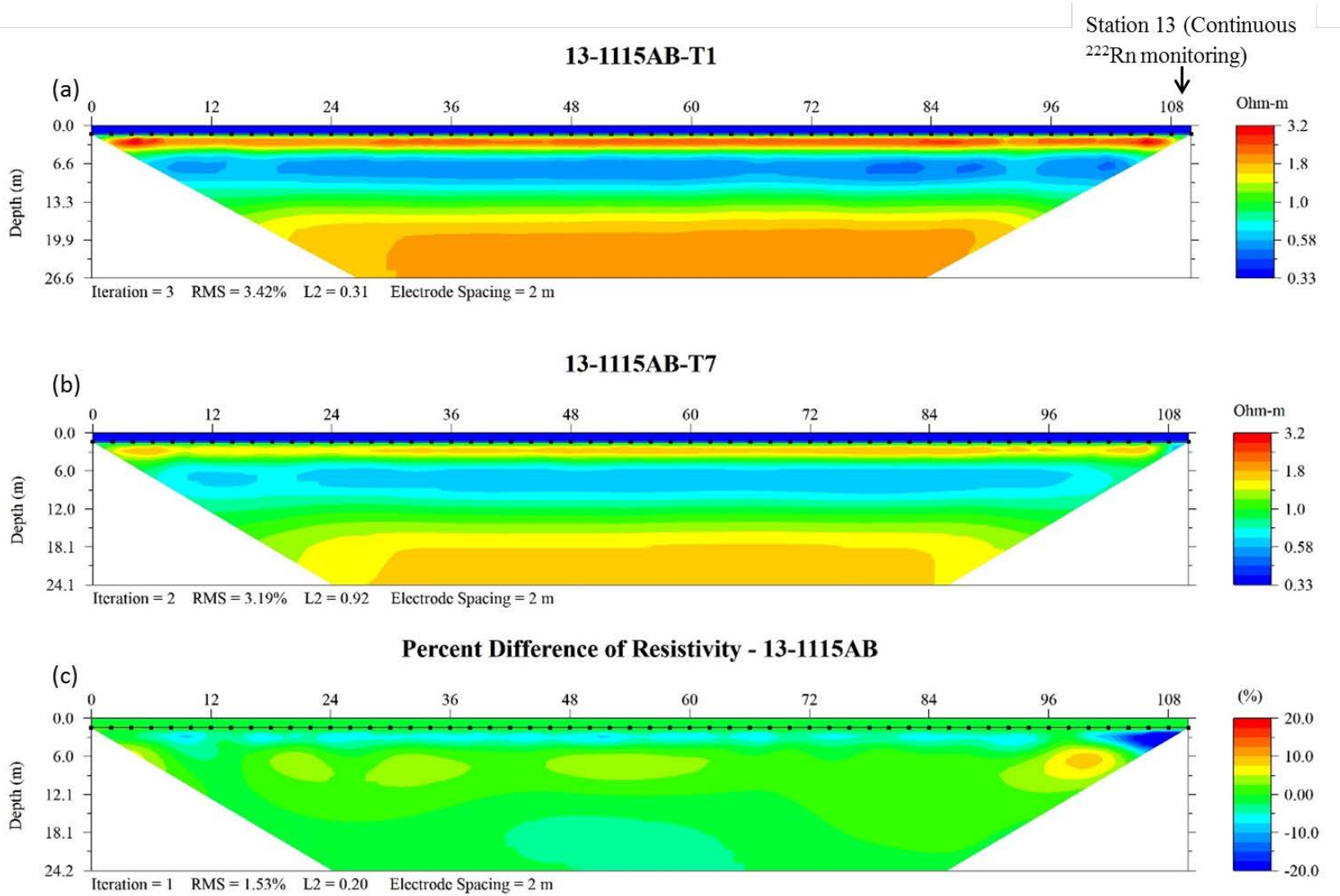

Figure TL 4: Fall time-lapse resistivity profiles (first (a) and last (b) time steps) for station 13 at St. Charles Mouth (see Figure 11 for geographic reference). The computed percent difference in resistivity (c) shows the change in porewater resistivity over an eight-hour period.

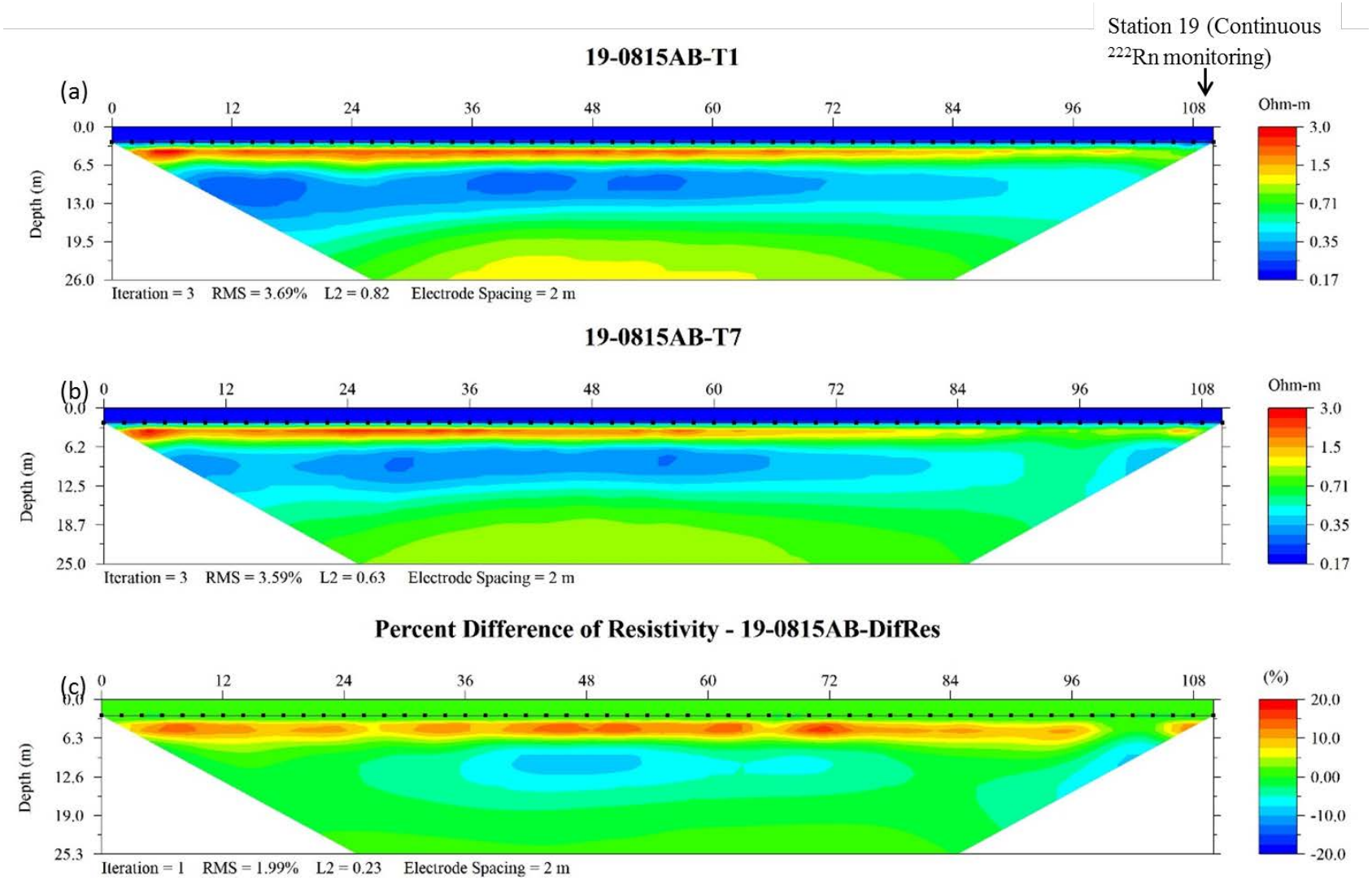

Figure TL 5: Summer time-lapse resistivity profiles (first (a) and last (b) time steps) for station 19 in Redfish Bay (see Figure 10 for geographic reference). The computed percent difference in resistivity (c) shows the change in porewater resistivity over an eight-hour period.

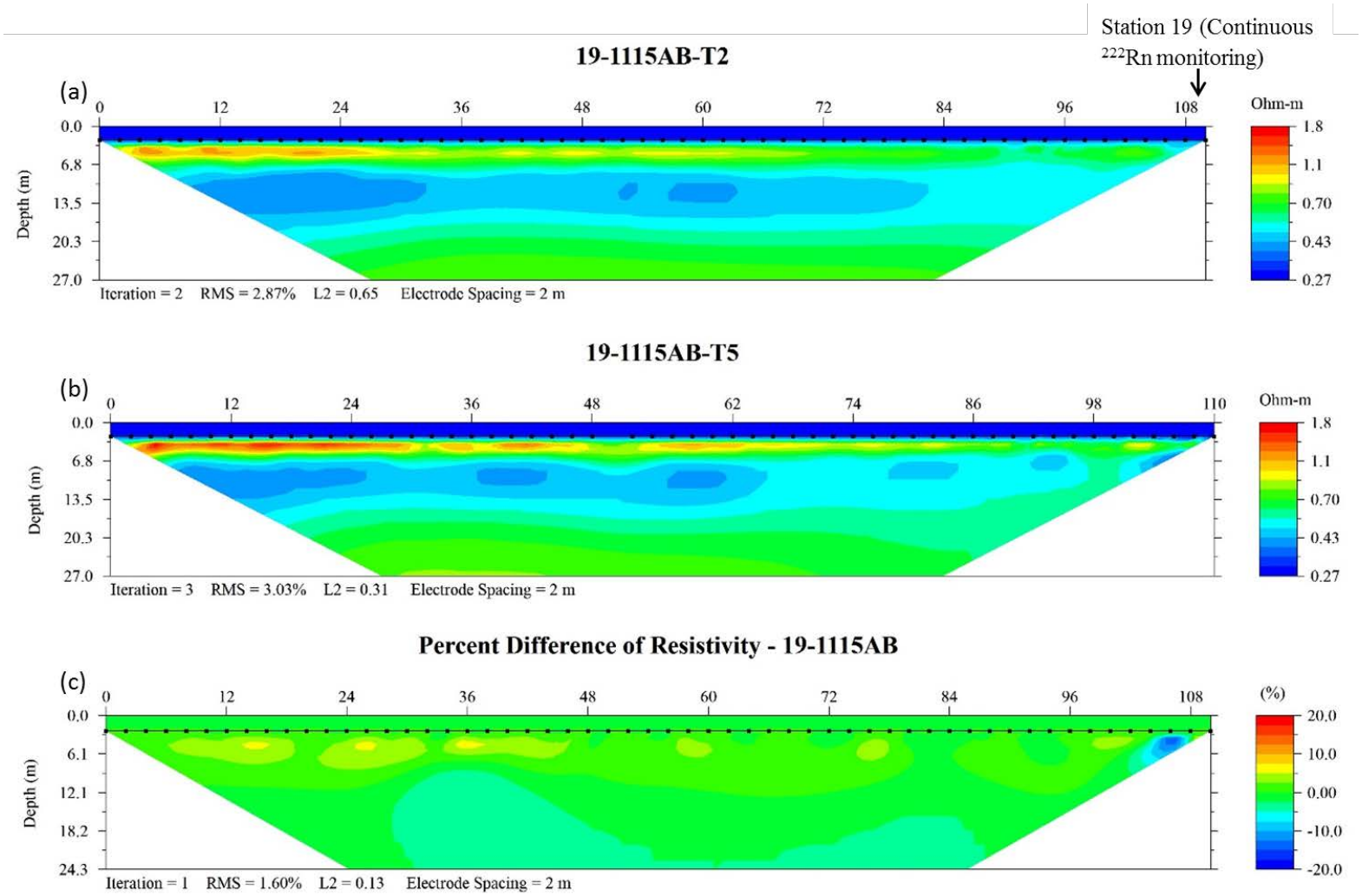

Figure TL 6: Fall time-lapse resistivity profiles (first (a) and last (b) time steps) for station 19 in Redfish Bay (see Figure 11 for geographic reference). The computed percent difference in resistivity (c) shows the change in porewater resistivity over a six-hour period.